DYNAMIC SOIL EROSION MODELLING WITH FUTURE SCENARIOS OF CLIMATE CHANGE

Francesco Niccolò Polinelli

POLITECNICO DI MILANO
DEPARTMENT OF CIVIL AND ENVIRONMENTAL ENGINEERING
DOCTORAL PROGRAMME IN ENVIRONMENTAL AND INFRASTRUCTURE ENGINEERING

Dynamic Soil Erosion Modelling with Future Scenarios of Climate Change

Doctoral Dissertation of:
Francesco Niccolò Polinelli

Supervisor:
Prof. Marco Gianinetto

Tutor:
Prof. Riccardo Barzaghi

The Chair of the Doctoral Program:
Prof. Riccardo Barzaghi

34th Cycle – 2022

Abstract

Soil erosion is a natural process caused by the erosive forces of rainfall or precipitation runoff, which causes soil detachment or removal of rock materials. It is addressed as one of the main hydrological risks in the European union, and the Alps are one of the most prone areas to soil erosion, in Europe. It causes nutrients loss and exposes the environment to landslides, with negative impacts on agriculture, ecosystem and infrastructures. Several human activities and climate change induce environmental modifications which intensify the pressure on soils and increase their predisposition to water erosion. Therefore, understending soil erosion spatial patterns and temporal trends could provide important information for supporting government land use policies and strategies to reduce this underestimated natural hazard. In this work the potential soil erosion rate is estimated by the D-RUSLE model under climate change and land use/land cover change scenarios, in the Alpine section of the Oglio river basin in North Italy. D-RUSLE is a modified version of the well-known RUSLE model that aims at providing more accurate estimates of the potential soil erosion. The classic RUSLE was modified to include the shielding effect of snow on soil erosion, with the integration of a model that describes separately the behaviour of rainfall and snow and, moreover, the temporal evolution of the land cover and its spatial distribution were estimated with the integration of Earth Observation data. Climate projections are obtained trough statistical spatio-temporal downscaling of 9 simulations among those available from CMIP5 protocol. Projection of land use/land cover have been obtained through a neural network algorithm trained with past land cover maps. The results show that the integration of satellite-derived data in D-RUSLE allow a better representation of soil erosion forcings, thus providing a more accurate erosion estimation to support government land use policies and strategies. Furthermore the results show two possible scenarios at 2100: if mean annual precipitation is unvaried and temperature increases of about 1.5-2 °C, almost 47% of the area would experience a reduction in the mean annual erosion rate and only the 18% would see an increase; If precipitation increases of about 8% and temperature raises of about 4 °C, then almost the 16% of the territory could expect an erosion rate decreases while the 72% will see an increase. To conclude the scalability of the model was tested, implementing it in a different area, the Dudh Koshi basin, in Nepal. The lower availabilty of data forced the implementation of machine learning algorithms to better optimize the parameters of the D-RUSLE model and its coefficients, in order to obtain realaiable results. The model proved to be scalable in a different area and the machine learning

algorithm proved to be a useful tool to optimize the model parameters and integrate geographical with statistical data.

Keywords: Soil Erosion, RUSLE, Earth-Observation, Climate Change, Machine learning, Neural Network

Contents

List of Figures

List of Tables

Chapter 1

Introduction

Soil is an extremely complex and variable medium and is subject to a series of degradation threats, as erosion, decline in organic matter, local and diffuse contamination and landslides. However, soil formation is such an extremely slow process, that soil can be considered as a non-renewable resource (6). As an example, the average annual soil loss rate in Europe accounts for 2.46 [t ha-1 yr-1] (2), which is about the double of the average soil formation rate, estimated in 1.4 [$\mathrm{t\,ha^{-1}\,yr^{-1}}$] (7). According to the European Commission Soil Thematic Strategy, soil erosion is one of the main hydrological risks in Europe, where 115 million hectares (12% of Europe's total land area) are subject to water erosion. Soil erosion is defined as the detachment of soil particles caused by the locally intense shear stress generated by raindrop impact (8). This phenomena has impact on land fertility loss, food production, drinking water quality, ecosystem services, flood an muddy flood risk and carbon stock shrinkage (9). In fact, the increased turbidity of fluvial and maritime environments, due to growth in suspended sediments, can alter ecosystems with consequences on food production (e.g. eutrophication and decrease of aquatic biodiversity (10) (11) (12) (13)). Moreover, erosion exposes soil to landslides because of an increased runoff and can be, therefore, responsible of increasing hydrological risks in case of heavy rainfall. Consequences of soil erosion are especially relevant for agriculture, where soil loss is strictly related to the reduction of organic matter and nutrients. Besides, human activities, human-induced forces and climate change have slightly shown an effect in accelerating soil loss (6). Among all European regions, the Mediterranean countries, with the Alps in particular, have the highest soil loss rates due to special climatic conditions with prolonged dry periods followed by heavy rainfall combined with steep slopes (2). From a modelling point of view soil erosion is mainly controlled by precipitation, topography, soil properties, land use/land cover and soil conservation practices. An ideal model would describe all the individual processes on the basis of hydraulics, hydrology and sediment transport theory equations, providing the basin response in terms of volume of sediments passing through

the closing section for a given input rainfall. However, nowadays there are many simplified models in the literature. Based on their constitutive framework, erosion models can be grouped in: i) empirical models; ii) conceptual models and iii) physics-based erosion and sediment transport models. Empirical models do not depend on a rigorous description of the physical process and require less computational cost and less a priori information. While being simple models, nevertheless they are useful tools for estimating soil loss at a catchment scale when limited data and input parameters are available (8). The most widely used empirical models are USLE (Universal Soil Loss Equation) (14), MUSLE (Modified Universal Soil Loss Equation) (15), RUSLE (Revised Universal Soil Loss Equation) (16), AGNPS (AGricultural Non-Point Source pollution model) (17) and SEDD (SEdiment Delivery Distributed) (18).Conceptual models describe the watersheds with a series of storage units and incorporate the general description of the catchment dynamics in terms of the underlying processes of sediment and runoff generation (8). Some examples are CREAMS (field scale model for Chemicals, Runoff and Erosion from Agricultural Management Systems) (19) and LASCAM (LArge Scale CAtchment Model) (20). Finally, physics-based erosion and sediment transport models use the mass conservation equation for flow and sedimentation processes simulation. They are able to describe the different phenomena contributing to erosion and their interactions, simultaneously (8). The rigorous description of the physical processes makes possible to extend their use to areas with very different characteristics. Although providing a more realistic representation of the processes, these models can suffer from high uncertainty due to the large number of input parameters required, that often need to be calibrated against observed data (**?**). Some examples are EUROSEM (EUROpean Soil Erosion Model) (21), WEPP (Water Erosion Prediction Project) (22) and ANSWERS (Areal Non point Source Watershed Environment Response Simulation) (23). Soil erosion models are important tools for understanding soil loss rates, spatial patterns and trends for supporting government land use strategies for effective erosion control practices and soil conservation (24). Even if the factors that influence erosion could be extremely variable in time and space, nonetheless these models frequently use a static definition for some of the input parameters that may present changes in space and time such as land cover. Therefore, Earth Observation from optical satellite, can help in the representation of these changes in space and time and thus improving the results of soil erosion modeling (25). In past years, multispectral satellite images were adopted to detect erosion features and eroded areas (e.g. large and medium sized gullies and badlands) or erosion consequences (e.g. water quality assessment in terms of suspended sediments in reservoirs and lakes) (26). Land cover mapping is a common input for soil erosion modelling because different land classes have a different protective effect towards erosion, especially vegetation (27). Once mapped, vegetation is assigned a

sheltering effect, depending on its type (26) or based on a vegetation index (28)(29). The main advantage of using satellite Remote Sensing data within soil erosion studies is the ability to account for seasonal variability of vegetation, long-term land cover changes and to provide such information with a spatial resolution suitable to exploit soil erosion at regional/local scale (landsat satellites provide images with a 30m spatial resolution). Of course, optical data suffer from lack of information in case of cloud cover and shadows, which are relevant in the mountainous environment and especially during Winter. Nevertheless, the actual high revisit time (16 days for landsat satellites) compensate this issue. This work models the potential soil erosion rate, at the catchment scale, in the central alpine and pre-alpine area of Italy by integrating a modified version of the RUSLE model (16) with multi-temporal satellite observations. RUSLE is widely used in the scientific community (30)(31)) and is usually applied considering the average rainfall erosivity, no land-use/land-cover changes and, thus, static sheltering effect provided by vegetation within the simulation period. Here we introduce i) the seasonal dynamics of precipitation by considering both rainfall (active in erosion) and snow (non-contributing to erosion); ii) the sheltering effect of snow cover dynamics; iii) the seasonal dynamics of vegetated areas and iv) long-term land-use/land-cover changes. All these novelties aim to improve potential soil erosion modelling in the Alps. Climate change and land transformations can induce environmental modifications able to intensify pressure on soils, thus increasing their predisposition to water erosion, modifying the dynamics of soil erosion and related hazards. In terms of processes, rainfall amounts and intensities are certainly the most direct and important factors controlling erosional changes under climate change. Besides, also land use and land cover transformations, together with biomass production, contribute in modifying soil loss (32)(33)(34). The Alps are extremely vulnerable and dynamic environments due to their morphological and land use/land cover variability, and are characterized by the highest soil loss rates in Europe, further intensified by special climatic conditions with prolonged dry periods followed by heavy rainfall (35). In particular, in the Alpine region the contribution of climate change is twofold. On one hand, the intensification of precipitation phenomena increases the rain erosive capacity. On the other hand, the temperature increase can faster desertification processes, reducing the vegetation sheltering effect to soil erosion. In addition, the Alpine glaciers retreat contribute to increase erosion since a large amount of sediments become exposed to erosion forcing. Moreover, the anthropogenic transformation of land cover, such as deforestation, urbanization, agricultural patterns reshaping and intensive grazing, tillage and deforestation, makes the territory more vulnerable and modifies the response of river basins by producing higher surface runoff with impact on river flow sediment transport capacity. Despite such expectations and their medium to long-term impact on water resources (13)(36)(37)(38) and hydrological

extremes (39)(40), little investigation has been devoted to analyze potential soil erosion in the context of future climate change and land transformation. Anyway, a common belief is that unsustainable land management and climate change will result in a change in erosion rates, and that the undeniable increase in rainfall amount and intensity and the increased human pressure on soils will lead to higher erosion rates, unless amelioration or management policies are taken from a global to a regional scale (41). In this context, the aim of this work is to provide a long-term overview of climate and land use/land cover changes impacts on soil erosion in the Alpine part of the Oglio River basin and to identify the potentially most fragile areas with respect to actual estimated soil loss. Thus, the D-RUSLE model (42) (43), is applied to provide future soil erosion estimates. This model is derived from the widely used RUSLE model, which provides a parametric evaluation system for land degradation in terms of soil erosion by integrating parameters of climate, soil, topography and vegetation. Current soil erosion is well addressed but the prediction of future soil erosion under climate change and land cover transformations is still studied with insufficient detail, even though the understanding of their combined effect on both hydrological and erosion processes is crucial (40). In fact, most studies focused on climate change without considering the effects of land changes (39)(41)(44), and only fewer works evaluated the impacts of both of them (40) (45) (46). In this context, the Alps are one of the most vulnerable ecosystems of Europe. They are located in a transitional zone between the drying Mediterranean region (South Alps) and the wetting northern Europe (North Alps). During the last century, the temperature in the Alpine region increased about +2 °C, and most of the climate projections agree to expect a generalized temperature increase in the future (47)(48). It is a different matter for precipitation, which is erratic. For the future, climate projections mainly expect dryer summers and wetter winters (47)(48)(49), but future scenarios do not agree unanimously. In this regard, (47) analyzed the climate projections of the global climate models (GCMs) in the Coupled Model Intercomparison Project release 5 (CMIP5) (50) for the Alpine arc. For the end of the XXI century, the authors found a very wide range of temperature changes, depending on the representative concentration pathways (RCPs (51)) considered, extending from -0.8 °C up to +8.9 °C. The variability in precipitation for GCMs driven by scenarios RCP2.6, RCP4.5, and RCP6.0 is quite similar: it approximately ranges between -5 to +20% in winter, -8 to +25% in spring, -30 to +25% in summer, and -10% to +15% in autumn. For South Alps, most of the global climate models driven by RCP4.5, RCP6.0, and RCP8.5 project precipitation increases in winter and a generalized decrease in the other seasons. With reference to regional modelling, (48) analyzed an ensemble of regional climate models (RCMs) projections for the Alpine region at end of the XXI century (A1B emission scenario). Climate simulations agree in expecting a temperature increase between +2.7 °C in spring and +3.8 °C

in summer. For precipitation, the expected changes are between 20.4% in summer and +10.4% in winter. The outcomes of the Coordinated Regional Downscaling Experiment (CORDEX) by Smiatek et al. (49) seems confirming these trends. For the end of the XXI century the authors predicted a temperature increase in the Greater Alpine Region of +2.5 °C in autumn and winter, +2.4 °C in summer, and +1.9 °C in spring. Precipitation is expected to increase up to +12.3% in winter, +5.7% in spring, and +2.3% in autumn. Compared to (47)(48) their study predicted a smaller decrease in precipitation in summer (about -1.7%). In this context, the Alps are one of the most vulnerable ecosystem of Europe. (47) analyzed the climate projections of the global climate models (GCMs) available in the Coupled Model Intercomparison Project release 5 (CMIP5) for the Alpine arc (50) that extends from 41° N to 50° N in latitude and from 4.6° E to 16.2° E in longitude. Compared to the baseline 1980–2009, the authors found that at the end of this century (2070–2099) the North Alps are expected to be wetter in winter and spring and dryer in summer. On the other hand, climatic simulations project dryer seasons in the South Alps, with the exception of winter where precipitation might increase. Temperature changes have a very wide range, depending on the representative concentration pathways (RCPs (51) considered: from -0.8 °C to +8.9 °C in the North Alps, and from 0.4 °C up to +9.5 °C in the South Alps. (48) projected temperature increases for the end of the century up to +2.7 °C in spring and up to +3.8 °C in summer, with precipitation changes between 20.4% in summer and +10.4% in winter. The analysis of regional climate models (RCMs) done by Smiatek et al. [24] seems confirming these trends. Studying the Greater Alpine Region, which extends from 43° N to 49° N in latitude and from 4.0° E to 19° E in longitude, for the end on the century the authors predicted a temperature mean increases of +2.5 °C in fall and winter, +2.4 °C in summer and +1.9 °C in spring at 2071–2100 (baseline 1971–2000). Precipitation is expected to increase up to +12.3% in winter, +5.7% in spring, and +2.3% in fall. However, compared to (48) their study predicted a small decrease in precipitation in summer of about -1.7%. As a consequence, the peculiar morphology of the Alps, their land cover variability, and unique climatic conditions are responsible for one of the highest soil loss rates of the whole European Union. In particular, climate change in the Alpine region might have different impacts. On the one hand, the intensification of precipitations increases the rain erosive capacity. On the other hand, the temperature increase can foster desertification processes, thus reducing the sheltering effect of vegetation. In addition, the temperature increase is also causes the retreat of glaciers that is exposes a large amount of new sediments to the erosive agents (48)(52). Moreover, the anthropogenic transformations of the landscape, such as deforestation, urbanization, agricultural patterns reshaping, intensive grazing, and tillage, is makes the territory more vulnerable to erosion and is also modifying the response of the river basins by producing higher

surface runoffs with impacts on the sediment transport capacity of rivers (38)(39)(41). (2) calculated the soil loss for all the European Union. The authors found that the mixture of high rainfall erosivity with relatively steep slopes produces high erosion rates in the Alpine areas, the Apennines, the Pyrenees, the Sierra Nevada, western Greece, western Wales, and Scotland. They estimated a mean soil erosion rate of 5.27 [t ha-1 yr-1] for the Alpine climatic zone (Alps, Pyrenees, and southern Carpathians). This is the double of the European mean value 2.46 [t ha-1 yr-1] but lower than the mean value estimated for Italy 8.46 [t ha-1 yr-1]. Such values are coherent with the sediment yield of 3.06 [t ha-1 yr-1] reported for the Dora Baltea mountain basin in North West Alps (53). A common belief is that unsustainable land management and climate change will result in a change in erosion rates, and that the undeniable increase in rainfall amount and intensity and the increased human pressure on soils will lead to higher erosion rates, unless suitable management policies will be taken from a global to a regional scale (41). Nevertheless, despite such a gloomy scenario and the expected medium to long-term impacts on water resources (54)(55)(56)(57) and hydrological extremes (58)(59), the study of soil erosion in the context of future climate change and land transformation is still investigated with insufficient detail. This study tries to fill this gap by analyzing how climate change and land cover transformations are expected to impact soil erosion in a typical territory of the Italian Alps. Based on the different assumptions described below, bestcase and worst-case scenarios for the end of the XXI century are presented.

The second part of this work focuses not on estimating soil erosion per se, but on different method to compute the parameter of the model, in order to make it possible also in different part of the world, where the data availability is less precise and abundant with respect to Regione Lombardia. The chosen area was the Dudh Koshi basin in Nepal. To obtain reliable parameter of the model starting from more coarse data, statistical data and machine learning algorithms were used. In this area were available daily meteorological data, instead of hourly like for Val Camonica. To overcome this difference in temporal resolution, in the SWE model computation, the results of the model were compared with maps derived from satellite remote sensing data of snow cover, and the parameter of the model iteratively changed with a baesyan optimization process to maximize the agreement between model output and satellite maps. As far as land cover are concerned the map for this area were less accurate and with a lower temporal update. To improve the precision of the land cover maps, statistical data of agricultural areas, available for each year in this area, were used. A classification process with SAM algorithm and Landsat images was performed and the results were compared with the statistical data. The thresholds of the SAM algorithm were iteratively changed in order to maximize the agreement between the results of the classification and the statistical data. In this case the Neural Network for the future projection of land cover maps was

performed testing three different model written with a python script. All the model share the same structure, with 16 input parameters and three hidden layers.

Chapter 2

Study Area

2.1 Val Camonica Study Area

This study estimates the potential soil erosion in the central alpine and pre-alpine area of Italy. The study area is Val Camonica (one of the largest valleys of the Central Alps), that is the Oglio River basin closed at Sarnico, which extends about 1,800 km2 (Figure 2.1). The analyzed area is characterized by an alpine climate, as confirmed by the data gathered by temperature stations and rain gauges, with cold Winter (average temperature 1.16 [°C]) and moderate Summer temperatures (average temperature 18.3 [°C]) on average, with higher temperatures in the lake areas (10.8 [°C]) respect to the high elevation areas (4.3 [°C]). The annual average precipitation is about 1,300 [mm yr-1], with peaks in Summer and Autumn and it is distributed almost homogeneously in the test case area. Snowfalls are possible from October to May and the snow cover generally persists at higher elevations until July. Within the study area, the elevations range from 185 [m a.s.l.] in Sarnico to 3,585 [m a.s.l.] of the Adamello Glacier. Almost 90% of the landscape is vegetated (about 45% are forests and only less than 1% are croplands), characterized by the typical mountainous vegetation distribution influenced by elevation variations and by precipitation seasonal regimes. In the following analysis the study area is divided in three elevation ranges: high elevation areas (elevation $\geq 1,600$ [m a.s.l.]) covering about 649 [km2], medium elevation areas (1,000 [m a.s.l.] < elevation < 1,600 [m a.s.l.]) covering about 570 [km2] and Iseo Lake areas (elevation $\leq 1,000$ [m a.s.l.]) covering about 580 [km2], of which about 65 [km2] corresponds to the lake surface (Figure 2.1 and 2.2).

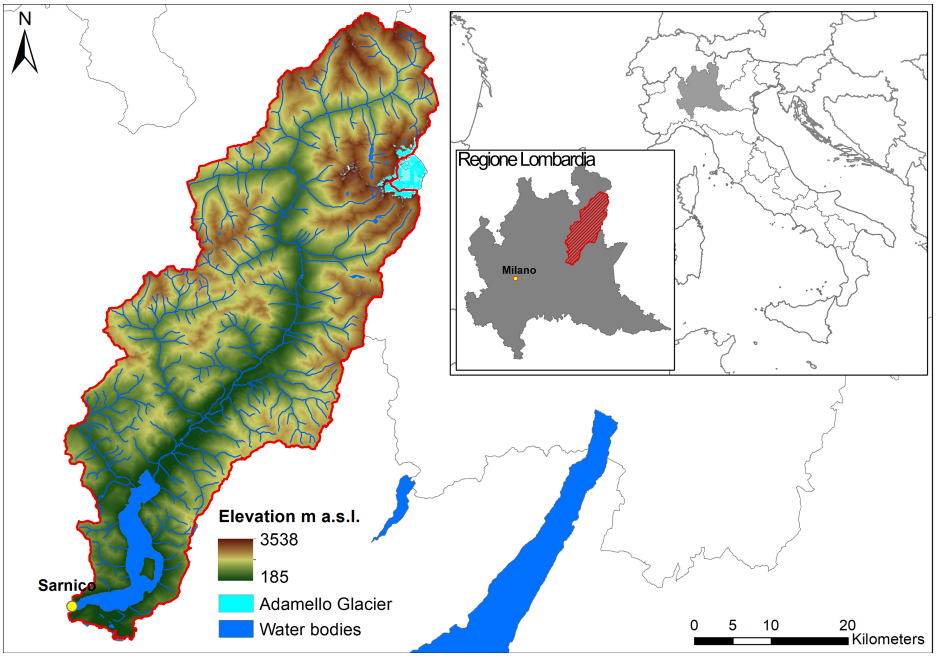

Figure 2.1: Study area: a) Digital Elevation Model of Val Camonica

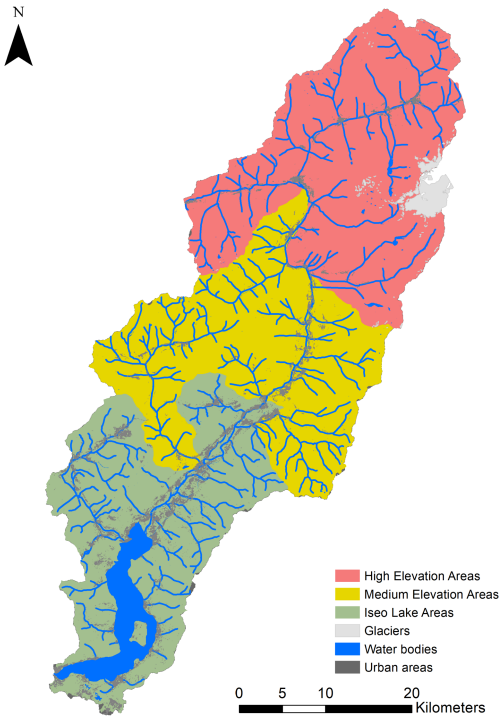

Figure 2.2: Subdivision of the study area in high elevation areas (elevation $\geq 1,600$ [m a.s.l.]), medium elevation areas (1,000 [m a.s.l.] $<$ elevation $<$ 1,600 [m a.s.l.]) and Lake Iseo areas (elevation $\leq 1,000$ [m a.s.l.]).

2.2 Nepal Study Area

As far as the second part of the work is concerned the study area is located in the hilly and mountain region of Nepal, and it extends for 7000 km^2 with an elevation range from 155 to the 8848 [m a.s.l.] of mount Everest. The annual rain discharge is about 1800 mm, the 80% of which is focused in the monsoon season, from may to October. And vegetation is the main land cover.

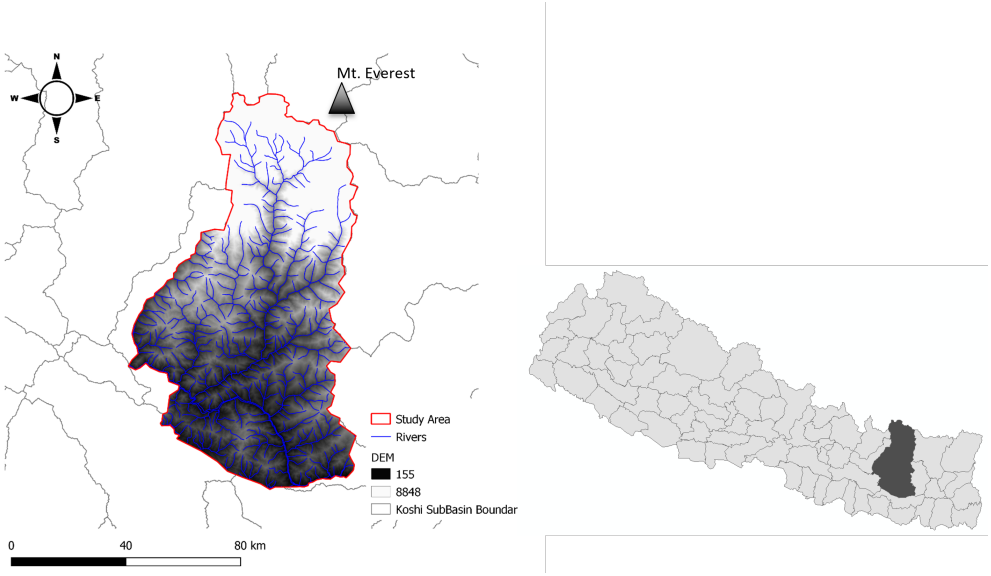

Figure 2.3: DEM of the Dudh Koshi basin, and its position inside the country of Nepal

Chapter 3

Data

3.1 Val Camonica Data

Within this work, we refer to official data supplied by Regione Lombardia (`www.geoportale.regione.lombardia.it`), Comunità Montana della Valle Camonica (`www.geoportale.cmvallecamonica.bs.it`) and Environmental Protection Agency of Regione Lombardia (`www.arpalombardia.it/siti/arpalombardia/meteo`), which are available in their geo-portals.

3.1.1 Thematic maps

With regard to thematic maps, were used:

- The 30-meters spatial resolution Digital Elevation Model of Regione Lombardia (Figure 2.1). This data as an accuracy of 0.30m for urban areas, 1m for extra-urban areas with presence of infrastructure and 2m for extra-urban areas;
- The DUSAF (Destinazione d'Uso dei Suoli Agricoli e Forestali) land-cover/land-use map of Regione Lombardia for the years 2000, 2007 and 2015. This thematic map, has a nominal scale of 1:10000 and is organized in five hierarchical levels where the first three are compliant with the European Corine Land Cover (CLC) map. Additional land-cover/land-use classes representative of Regione Lombardia territory are also available. Within this work, we used the third level (Figure 3.1);

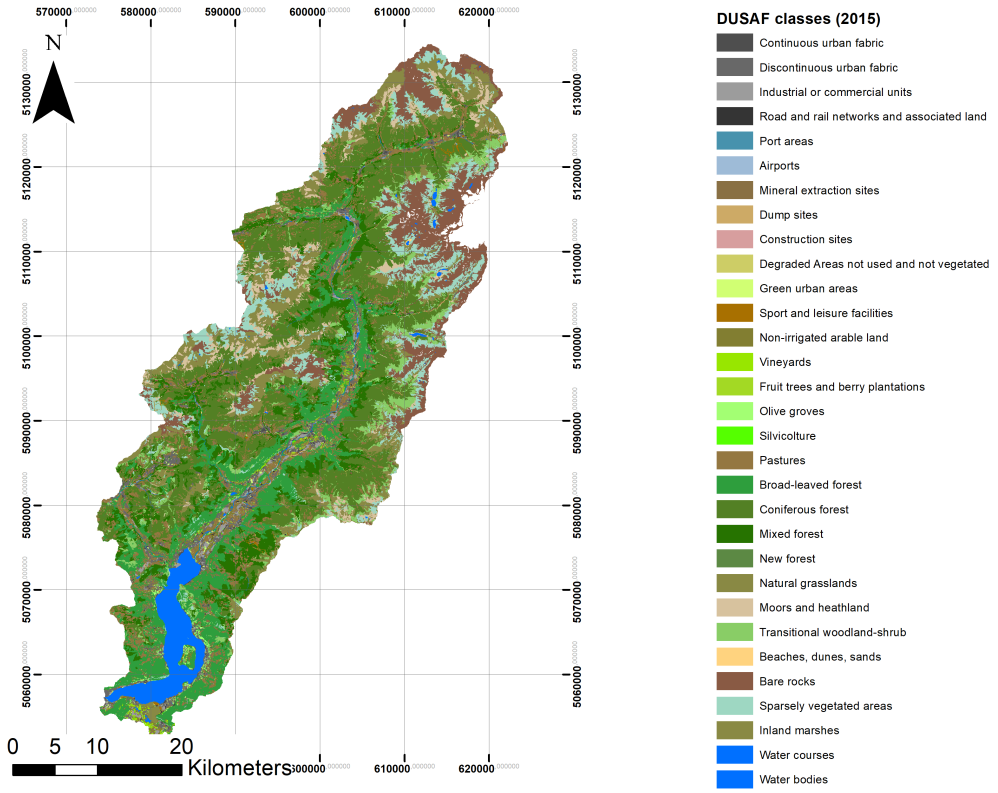

Figure 3.1: The DUSAF (Destinazione d'Uso dei Suoli Agricoli e Forestali) land-cover/land-use map of Regione Lombardia for the year 2015.

- The soil map of Regione Lombardia (Figure 3.2). This map,produced between 2008 and 2011, has a nominal scale of 1:250000 with the minimal mapping unit of 20 ha.

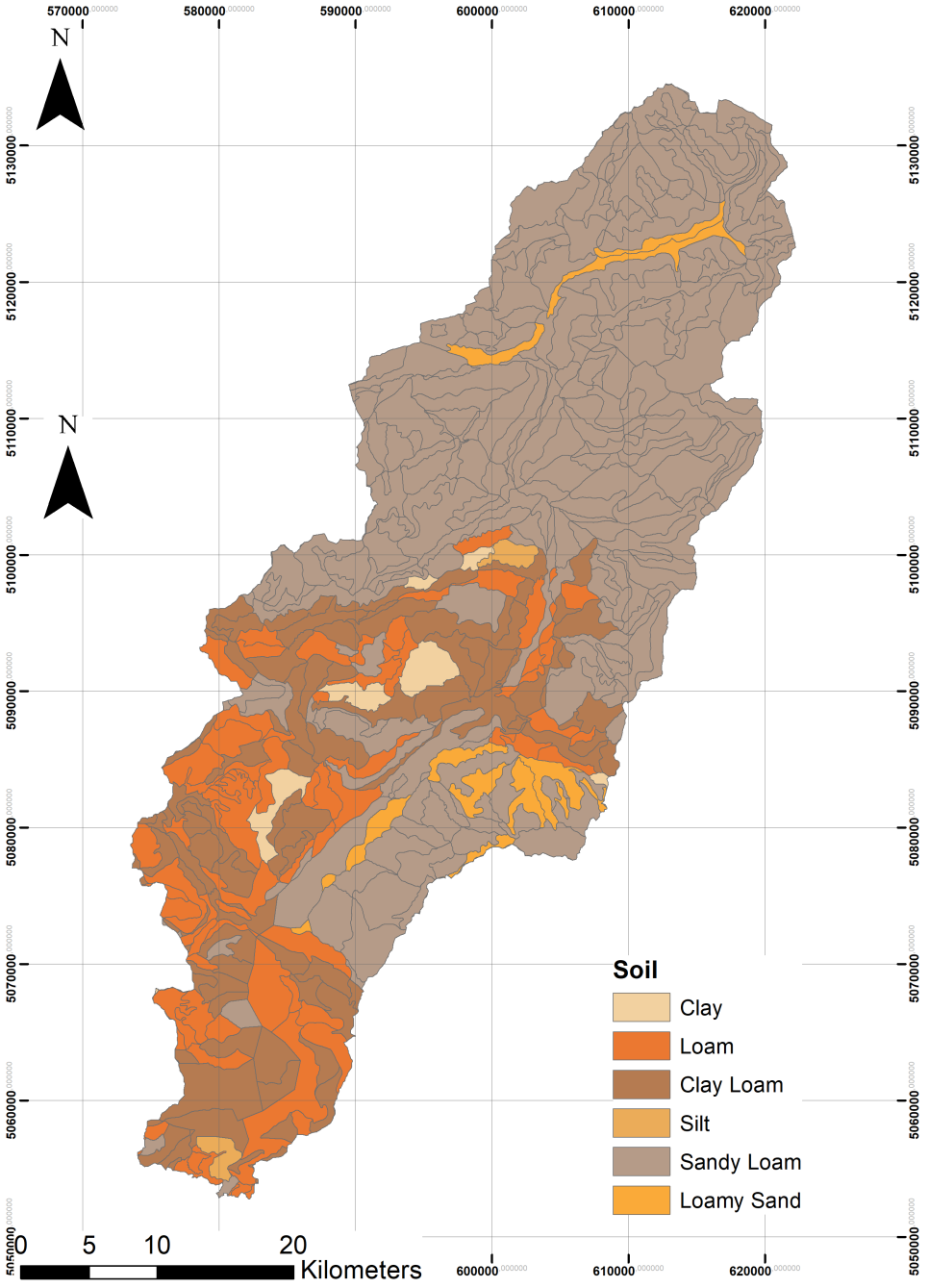

Figure 3.2: Soil map of the study area.

3.1.2 Meteorological data

With regard to meteorological data, I used hourly time series of precipitation and air temperature recorded from 2003 to 2017 by 30 rain gauges and 28 thermometers belonging to the Environmental Protection Agency of Regione Lombardia (Figure 3.3).

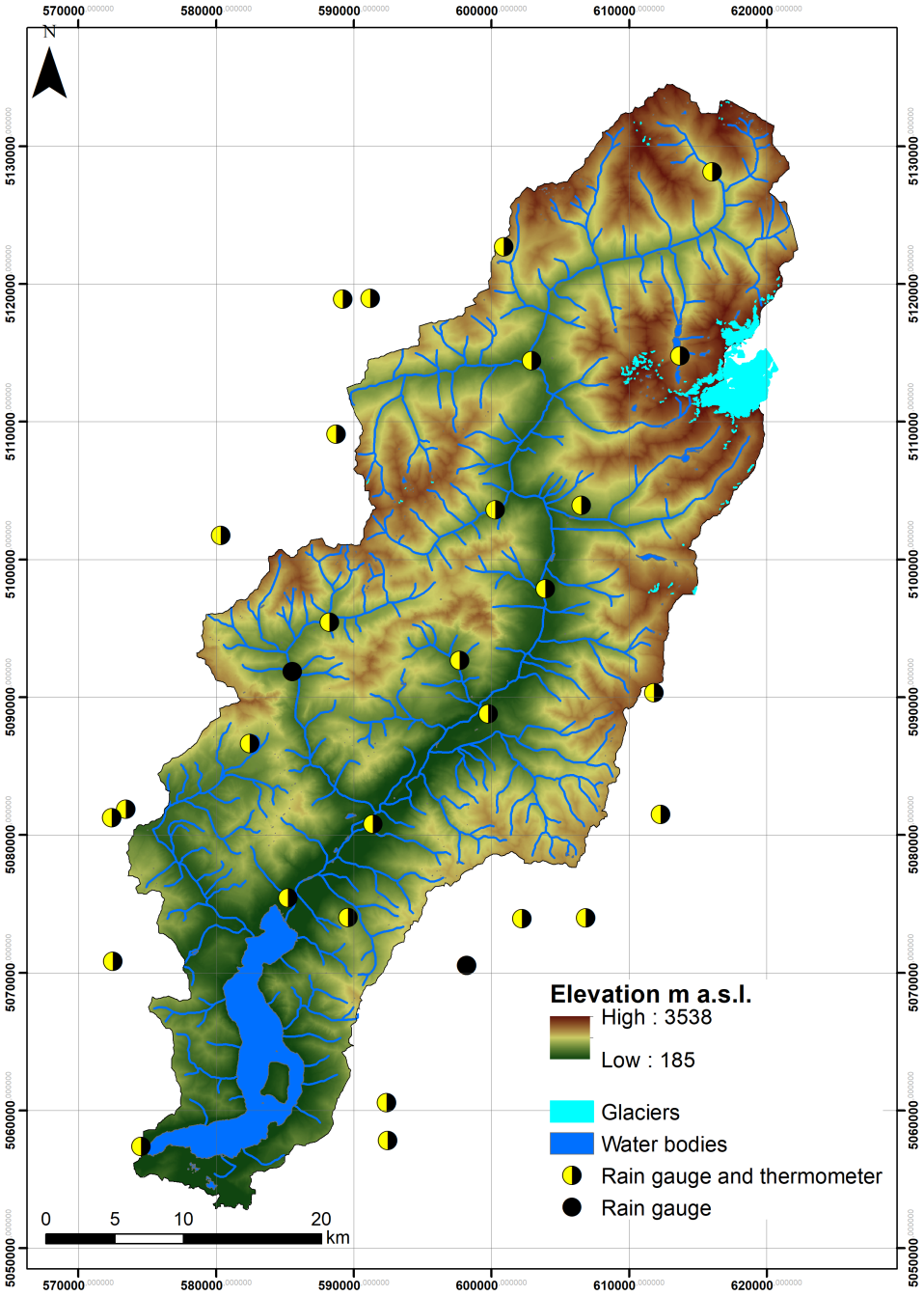

Figure 3.3: Study area with highlighted the rain gauges and the thermometers used.

3.1.3 Satellite Remote Sensing data

With regard to Remote Sensing data, I used a time series made of 20 images collected by Landsat-5/TM, Landsat-7/ETM+ and Landsat-8/OLI in the period 2002-2017. The images were acquired both in Autumn/Winter (September-February) and in Spring/ Summer (March-August) to provide seasonal estimates. In this work were not used Sentinel-2 data because they were not available for the entire analyzed period, but in

an other context these data would offer reliable dataset with better spatial and temporal resolution with respect to the Landsat data.

Table 3.1: List of Landsat images used in this study.

LANDSAT IMAGES		
Image Name	**Acquisition Date**	**Season**
LT05_L1TP_193028_20000228_20171211_01_T1	28/02/2000	Winter
LE07_L1TP_193028_20000713_20211119_01_T1	13/07/2000	Summer
LE07_L1TP_193028_20010801_20210520_01_T1	01/08/2001	Summer
LE07_L1TP_193028_20011207_20200917_01_T1	07/12/2001	Winter
LE07_L1TP_193028_20020108_20211128_01_T1	08/01/2002	Winter
LE07_L1TP_193028_20020719_20200916_02_T1	19/07/2002	Summer
LT05_L1TP_193028_20030730_20161205_01_T1	30/07/2003	Summer
LT05_L1TP_193028_20040801_20161201_01_T1	01/08/2004	Summer
LT05_L1TP_193028_20041121_20161129_01_T1	21/11/2004	Winter
LT05_L1TP_193028_20060722_20161120_01_T1	22/07/2006	Summer
LT05_L1TP_193028_20070725_20161112_01_T1	25/07/2007	Summer
LT05_L1TP_193028_20090730_20161023_01_T1	30/07/2009	Summer
LT05_L1TP_193028_20110210_20161010_01_T1	10/02/2011	Winter
LT05_L1TP_193028_20110821_20161007_01_T1	21/08/2011	Summer
LC08_L1TP_193028_20130810_20170503_01_T1	10/08/2013	Summer
LC08_L1TP_193028_20140829_20170420_01_T1	20/08/2014	Summer
LC08_L1TP_193028_20141219_20170416_01_T1	19/12/2014	Winter
LC08_L1TP_193028_20150715_20170407_01_T1	15/07/2015	Summer
LC08_L1TP_193028_20151206_20170401_01_T1	06/12/2015	Winter
LC08_L1TP_193028_20160717_20170323_01_T1	17/07/2016	Summer
End of Table		

3.1.4 Field survey

In Summer 2017 13 soil samples were collected in the North East of the study area, where the elevation is higher and rocks are mainly metamorphic. In Summer 2018 we collected 14 soil samples at the lower altitudes of South West, where there is a predominance of calcareous sedimentary rocks. Sampling plots were selected to maximize soil texture and taxonomy variability within the study area (Figure 3.4). The details of the sampling plots are shown in Figure 4.3.

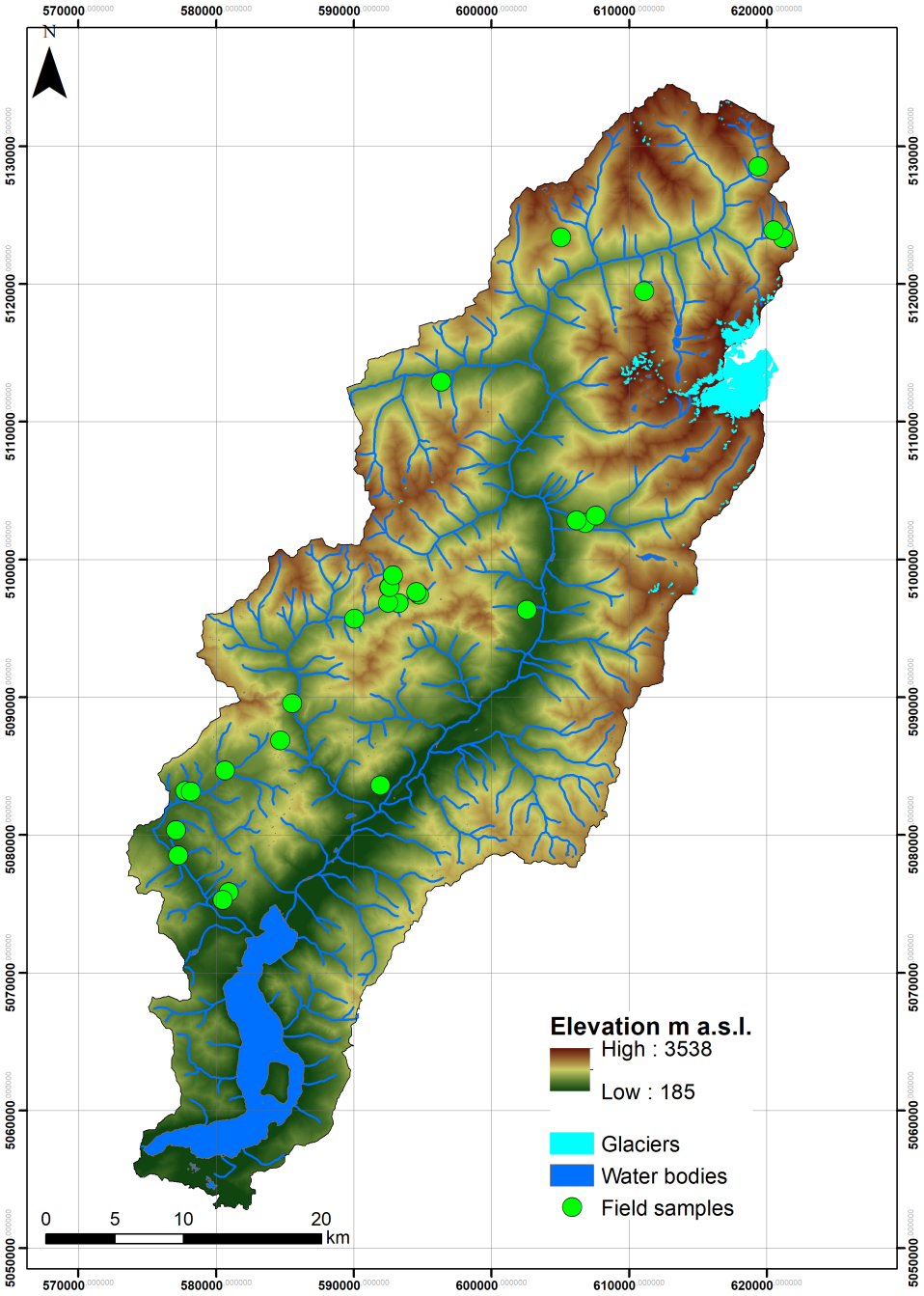

Figure 3.4: Study area with highlighted the sampling plots.

3.1.5 Climate Scenarios

Climate scenarios came from the spatio-temporal statistical downscaling of the GCMs under different RCPs made available by the CMIP5 [25]. In this study we considered the following GCMs models:

- European Centre HAmburg Model versione 6 (ECHAM6) [38];
- Community Climate System Model version 4 (CCSM4) [39];

- European Consortium Earth system model version 2.3 (EC-Earth) [40].

driven by the following RCPs [25,25]:

- RCP2.6: peak in radiative forcing at 3 [W m^2] (490 ppm CO_2 equivalent at 2040), and subsequent decline to 2.6 [W m^2]);
- RCP4.5: stabilization to 4.5 [W m^2] (650 ppm CO_2 equivalent at 2070);
- RCP8.5: radiative forcing up to 8.5 [W m^2] (1,370 ppm CO_2 equivalent by 2100).

By combining the three GCMs with the three RCPs I obtained nine different climate projections. Once downscaled, they returned nine climate scenarios at hourly resolution for each meteorological station. All the climate scenarios considered cover the period 1981–2100.

3.2 Nepal Data

Within this work were used data from the research institute ICIMOD (International Centre for Integrated Mountain Development) (60) for land cover and meteorological data.

3.2.1 Meteorological data

With regard to meteorological data, were used daily time series of precipitation and air temperature derived from a reanalysis of data from 1981 to 2010. This dataset (HIAWARE) (61) is provided with a resolution of 5 km for the entire study area.

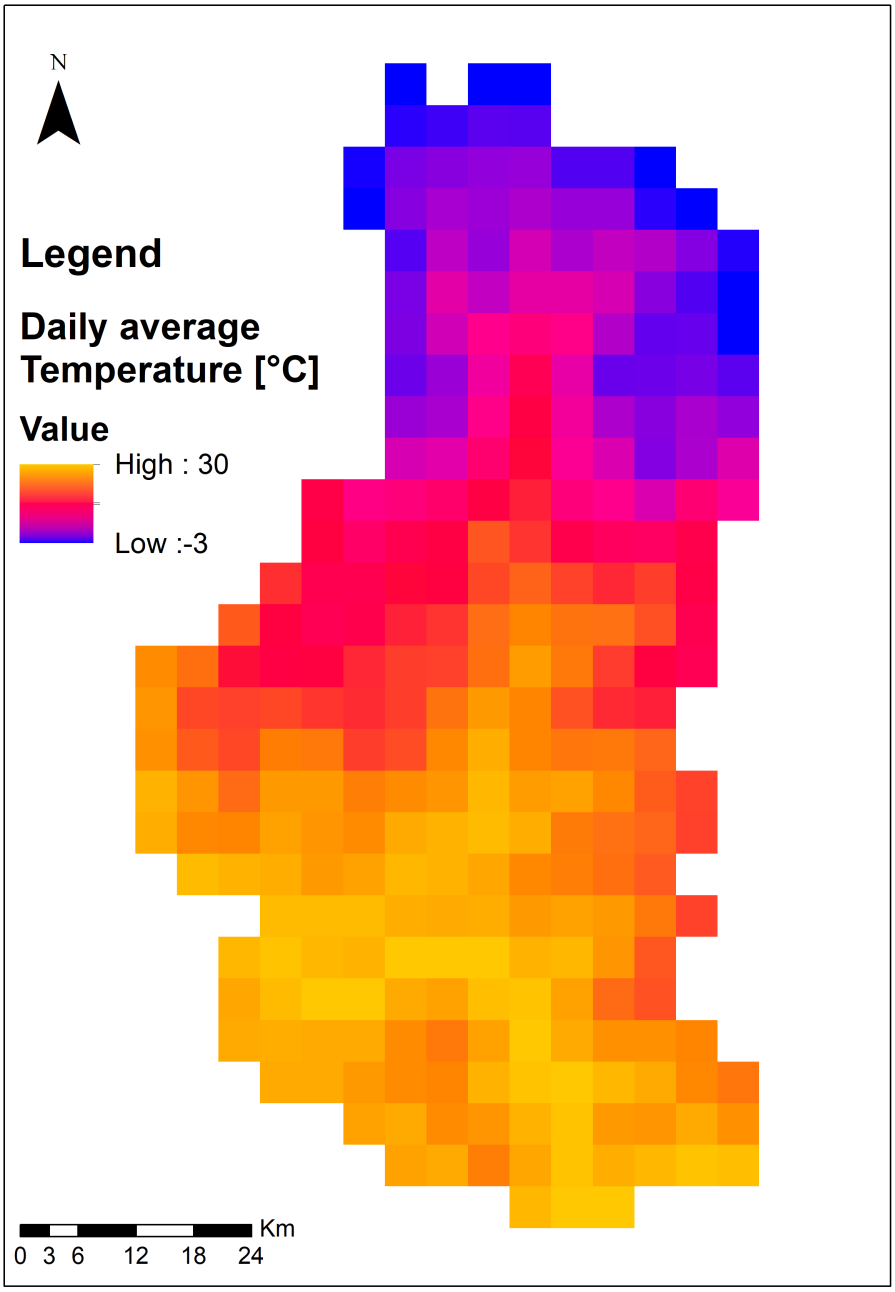

Figure 3.5: Temperature data - 29/Jun/2010 - 5km resolution

3.2.2 Digital Elevation Model

With regard to the Digital Elevation Model (DEM) used in this work the SRTM with a 30m resolution was used (62). On September 23, 2014, the White House announced that the highest-resolution topographic data generated from NASA's Shuttle Radar Topography Mission (SRTM) in 2000 was to be released globally by late 2015. The announcement was made at the United Nations Heads of State Climate Summit in New York. Since then the schedule was accelerated, and all global SRTM data have been released. Previously, SRTM data for regions outside the

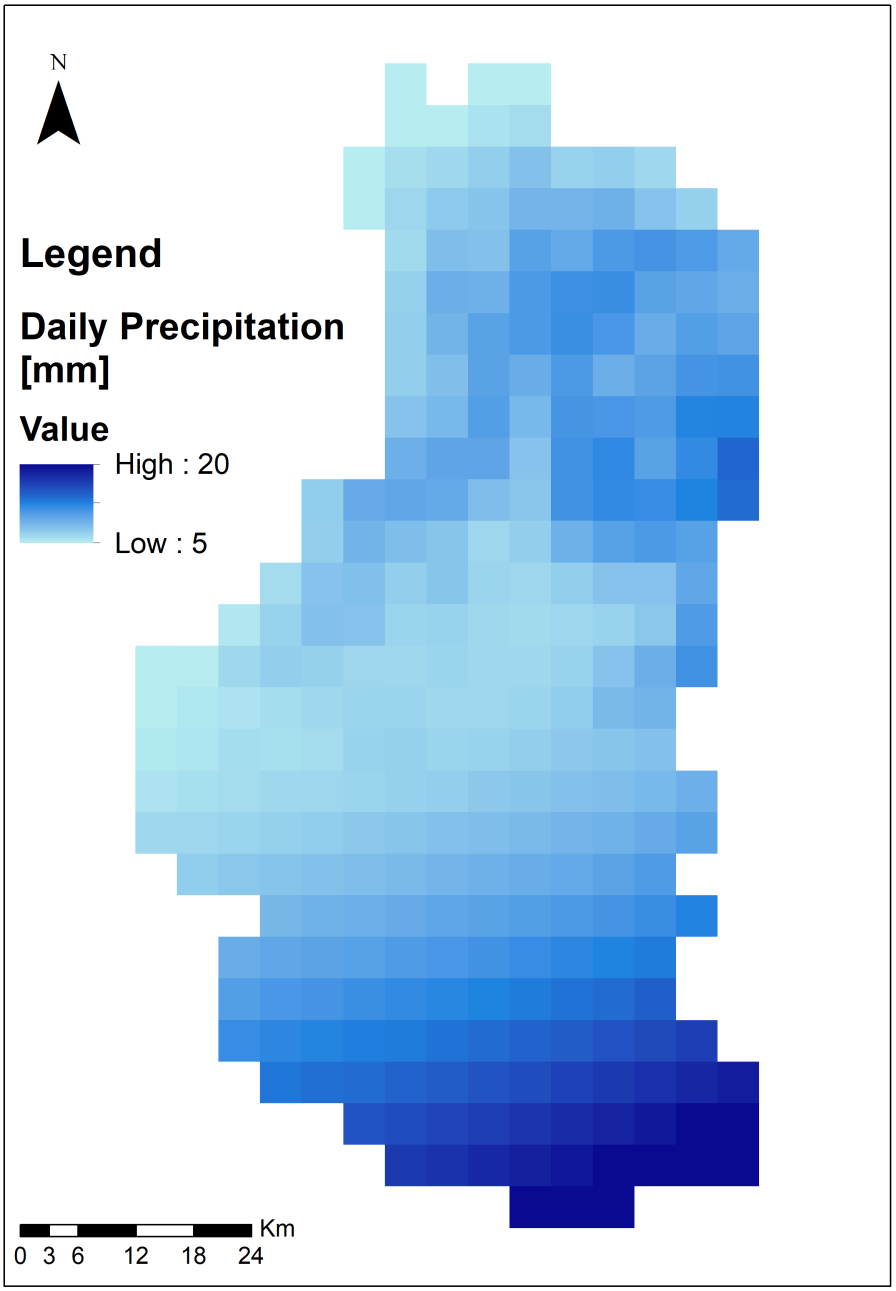

Figure 3.6: Temperature data - 29/Jun/2010 - 5km resolution

United States were sampled for public release at 3 arc-seconds, which is 1/1200th of a degree of latitude and longitude, or about 90 meters (295 feet). The new data have been released with a 1 arc-second, or about 30 meters (98 feet), sampling that reveals the full resolution of the original measurements.

3.2.3 Land Cover Maps

With regard to land cover maps, three Land Cover maps from ICIMOD were used. These maps were available for the period: 1990, 2000 and 2010. They were available for the entire koshi area and were divided in 9 different land cover classes: water bodies, snow/glacier, shrubland, grassland, forest, build-up area, barren area, rabi crops (winter cultures) and kharif crops (summer cultures). ICIMOD recently released an update version of the land cover maps, but the earlier version of the product was not accurate: the agriculture class was over represented, and that was occupying also forest areas. This misclassification was discovered comparing the area classified as "agriculture" with satellite images and statistical data provided by the Ministry of Agriculture and Livestock Development.

3.2.4 Satellite Remote Sensing Data

As far as satellite images are concerned for this study were used 15 Landsat images from 2009 to 2010

Table 3.2: List of Landsat images used in this study for Nepal.

LANDSAT IMAGES	
Image Name	**Acquisition Date**
LT05_L1TP_140041_20090201_20200828_02_T1	01/02/2009
LT05_L1TP_140041_20090217_20200828_02_T1	17/02/2009
LT05_L1TP_140041_20090305_20200828_02_T1	05/03/2009
LT05_L1TP_140041_20090508_20200827_02_T1	08/05/2009
LT05_L1TP_140041_20090913_20200825_02_T1	13/09/2009
LT05_L1TP_140041_20091015_20200825_02_T1	15/10/2009
LT05_L1TP_140041_20091202_20200825_02_T1	02/12/2009
LT05_L1TP_140041_20100119_20200825_02_T1	19/01/2010
LT05_L1TP_140041_20100204_20200825_02_T1	04/02/2010
LT05_L1TP_140041_20100220_20200824_02_T1	20/02/2010
LT05_L1TP_140041_20100409_20200825_02_T1	09/04/2010
LT05_L1TP_140041_20100425_20200825_02_T1	25/04/2010
LT05_L1TP_140041_20100511_20200824_02_T1	11/05/2010
LT05_L1TP_140041_20101103_20200823_02_T1	03/11/2010
LT05_L1TP_140041_20101205_20200823_02_T1	05/12/2010
End of Table	

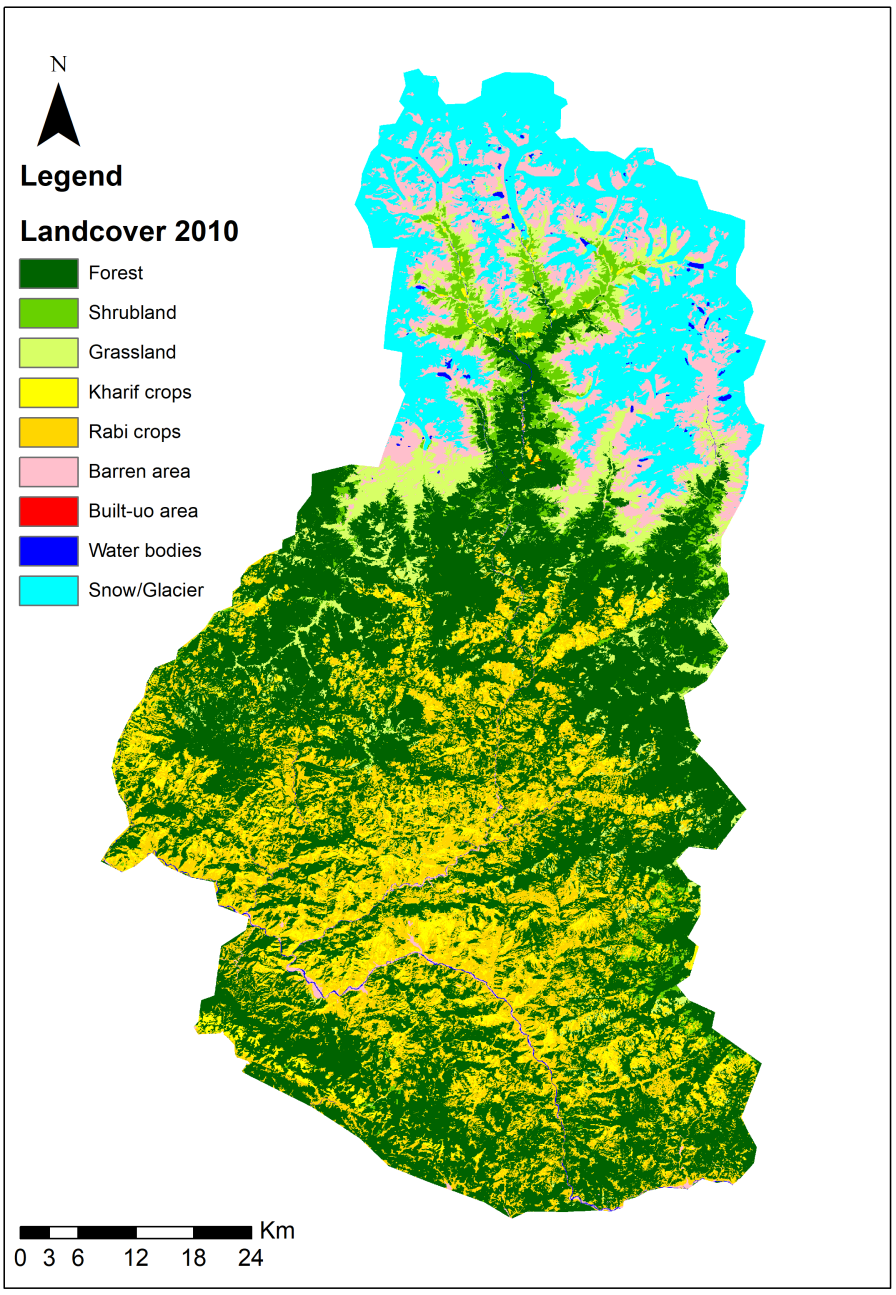

Figure 3.7: ICIMOD Land Cover map of 2010 - Updated version

Chapter 4

Method

4.1 Val Camonica soil erosion modelling

4.1.1 Framework

The Figure 4.1 shows the global framework of the methodology followed to estimate soil erosion in Val Camonica.

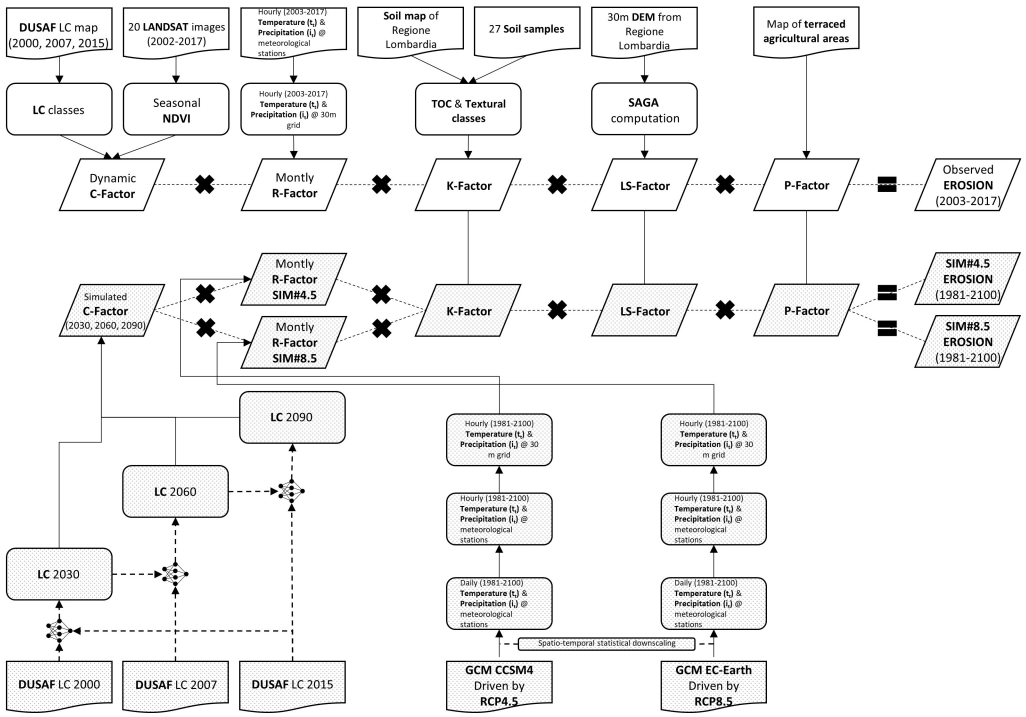

Figure 4.1: shows the experimental framework described in detail in the previous sections.

4.1.2 Standard modelling of potential soil erosion

The empirical Revised Universal Soil Loss Equation (RUSLE) is a very popular model to estimate the annual potential soil erosion rate due to rainfall (16). Although originally developed for agricultural application, today RUSLE is used as a general model to provide estimates also for non-agricultural lands at different spatial scales, even at continental scale (2). RUSLE estimates the annual potential soil erosion rate E [$t\ ha^{-1}\ yr^{-1}$] through five parameters, as shown in Equation 4.1:

$$E = R * K * LS * C * P \tag{4.1}$$

where:

- R is the rainfall erosivity [$MJ\ mm\ ha^{-1}\ h^{-1}\ yr^{-1}$], also called Rfactor, which is the driving force of erosion and is a function of precipitation rate, air temperature and snow cover dynamics;
- K is the soil erodibility [$t\ ha\ h\ ha^{-1}\ MJ^{-1}\ mm^{-1}$], also called K-factor, which describes the soil properties (i.e. soil structure and organic matter content) that influence the predisposition of soil to erosion;
- LS [$-$] is a dimensionless combined parameter, also called LS-factor, that describes the impact of slope length and slope steepness on soil erosion;
- C [$-$] is a dimensionless parameter, also called C-factor, that describes how land-use and land-cover protect the soil from erosion (lower C-factor values correspond to higher protection, thus to lower erosion);
- P [$-$] is a dimensionless parameter, also called P-factor, that describes the impact of soil conservation practices to reduce the potential erosion.

Precipitation data were used to estimate the daily rainfall erosivity at each rain gauge with the Rainfall Intensity Summarization Tool (RIST) code (USDA, 2017). Then, rainfall erosivity was aggregated at a monthly scale and spatialized on a 30 [m] grid with the inverse-square law, as shown in Figure 4.2a (R1). When organic matter content, texture, structure and permeability are known, soil erodibility can be estimated with equations [4.2-4.3] (14); (16):

$$K = \frac{2.1 * 10^{-4} * M^{1.14} * (12 - OM) + 3.25 * (s-2) + 2.5 * (p-3)}{100} * 0.1317 \tag{4.2}$$

where:

- OM [%] is the organic matter content;
- s is the soil structure class (s=1: very fine granular, ..., s=4: blocky, platy or massive);
- p is the permeability class (p=1: very rapid, ..., p=6: very slow);

- M is the textural factor computed as:

$$M = (M_{silt} + M_{vfs}) * (100 - M_c) \tag{4.3}$$

  - $M_c[\%]$ is the fractional content of clay (particle size < 0.002 [mm]);
  - $m_{silt}[\%]$ is the fractional content of silt (0.002[mm] $\leq$ particle size < 0.05 [mm]);
  - $m_{vfs}[\%]$ is the fractional content of very fine sand (0.05 [mm] $\leq$ particle size < 0.1 [mm]);

All this information was not available for our study area, therefore the K-factor map made by JRC (3) was resampled from its 500 [m] spatial resolution to 30 [m] spatial resolution (Figure 4.2b) (K1). The original resolution of 500m was considered adequate due to the lower spatial variability (35) of this parameter with respect to the others. The resampling was performed just to match the other parameter resolution. In the literature we can find several different formulations for estimating the LS-factor. It is quite common using the equation proposed by (63), which takes into account the unitary catchment area as input in each cell:

$$LS = (m+1)\left(\frac{U_{in}}{22.13}\right)^m \left(\frac{sin(\theta)}{sin(5^\circ)}\right)^n \tag{4.4}$$

where:

- $U_{in}[m^2 m^{-1}]$ is the contributing area to the cell for perimeter unit;
- 22.13 [m] is the length of the RUSLE standard parcel;
- $\theta[^\circ]$ is the cell slope;
- 5° is the slope of the RUSLE standard parcel;
- m and n are empirical coefficients (in literature typical values are $0.4 \leq m \leq 0.6$ and $1.0 \leq n \leq 1.3$).

In this study were used m=0.4 and n=1.3 as suggested by (64)(**?**). Figure 4.2c shows the map for LS-factor (LS1). In traditional RUSLE each land-cover class is assigned a unique and static C-factor, usually retrieved from literature. In this work, the C-factor is assigned using the DUSAF land-cover/land-use map of 2015 and tabulated data extracted from (2) and (65) as summarized in (1). Table 4.1 reports the correspondences between land cover classes and C-factor and Figure 4.2d shows its geographic distribution.

Table 4.1: Tabulated C-factor values assigned to each DUSAF land cover classes (column "C-factor (DUSAF)") and tabulated C-factor ranges for each DUSAF land cover classes (column "C-factor range") (1). C-factor values sources are (a) the parametrization proposed for Italy by (2), the central value of the C-factor range values for Europe from (b) (3) or (c) (4). The land cover classes without (a),(b) or (c) are classes not included in above cited studies but where there can not be any soil erosion (urbanized areas or water bodies).

C-Factor			
Land cover class name	**Land cover class code**	**C-factor (DUSAF)**	**C-factor range**
Continuous urban fabric	111	0.00000	0.00
Discontinuous urban fabric	112	0.00000	0.00
Industrial or commercial units	121	0.00000	0.00
Road and rail networks and associated land	122	0.00000	0.00
Port areas	123	0.00000	0.00
Airports	124	0.00000	0.00
Mineral extraction sites	131	0.00000	0.00
Dump sites	132	0.00000	0.00
Construction sites	133	0.00000	0.00
*Degraded Areas not used and not vegetated	134	0.00000	0.00
Beaches, dunes, sands	331	0.00000_b	0.00
Bare rocks	332	0.00000_b	0.00
Glaciers and perpetual snow	335	0.00000_b	0.00
Water course	511	0.00000	0.00
Water bodies	512	0.00000	0.00
Green urban areas	141	0.00100_c	
Inland marshes	411	0.00100_c	
*Silvicolture	224	0.00130_a	
Broad-leaved forest	311	0.00130_a	0.0001-0.003
Coniferous forest	312	0.00130_a	0.0001-0.003
Mixed forest	313	0.00130_a	0.0001-0.003
*New forest	314	0.00130_a	
Sport and leisure facilities	142	0.01000_c	
Transitional woodland-shrub	324	0.2420_a	0.003-0.05
Natural grasslands	321	0.4160_a	0.01-0.08
Moors and heathland	322	0.05500_b	0.01-0.1
Pastures	231	0.09880_a	0.05-0.15
Fruit trees and berry plantations	222	0.20000_b	0.1-0.3
Olive groves	223	0.21630_a	0.1-0.3
Sparsely vegetated areas	333	0.25090_a	0.1-0.45
Non-irrigated arable land	211	0.33500_b	

Vineyards	221	0.34540_a	0.15-0.45
End of Table			

*not in Corine Land Cover classification

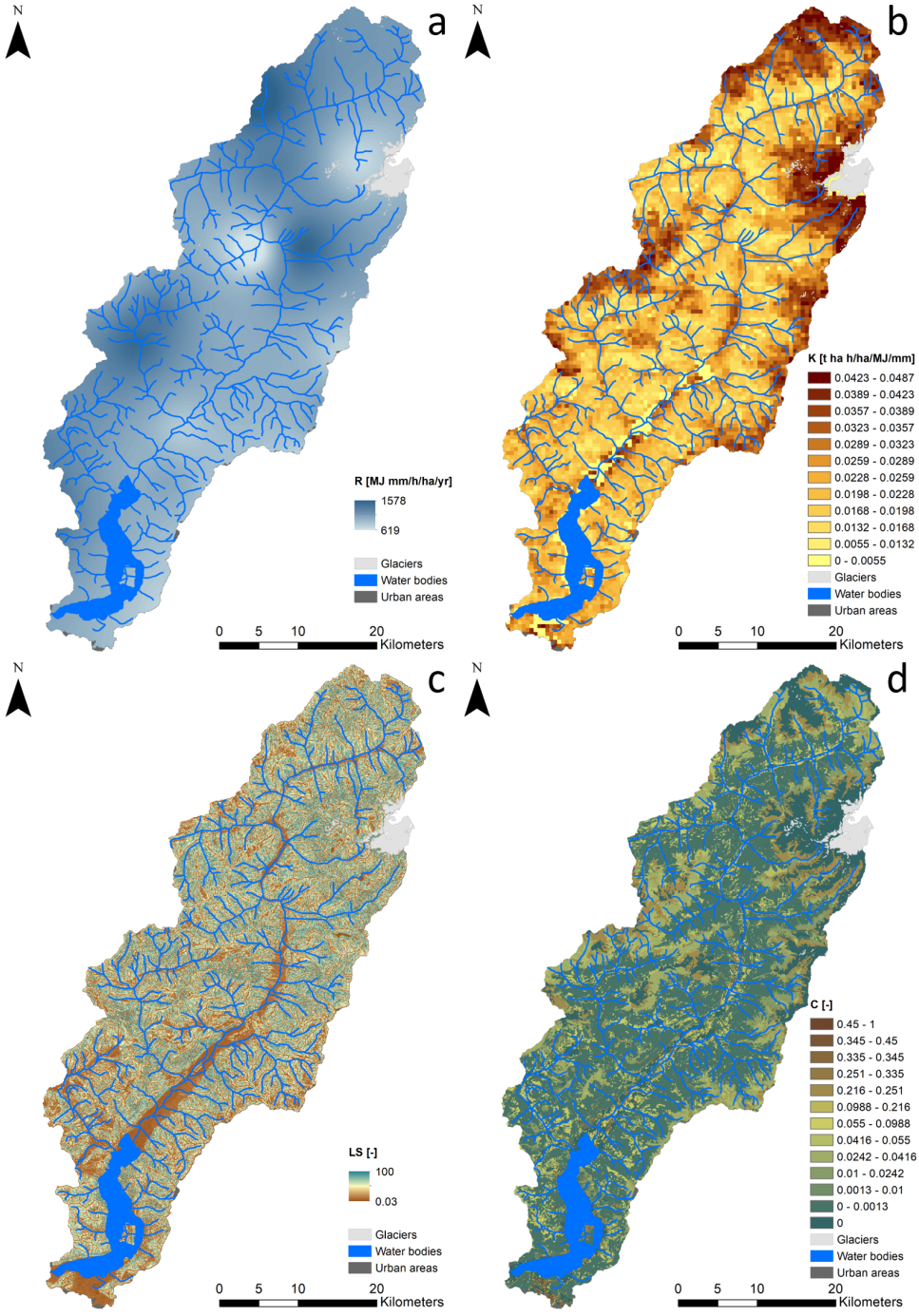

Figure 4.2: Parameters of classic RUSLE: a) rainfall erosivity (R1 parametrization); b) soil erodibility (K1 parametrization); c) slope length and steepness (LS1 parametrization); d) cover management type (C0 parametrization).

Finally, it is very difficult to define P-factor. In fact, although few authors tried to estimate the P-factor from land cover information, this parameter is usually not considered in erosion studies because its estimation needs a very detailed knowledge of the territory. Consequently, it is usually set to P=1.

4.1.3 The Dynamic RUSLE model

RUSLE was originally developed for the estimation of soil loss in flat agricultural areas. While retaining the same formal equation of the original RUSLE [1], here an alternative parametrization called Dynamic RUSLE (D-RUSLE) is proposed. D-RUSLE includes the effects of rainfall intensity, snow cover dynamics and land-cover/land-use changes in time, thus reflecting more realistically precipitation erosivity and the sheltering effect of snow and vegetation seasonal dynamics. All the meteorological data recorded by rain gauges and thermometers are spatialized with the inverse-square law on a 30 [m] grid and temperatures are spatialized using a dynamic gradient estimated at each simulation step. The R-factor (R2) is computed at monthly scale using the equation proposed by Sun, Cornish, & Daniell (2002), where units are modified to get erosion rate in [$t\ ha^{-1}\ month^{-1}$] instead of [$kg\ m^{-2}\ month^{-1}$] (25):

$$R = \sum_{t=1}^{n_h} 0.138 * i_{e,t}^2 \tag{4.5}$$

where:

- $i_{e,t}$ is the effective hourly intensity of precipitation;
- n_h is the monthly number of hours.

The effective hourly intensity of precipitation $i_{e,t}$ computed with equations [4.6-4.7]:

$$SWE_t = SWE_{t-1} + \begin{cases} +min\left(max\left(0; \frac{T_{sup}-T_t}{t_{sup}-t_{inf}}\right); 1\right) & IF\ i_t\ >\ 0, \\ -min\left(max\left(0; c_m * (T_t - T_m)\right); SWE_{t-1}\right) & IF\ i_t\ =\ 0 \end{cases} \tag{4.6}$$

$$i_{e,t} = \begin{cases} 0 & IF\ SWE_t\ >\ 0, \\ i_t & IF\ SWE_t\ =\ 0 \end{cases} \tag{4.7}$$

where:

- $SWE_t[mm]$ is the snow water equivalent;
- $T_t[^\circ C]$ is the air temperature;
- $T_{inf}[^\circ C]$ is the temperature below all the precipitation is snow ($T_{inf} = -3\ [^\circ C]$);
- $T_{sup}[^\circ C]$ is the temperature above all the precipitation is rain ($T_{sup} = 0\ [^\circ C]$);
- $T_m[^\circ C]$ is the temperature above snow melting starts ($T_m = 0\ [^\circ C]$);
- $i_t[mm\ h^{-1}]$ is the measured precipitation by rain gauge (=rain+snow);
- $C_m[mm\ h^{-1}\ ^\circ C^{-1}]$ is the snow melting rate ($C_m = 0.18\ [mm\ h^{-1}\ ^\circ C^{-1}]$);

Equation [4.6] describes the snow water equivalent dynamics in terms of accumulation (when $i_t > 0$) and melting (when $i_t = 0$), which is used as a proxy for snow cover dynamics. Equation [4.7] provides the estimated effective hourly intensity of precipitation (i_e) as function of precipitation, air temperature and snow cover (Figure 4.4a). The K-factor (K2) is assigned to the different soil textural classes derived from the official soil map of Regione Lombardia according to information retrieved from literature (5), after local validation (Figure 4.3). For the 27 soil samples we measured total organic carbon (TOC), acidity (pH) and texture. Then the laboratory results were compared with the information extracted from the soil map (here texture is expressed as texture classes) (Figure 4.4b). Since the accordance was reasonably good, to each cell was assigned a K-factor value based on its TOC and texture class provided by the soil map, as reported in Table 4.2.

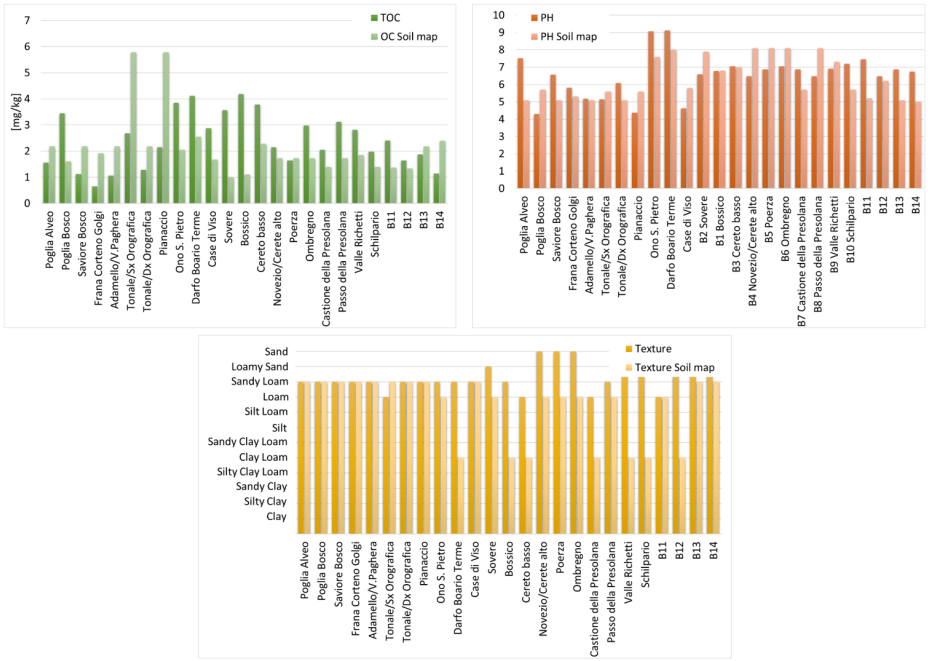

Figure 4.3: Comparison between TOC, pH and textural class measured for the 27 soil samples and retrieved from the soil map of Regione Lombardia.

Table 4.2: K-factor values for different textural classes and TOC content (modified from (5)

Soil Texture Classes	K-factor	
	For TOC $< 1.16\,[\%]$	For TOC $> 1.16\,[\%]$
Sand	0.0040	0.0015
Loamy Sand	0.0066	0.0053
Sandy loam	0.0184	0.0158
Loam	0.0448	0.0342
Silt loam	0.0540	0.0487
Silt	0.0561	0.0514
Sandy clay loam	0.0263	0.0263
Clay loam	0.0435	0.0369
Silty clay loam	0.0461	0.0395
Sandy clay	0.0277	0.0277
Silty clay	0.0356	0.0345
Clay	0.0316	0.0277

The LS-factor (LS2) is estimated with the terrain analysis/hydrology module available in SAGA (System for Automated Geoscientific Analyses) that use the popular formulation proposed by Desmet and Govers (1996) (Figure 4.4c). Equation [4.8] takes into account flow accumulation from upslope cells:

$$LS = \frac{\left(A_{in} + D^2\right)^{\left(\frac{\beta}{beta+1}+1\right)} - \left(A_{in}\right)^{\left(\frac{\beta}{beta+1}+1\right)}}{x^{\left(\frac{\beta}{\beta+1}\right)} * 22.13^{\left(\frac{\beta}{\beta+1}\right)} * D^{\left(\frac{\beta}{\beta+1}+2\right)}} \tag{4.8}$$

$$\beta = \frac{\frac{sin(\theta)}{sin(5^\circ)}}{0.56 + 3 * [sin(\theta)]^{0.9}} \tag{4.9}$$

$$x = |sin(a)| + |cos(a)| \tag{4.10}$$

$$S = \begin{cases} 10 * sin(\theta) + 0.03 & IF\ \theta\ <\ 5[^\circ] \\ 16.8 * sin(\theta) - 0.5 & IF\ \theta \geq\ 5[^\circ] \end{cases} \tag{4.11}$$

where:

- $A_{in}[m^2]$ is the contributing area to the cell;
- *D [m]* is the cell size;
- *22.13 [m]* is the length of the RUSLE standard parcel
- $a[^\circ]$ is the cell orientation (aspect);
- $\theta[^\circ]$ is the cell slope

- $5[^{\circ}]$ is the slope of the RUSLE standard parcel.

Finally, C-factor is estimated at 30 [m] spatial resolution as a dynamic variable using only satellite Remote Sensing data (C1) and aggregating satellite Remote Sensing data with land cover maps (C2). Compared to the classic "static" modelling of the cover management factor (C0), satellite data allow the inclusion of its seasonal and inter-annual dynamics. C-factor could be estimated from NDVI using equation [12] proposed by (28) (C1), as shown in Figure 4.4d:

$$C = e^{-\alpha * \frac{NDVI}{\beta - NDVI}} \tag{4.12}$$

where:

- α and β are empirical coefficients (suggested values for Italy are $\alpha = 2$ and $\beta = 1$).

However, it is well-known that equation [4.12] might result in unreliable overestimations of C-factor (i.e. underestimation of the sheltering effect of vegetation) when NDVI is less than 0.65, which could in turn reflect in unreliable overestimation of soil erosion rates. Moreover, satellite images collected over mountain areas in Winter have very large shadows, which lead to unreliable estimation of NDVI, thus unreliable estimation of C-factor and, finally, unreliable estimation of erosion rates. For those reasons, equation [4.12] seems not suitable to study soil erosion in mountain areas, and would be the preferred method only in if no information on land cover is available. Here a new method for the estimation of C-factor based on NDVI time series is proposed, where information on land cover is used as a priori knowledge to constrain C-factor values (66) (C2). Satellite images are pre-processed through standard radiometric calibration and atmospheric corrections for non-flat terrain. All the images are grouped into two macro-seasons: Spring/Summer (from March to August) and Autumn/Winter (from September to February), and snow cover and clouds were masked. The study area, as most of the Alpine environment, is characterized by the presence of many steep and narrow valleys and during Autumn/Winter almost half of the territory is completely shadowed or snowed up. That can produce undersatureted data (i.e. null values in shadowed areas) or oversaturated data (i.e. flat values in snowy areas). For this reason, Autumn/Winter NDVI values were unreliable and thus replaced with synthetic values reconstructed combining Spring/Summer observations and DUSAF land cover classes. For each Autumn/Winter image, we selected the closest Spring/Summer image and the closest DUSAF among the three maps available. Then I calculated the pixel-based ratio between Autumn/Winter NDVI and Spring/Summer NDVI, excluding shadowed or snowy image pixels. Next, we computed the average value of the ratio between Autumn/Winter NDVI and Spring/Summer NDVI for each land cover class. Finally, I reconstructed a synthetic pixel-based map for Autumn/Winter NDVI by multiplying the Spring/Summer NDVI by the average ratio computed at the previous step, for each land cover class. Once reconstructed the time series of NDVI, I estimated the C-factor time series. For each land cover class of DUSAF I defined a range of possible values for C-factor $[C_{n,min}, C_{n,max}]$ based on past studies (see Table 4.1 and (1)) and then linearized C-factor with NDVI as follows:

$$C_n = \begin{cases} C_{n,max} & FOR\ NDVI\ <\ NDVI_{n,min} \\ C_{n,max} + \frac{NDVI - NDVI_{n,min}}{NDVI_{n,max} - NDVI_{n,min}} (C_{n,min} - C_{n,max}) & FOR\ NDVI_{n,min}\ \leq\ NDVI\ \leq\ NDVI_{n,max} \\ C_{n,min} & FOR\ NDVI\ >\ NDVI_{n,max} \end{cases} \tag{4.13}$$

where:

- $C_{n,min}[-]$ is the minimum C-factor value for land cover class n;
- $C_{n,max}[-]$ is the maximum C-factor value for land cover class n;
- $NDVI_{n,min}[-]$ is a threshold for land cover class n set to $\mu_{NDVI} - \sigma_{NDVI}$
- $NDVI_{n,max}[-]$ is a threshold for land cover class n set to $\mu_{NDVI} + \sigma_{NDVI}$

To guarantee time and space coherence of seasonal C-factor estimates, I use the same thresholds for both Spring/Summer and Autumn/Winter images. Pixel corresponding to non-vegetated classes in DUSAF were assigned a null C-factor (Figure 4.4e).

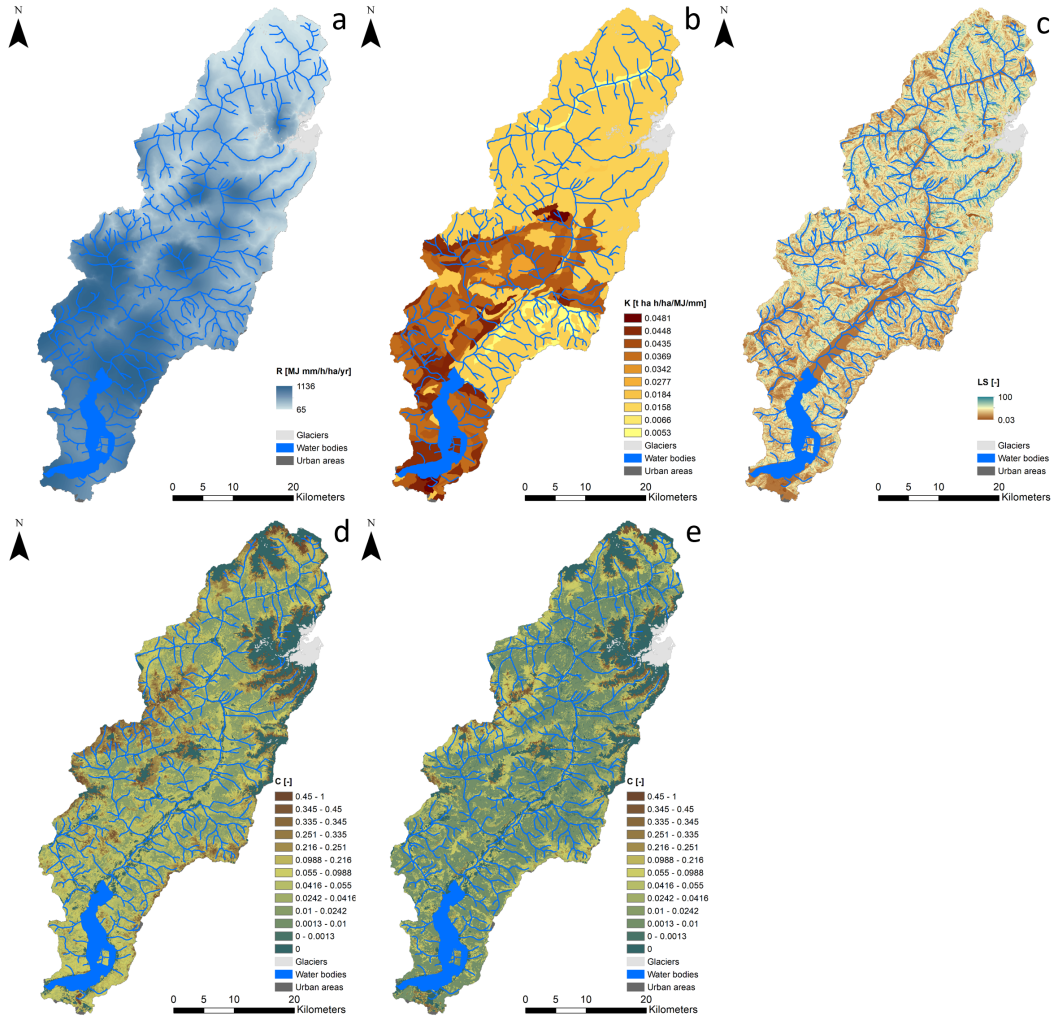

Figure 4.4: Parameters of D-RUSLE: a) rainfall erosivity (R2 parametrization); b) soil erodibility (K2 parametrization); c) slope length and steepness (LS2 parametrization); d) cover management type (C1 parametrization); e) cover management type (C2 parametrization).

4.1.4 Projection of Precipitation, Temperature, and Rainfall Erosivity

The climate projections generated from GCMs driven by RCPs have a coarse spatial resolution (more than 100 km x 100 km) and a coarse temporal resolution (daily), which are not suitable for simulating erosion rates al local scale with D-RUSLE. In addition, it is known that precipitations simulated by GCMs usually suffer from bias and poor intermittence and variability. Thus, they have improper representation of mean rainfall values on the ground (bias), poor representation of the sequence of dry and wet days (intermittence), and poor representation of the variability of rainfall in time (variability). To overcome all these issues, we used a stochastic time random cascades (SSRCs) approach (67) to correct and downscale in space and time our climate simula-

tions. This technique first downscales in the spatial domain the daily time series of precipitation and temperature simulated by the climate projections, from the GCM grid to the pinpoint meteorological stations. Then downscales the time series of meteorological stations in the temporal domain, from daily to hourly (67). With reference to precipitation, the SSRCs correct the bias by applying a constant (multiplicative) term to force the mean simulated daily precipitation from the GCM to equate the observed value at the rain gauges. Intermittence is then introduced with a binomial generator to evaluate the probability of wet (or dry) spells, thus reproducing the alternance of days with and without precipitation. Finally, the variability of rainfall is reproduced with a "strictly positive" log-normally distributed generator, which properly depicts the variance of rainfall intensity during wet days. Overall, the downscaled simulations provide a series of precipitation that are statistically equivalent (in terms of mean value, dry/wet spell dynamics, and rainfall variance) to the observed precipitation at rain gauges and can be thus used confidently for hydrological simulation. With reference to temperatures, the simulated downscaled temperatures well mimic the observed trend at the thermometer stations, unless for an additive bias which was corrected using a monthly Delta-T approach (68). Finally, both the downscaled precipitation and temperature time series were further corrected for altitude using lapse rates to preserve their observed (at meteorological stations) vertical structure, and then spatialized from the rain gauges/thermometer stations to the whole study area with a spatial resolution of 30 m. For every rain gauge and thermometer station, we calibrated the SSRCs models using the observed hourly data in the period 2003–2017. The so tuned models were then used to downscale in space and time precipitation and temperature simulated by the nine climate scenarios in the period until 2100. Overall, to estimate future climate change we generated time series for four 30-years periods: 1981–2010 was used as the reference period, while the statistics of the periods 2011–2040, 2040–2070, and 2071–2100 were used as representative of future climate change. Once simulated the climate scenarios, we simulated rainfall, snowfall, and snow cover dynamics with D-RUSLE and then computed monthly maps of rainfall erosivity using the equation proposed by Sun, Cornish, and Daniell (69):

$$R = \sum_{t=1}^{n_h} 0.138 * i_{e,t}^2 \tag{4.14}$$

where:

- $i_{e,t}$ [mm h^{-1}] is the effective hourly intensity of precipitation;
- n_h is the monthly number of hours.

4.1.5 Land Cover Scenarios

Automatic machine learning was used for projecting future land cover maps. For this task, many different methods are described in the literature (e.g., logistic regression, similarity-weighted instance-based machine learning), but neural networks are the most commonly used and are also known to outperform the other methods (70);(71). For this simulation, the land change modeler

Table 4.3: Main land cover transitions and land cover persistences highlighted by the change detection analysis for the period 2000-2015.

Sub-Model	Land Cover Transitions	Land Cover Persistences
Sub-model 1 (arable lands)	Non-irrigated arable land → Pastures Pastured → Discontinuous urban fabric; Pastured → Non-irrigated arable land.	Non-irrigated arable lands; Pastures
Sub-model 2 (forests)	Pastured → Broad-leaved forest; Coniferous forest → Mixed forest; Coniferous forest → Moors and heathland; Coniferous forest → Transitional woodlandshrub; Transitional woodland-shrub → Broad-leaved forest; Transitional woodland-shrub → Mixed forest	Pastures; Coniferous forest; Transitional woodland-shrub
Sub-model 3 (grasslands)	Pastures → Natural grassland; Pastures→ Transitional woodland-shrub; Moors and heathland → Natural grassland; Bare rocks → Sparsely vegetated areas; Sparsely vegetated areas. Sparsely vegetated areas → Natural grasslands; Sparsely vegetated areas → Transitional woodland-shrub; Sparsely vegetated areas → Bare rocks.	Pastures; Moors and heathland; Bare rocks;

module of TerrSet (72) was used. First, the land cover changes that occurred in the past with a classic change detection analysis between DUSAF 2000 and DUSAF 2015 were quantified. To avoid meaningless changes, we retained only class transitions with a total geographic extension larger than 3000 cells (i.e., more than 2.7 [km2], about 0.15% of the study area). This analysis highlighted 16 main land cover transitions and 7 main land cover persistences, which were grouped in the three sub-models reported in Table 4.3.

Then, for each of the three sub-models I built a multi-layer perceptron neural network (MLPNN). All the MLP-NNs were designed with three input neurons (elevation, slope, and aspect) and a hidden layer with six neurons. Different formulation of the NN structure were tested, with more input parameters (distance from river, distance from roads, and population), but they resulted to be non-significant in explaining the Land Cover transitions. The output layer used to predict the probability of land cover changes in the future had as many neurons as the number of potential land cover transitions and potential land cover persistences (5 for sub-model #1, 9 for sub-model #2, and 11 for sub-model #3). Figure 4.5 shows the neural network design.

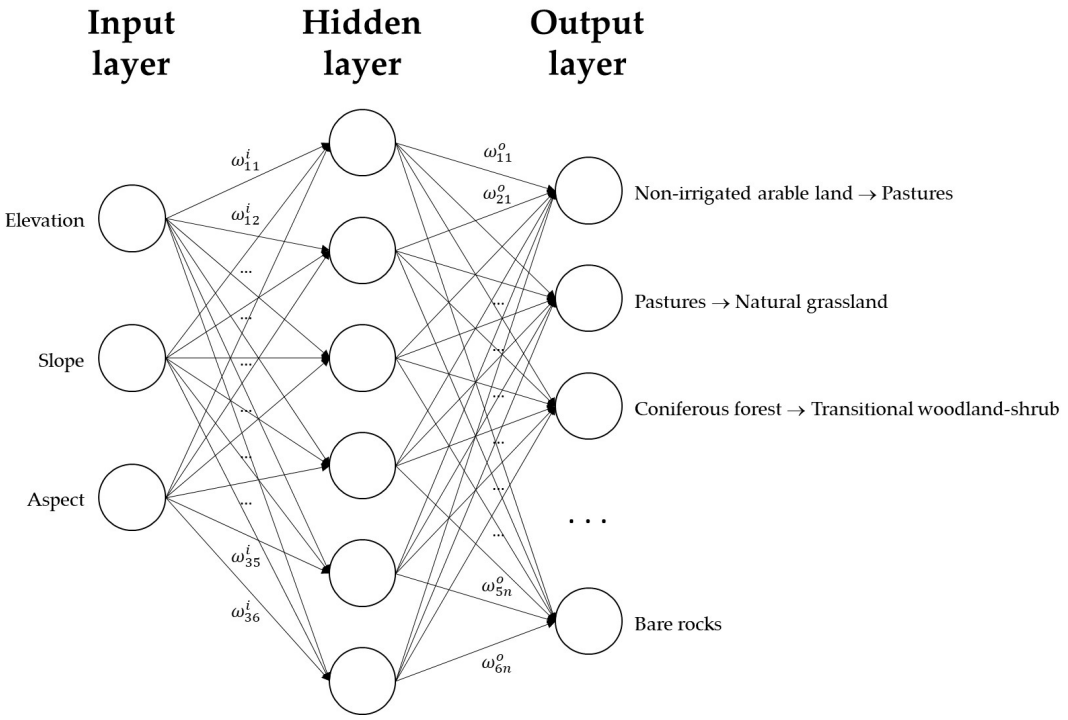

Figure 4.5: Multi-layer perceptron neural network used for generating future land cover scenarios.

The third step was the training of the networks (one for each sub-model) to set the optimal weights (ω^k_{ij}). A set of training data and a set of testing data were automatically extracted from the reference land cover maps. To avoid sub-optimal solutions or an unstable training process, we used a learning rate of 0.0001. Moreover, I used a momentum of 0.5 for increasing numerical stability and for reducing volatility over the training epochs. Once trained, the neural networks were used to generate a set of land cover transition/persistence potentials [44]. Finally, using the past land cover changes and the modelled transition/persistence potentials, the future land cover map was predicted with a Markov Chain. Specifically, having evaluated the historical land cover changes from time t1 to time t_2, the Markov Chain estimated the portion of land that is expected to transition from one class to another other, between the time t2 and a future time t_3 (73). By repeating the process mentioned above, I simulated one land cover (LC) map for each of the 30-years simulation period: LC 2030, LC 2060, and LC 2090. For limiting error propagation in the simulation process, the MLP-NNs were trained with at least one real land cover map (i.e.,

DUSAF). Therefore, for the simulation at year 2030 the networks were trained with the DUSAF 2000 and DUSAF 2015 maps, DUSAF 2007 and the simulated land cover map for year 2030 (LC 2030) were used for predicting the land cover at year 2060 (LC 2060), and DUSAF 2015 and the simulated map at year 2060 (LC 2060) were used for the last prediction at year 2090 (LC 2090). Moreover, since initialization of the neural network is prone to numerical issues, we repeated each simulation five times, for a total of 15 simulations for every 30-years period. The final land cover maps were generated by retaining the modal value of each land cover simulation. While this is not a Monte Carlo simulation, however the multiple repetitions allowed us to get a more accurate prediction of the future land cover, minimizing the intrinsic error of the single stochastic simulation.

As a result of our simulations, I described the dynamics of the cover management factor through the following land cover maps:

- 1981-2010 (reference period): DUSAF 2000 map;
- 2011-2040: simulated LC 2030 map;
- 2041-2070: simulated LC 2060 map;
- 2071-2100: simulated LC 2090 map.

Clearly, future projections of the cover management factor cannot exploit the satellite observations for reproducing the seasonal dynamics of vegetation. Thus, the cover management factor was estimated by assigning a fixed value to land cover classes at each simulation period (Table 4.1) (74);(75). This means that our simulations only considered the trend of the C-factor and were not able to reproduce its seasonal variability.

4.2 Nepal parameters modelling

As mentioned in the introduction, this part of the work was less focused on the soil erosion estimation per se, but more on how to compute the parameters of the model, in situation where data availability is less abundant and reliable.

4.2.1 Meteorological data processing

With regard to meteorological data, I used a daily time series of precipitation and air temperature derived from a reanalysis of data from 1981 to 2010. This dataset (HIAWARE) is provided with a resolution of 5 km for the entire study area.

Through a cubic interpolation the resolution of temperature and precipitation data was upgraded to 30 m taking into consideration the local temperature gradient thanks to a 30 m resolution Digital Elevation Model (DEM) from SRTM mission.

4.2.2 Calibration of the SWE model

The SWE model described in equation 4.6 was calibrated with the help of 15 Landsat satellite images, over the period 2009-2010. Instead of having a fixed values for each parameter of the model, a possible range was defined (table 8.1) and the model was performed with a random initialization of the parameters. A classification process was applied to the 15 Landsat images, in order to derive, for each image, a map of the snow covered areas. The classification was performed starting from the work of (76) and further tuned for the study area, where topography has an important role, with many areas in shadow. The classification (see Equations 4.15 - 4.16 - 4.17) is pixel based with a set of threshold on the NDSI index and the reflectance bands of the landsat images.

$$Areas\ classified\ as\ snow = \begin{cases} NDSI > 0.75 \\ R(red) > 0.045 \\ R(green) > 0.035 \end{cases} \tag{4.15}$$

$$Areas\ classified\ as\ clouds = \begin{cases} -0.27 < NDSI < 0.3 \\ R(green) > 0.3 \\ R(SWIR) > 0.4 \end{cases} \tag{4.16}$$

$$NDSI = \frac{R(green) - R(SWIR)}{R(green) + R(SWIR)} \tag{4.17}$$

where:

- R(green) -> represents the pixel reflectance in the green band;
- R(red) -> represents the pixel reflectance in the red band;

Parameters	**Range**	**Tuned Value**
T_{inf}[°C]	[-7;0]	-7
T_{sup}[°C]	[-4;7]	3
T_m[°C]	[-5;0]	-5
C_m[mm d^{-1} $°C^{-1}$]	[2.5;15]	14

Table 4.4: Bayesian optimization parameters

- R(SWIR) -> represents the pixel reflectance in the short wave infrared.

These maps were used as true value reference. The outputs of the model, saved at the same date of the satellite images, were then compared with the maps of snow cover derived from the Landsat images, excluding the areas covered by clouds, and the confusion matrix, for each pair, was computed and the F1-score derived. Through a bayesian optimization process the 4 parameter of the model were tuned in order to maximize the F1-score. At the end of the process the average value of F1-score was 0.5860, and the values of the 4 parameters are shown in table 4.4.

4.2.3 ICIMOD Land cover maps processing

As far as the land cover maps, provided by ICIMOD, are concerned, a classification process was performed in order to improve the quality of the earlier versions of Land cover maps. Exploiting the power of Google Earth Engine cloud computing, all the Landsat available images from 1985 to 2015 were used to perform the classification. A SAM algorithm was used to classify the area of agriculture and forest. The output of the first classification was compared with the statistical data of the agricultural areas. An iterative process was then applied to modify the threshold value of the SAM classification in order to minimize the difference between the output of the classification and the statistical data.

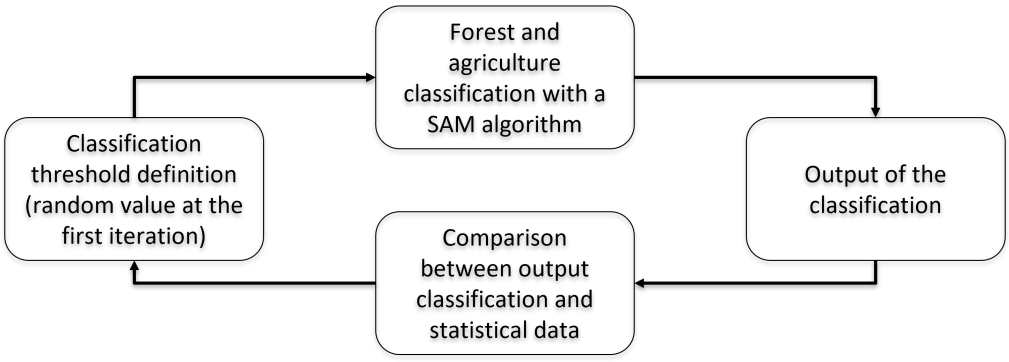

Figure 4.6: Classification process of land cover maps

The publication, by ICIMOD, of the recently update LC maps, which proved to be accurate, made unnecessary the classification process. Nonetheless the process proved to be a useful

Hyper-parameter	Value
Epochs	50
Dropouts on each hidden layer	20%
Loss	Sparse categorical crossentropy
Optimizer	Adam
Metric	Accuracy
Batch size	32

Table 4.5: Hyper-parameter of the three Neural Network models

way to improve the accuracy of a poor land cover map, integrating satellite information with statistical data.

4.2.4 Land Cover Projection

To simulate the future evolution of Land Cover three model of Neural Network were tested, with python. All the model share the same structure:

- 16 input parameters
  - DEM
  - Slope
  - Aspect
  - Distance from roads
  - Distance from rivers
  - Population
  - Input map pixels
  - For each pixel of the input map the 9 pixels in the 3x3 kernel surrounding the pixel
- 3 hidden layers
  - 16 nodes
  - Relu activation function
- Output layer
  - Softmax activation function
  - 9 classes

The hyper-parameters of the three models are shown in table 4.5.

The first 6 input parameters are the same for each model, while the parameters related to the input map, and the true value map used to train the NN are different for each model.

4.2.4.1 Model 1

The first model used, as input map, the map of 1990 and the map of 2000, stacked together in a single array, in order to increase the numerosity of the training sample. As true value the map of 2000 and the map of 2010 were stacked together in a single array. Of the input and true value maps, 90% of the pixels were used to train the model, while 10% were used to validate it.

The performance of the model 1 is shown in table 4.6.

It is important to underline that between the input map (1990 + 2000) and the true value map (2000 + 2010) 83% of the study area does not change its state. For this reason in the training phase the class invariability is over-represented, and the neural network might just be trained to maintain the same land cover class.

Score	Value
Loss	0.5130
Accuracy	0.8384
Validation Loss	0.4253
Validation Accuracy	**0.8676**

Table 4.6: Model 1 performance

Score	Value
Loss	0.9927
Accuracy	0.6504
Validation Loss	0.7721
Validation Accuracy	**0.7189**

Table 4.7: Model 2 performance

4.2.4.2 Model 2

A second Neural Network model was tested to bypass the eventuality of over representation of the invariability of land cover. In this model only 10% of the pixels that don't change their land cover class between the input map and the true value map are taken into consideration in the training process, while for the validation the entire area is considered.

The performance of model 2 is shown in table 4.7.

4.2.4.3 Model 3

The last model tested had in input only the 1990 land cover map, and as true value reference the 2010 land cover map. This process cuts in half the dataset dimension but excludes the land cover map of 2000 that showed some misclassified area. Despite the time step, between the input and the output, doubling up this model showed a better performance with an accuracy on the validation set of 80%

The performance of model 3 is shown in table 4.8.

Score	Value
Loss	0.7541
Accuracy	0.7191
Validation Loss	0.5758
Validation Accuracy	**0.8071**

Table 4.8: Model 3 performance

Chapter 5

Result

Figure 5.1 compares the estimates of potential soil erosion rates simulated with D-RUSLE (SIM_07) and RUSLE (SIM_01). D-RUSLE takes into account a regional-based mapping of the parameters, snow cover dynamics and both inter-annual and intra-annual variability of land cover as follows:

- Rainfall erosivity is modelled using the R2 parametrization, as it separates rainfall and snow contribution to soil erosion, thus providing seasonal and altitude discrimination which are important in the mountainous environment;
- Soil erodibility is modelled using the K2 parametrization, as it can be applied to other case studies;
- Slope length and steepness is modelled using the LS2 parametrization, as suggested by reference works in the literature;
- Cover management type are modelled using the C2 parametrization, as satellite images can greatly improve the dynamic estimation of the sheltering effect of vegetation;
- Conservation practice is neglected in the absence of field information.

Although the two approaches provide a different range of erosion rates variability, due to different parameters' formulation, their spatial patterns can be compared. That is shown in Figure 5.1: overall, higher erosion areas are predominantly located at higher altitudes on slopes, while lower erosion values characterize valley areas. Nevertheless, the adoption of D-RUSLE (Figure 5.1a) lead to a decrease in soil loss estimates of more than 8 times with respect to classic RUSLE (Figure 5.1b), with a larger difference in the high elevation areas. This difference decreases to a fifth in the lake area (Figure 5.2).

5.1 Benchmark

Potential soil loss rate is a difficult quantity to measure in the field, thus we used the most recent reference data available for Europe (2) as benchmark (Figure 5.1c). The comparison

between JRC erosion estimates on Val Camonica area and D-RUSLE (SIM_07) estimates shows a general agreement on the location of the areas more prone to erosion, given the different spatial resolution of the studies: 100-m (aggregated) for JRC output (2)) and 30-m for our results (25). No data values (almost 16% of the study area) in JRC map are due to a lack of data in the C-factor estimate (77).

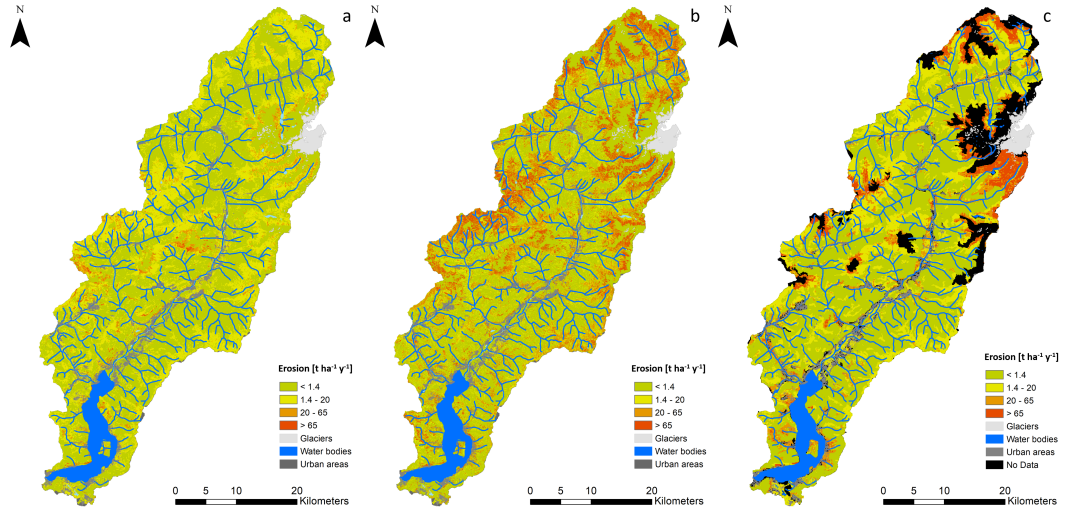

Figure 5.1: Comparison of potential soil erosion maps simulated with: a) D-RUSLE (SIM_07), b) classic RUSLE (SIM_01) and c) JRC erosion estimates.

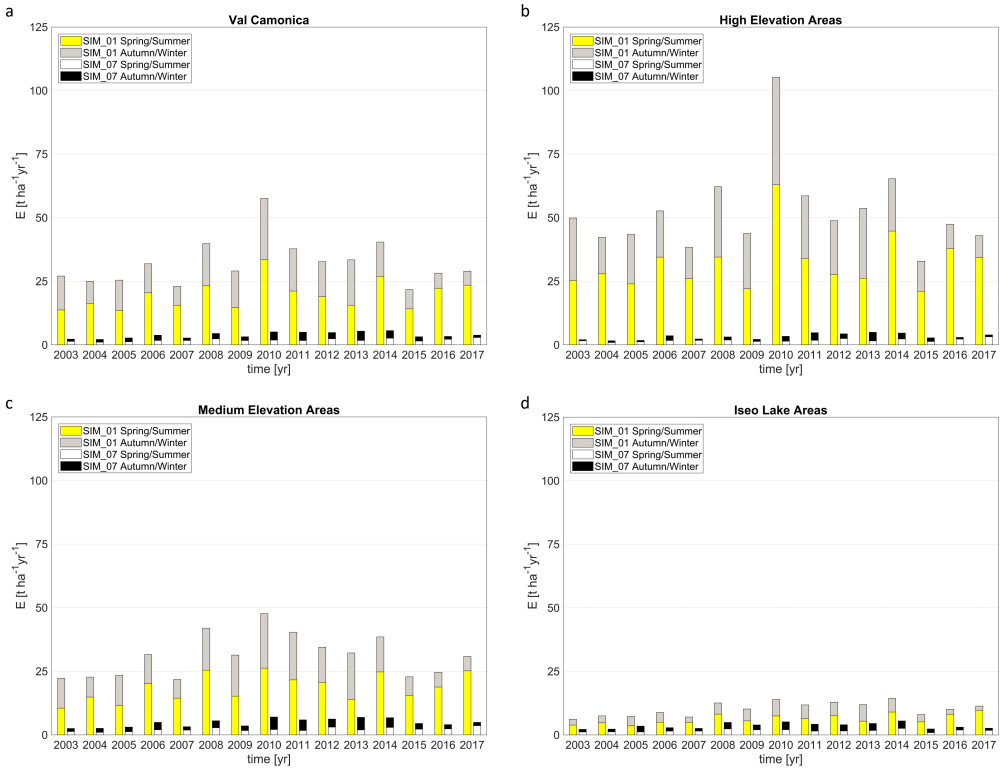

Figure 5.2: Comparison of potential soil erosion rates (2003-2017) computed for Spring/Summer and Autumn/Winter with D-RUSLE (SIM_07) and classic RUSLE (SIM_01).

5.2 Sensitivity analysis

Several simulations are used to evaluate the models' sensitivities to different parametrization of input variables (Table 5.1). Simulation code SIM_01 corresponds to classic RUSLE, here used as reference, while simulation code SIM_07 corresponds to the D-RUSLE model here proposed. Intermediate simulations (from SIM_02 to SIM_06) show the impact on the estimate of different input variables parametrization.

Table 5.1: Different combinations of the parameters

Simulation code	Parameters' code			
	R-factor	C-factor	K-factor	LS-factor
SIM_01	R1	C0	K1	LS1
SIM_02	R2	C0	K1	LS1
SIM_03	R1	C0	K2	LS1
SIM_04	R1	C0	K1	LS2
SIM_05	R1	C1	K1	LS1
SIM_06	R1	C2	K1	LS1
SIM_07	R2	C2	K2	LS2

Sensitivity to R-factor

On average, the R2 parametrization produces lower rainfall erosivity compared to the R1 parametrization ($\mu_{R1} = 1094\ [MJ\ mm\ ha^{-1}\ h^{-1}\ yr^{-1}]$, $\mu_{R2} = 439\ [MJ\ mm\ ha^{-1}\ h^{-1}\ yr^{-1}]$), with almost comparable dispersion ($\sigma_{R1} = 141\ [MJ\ mm\ ha^{-1}\ h^{-1}\ yr^{-1}]$, $\sigma_{R2} = 163\ [MJ\ mm\ ha^{-1}\ h^{-1}\ yr^{-1}]$) In particular, the R1 parametrization overestimates rainfall erosivity in Autumn/Winter, as it does not distinguish between snow and rainfall and does not account for snow cover. Consequently, using the R2 parametrization (SIM_02) instead of the standard R1 (SIM_01) produces lower potential soil erosion rates. The most significant decrease is located in high and medium elevation areas, where soil loss rates decrease of 75% and 63% respectively, due to the modelling of snowfall and snow cover dynamics. A minor decrease (47%) is retrieved in the lake areas, as a result of lower altitudes that limit the snow occurrence and foster the snow cover melting process. Overall, using R2 instead of R1 had the highest impact on simulations (-68% of potential soil erosion rates).

Sensitivity analysis respect to K-factor

The effect of using K2 parametrization (SIM_03) instead of more complex and detailed K1 parametrization (SIM_01) is not uniform in the whole study area. Overall, K2 parametrization produces a lower spatial variability, as each polygon of the reference soil map is assigned a single value (Figure 4.3b). Nevertheless, statistics are comparable ($\mu_{K1} = 0.0228\ [t\ ha\ h\ ha^{-1}\ MJ^{-1}\ mm^{-1}]$, $\mu_{K2} = 0.0236\ [t\ ha\ h\ ha^{-1}\ MJ^{-1}\ mm^{-1}]$, , $\sigma_{K2} = 0.0112\ [t\ ha\ h\ ha^{-1}\ MJ^{-1}\ mm^{-1}]$ More in detail, the use of K2 parametrization has a mixed impact: potential soil loss rate decreases of almost 50% in high elevation areas, while increases of almost 60% in the Iseo Lake area. The impact of K2 parametrization is limited in medium elevation areas (-16%). Therefore, moving from K1 to K2 parametrization the overall potential erosion rate decreases by 27%. This reflects the different spatial distribution of K-factor using K1 and K2 parametrizations, as shown in Figure 4.1b and Figure 4.3b.

Sensitivity analysis respect to LS-factor

LS2 parametrization (SIM_04) is very different from the classic LS1 parametrization (SIM_01), both in terms of mean ($\mu_{LS1} = 29.6$, $\mu_{LS2} = 13.0$) and standard deviation ($\sigma_{LS1} = 38.7$, $\sigma_{LS2} = 15.0$). However, past studies suggested that LS2 is to be preferred for sub-basin scale analysis (77). The adoption of LS2 parametrization has an important impact on the modelling, with an overall decrease of potential soil erosion rate of about 55%, regardless the elevation ranges.

Sensitivity analysis respect to C-factor

Simulation SIM_06 (C2) returns slightly increasing rates with respect to SIM_01 (C0). Nevertheless, values are almost comparable among all the three altitude areas (+19%, +13% and -6% for SIM_06 in high altitude, in medium altitude and in lake areas respectively), as all both approaches rely on the use of land cover classes to limit C-factor variability. On the contrary, simulation SIM_05 (C1) returns a prominent increase (nearly three times) in soil loss rates estimates, due to no boundaries that limit the variability of C-factor estimates. This effect is particularly evident in the lake area (+296%), characterized by a predominance of forests, and slightly decreases when moving to higher altitudes (+188% for medium elevation area and +127% for high elevation area), where forests are replaced by sparsely vegetated areas. On the whole area, the use of C2 parametrization showed a limited effect of average soil erosion rates (+12%), but differences between C0 and C2 parametrization are evident when data are analysed at seasonal scale as in Section 6.2.

5.3 Projection of Precipitation, Temperature, and Rainfall Erosivity

Comparing the simulated mean annual precipitations at the rain gauges (2003-2017) with observations (2003-2017), we found the following biases in the downscaling process: 3.7% for ECHAM6, 3.9% for EC-Earth, and 4.5% for CCSM4. In the same period, at the thermometers the biases were: 0.1 °C (ECHAM6 and EC-Earth) and 0.0 °C (CCSM4). Among the nine climate scenarios, GCM CCSM4 driven by RCP4.5 projected the smaller changes for annual precipitation (-1.8%) and temperature (+1.4 °C) at 2071-2100. On the other hand, GCM EC-Earth driven by RCP8.5 projected the larger changes for annual precipitation (+8.4%) and temperature (+4.0 °C) at 2071–2100. For this reason, our analysis focused only on these two extreme scenarios: GCM CCSM4 driven by RCP4.5 (hereafter referred to as SIM4.5) is our best-case scenario and GCM EC-Earth driven by RCP8.5 (hereafter referred to as SIM8.5) is our worst-case scenario. All the other scenarios lie in the between. Figure 5.3 shows a comparison between the 30 m spatialized mean annual observed vs. simulated precipitation and temperature in the period

2003–2017. On the one hand, precipitation was slightly underestimated in all the domain. On the other hand, observed and simulated temperatures show a good agreement, being characterized by a negative gradient with elevation. Tables 5.2 and 5.3 summarize the numerical results. Figures 5.4 and 5.5 report the mean precipitation and temperature anomalies simulated with SIM#4.5 and SIM#8.5 at 2011–2040, 2041–2070, and 2071–2100. The baseline is the reference simulated period (1981–2010).

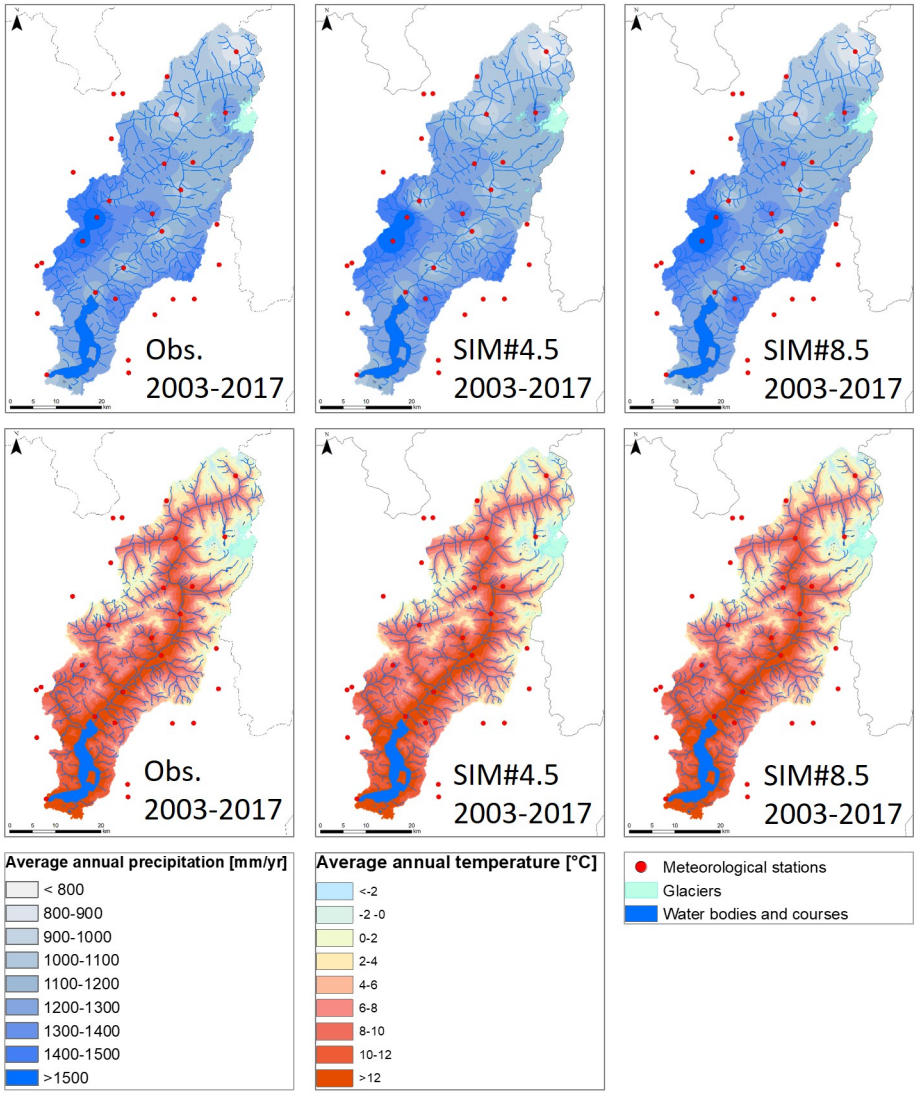

Figure 5.3: Estimates of mean annual precipitation (first row) and temperature (second row) based on observations in 2003–2017 (first column); statistical downscaling of SIM#4.5 in 2003–2017 (second column) and statistical downscaling of SIM#8.5 in 2003–2017 (third column).

Table 5.2: Mean annual precipitation [$mm\ yr^{-1}$] based on spatially distributed observations and simulated climate.

	Study Area	**North Region**	**Center Region**	**South Region**
Observed (2003-2017)	1212	1108	1274	1274
SIM#4.5 (2003-2017)	1199	1086	1254	1277
SIM#8.5 (2003-2017)	1200	1091	1253	1270

Table 5.3: Mean annual temperature [°C] based on spatially distributed observations and simulated climate.

	Study Area	**North Region**	**Center Region**	**South Region**
Observed (2003-2017)	7.0	4.3	7.1	10.4
SIM#4.5 (2003-2017)	7.0	4.3	7.0	10.3
SIM#8.5 (2003-2017)	7.0	4.3	7.1	10.3

Figure 5.6 shows a comparison between the spazialized R-factor based on observations vs. simulations for the period 2003–2017. Figure 5.7 reports the projections for SIM4.5 and SIM8.5. The simulated maps show spatial patterns that are similar to those observed but the R-factors are underestimated by about 26% in both SIM#4.5 and SIM#8.5 (Table 5.4).

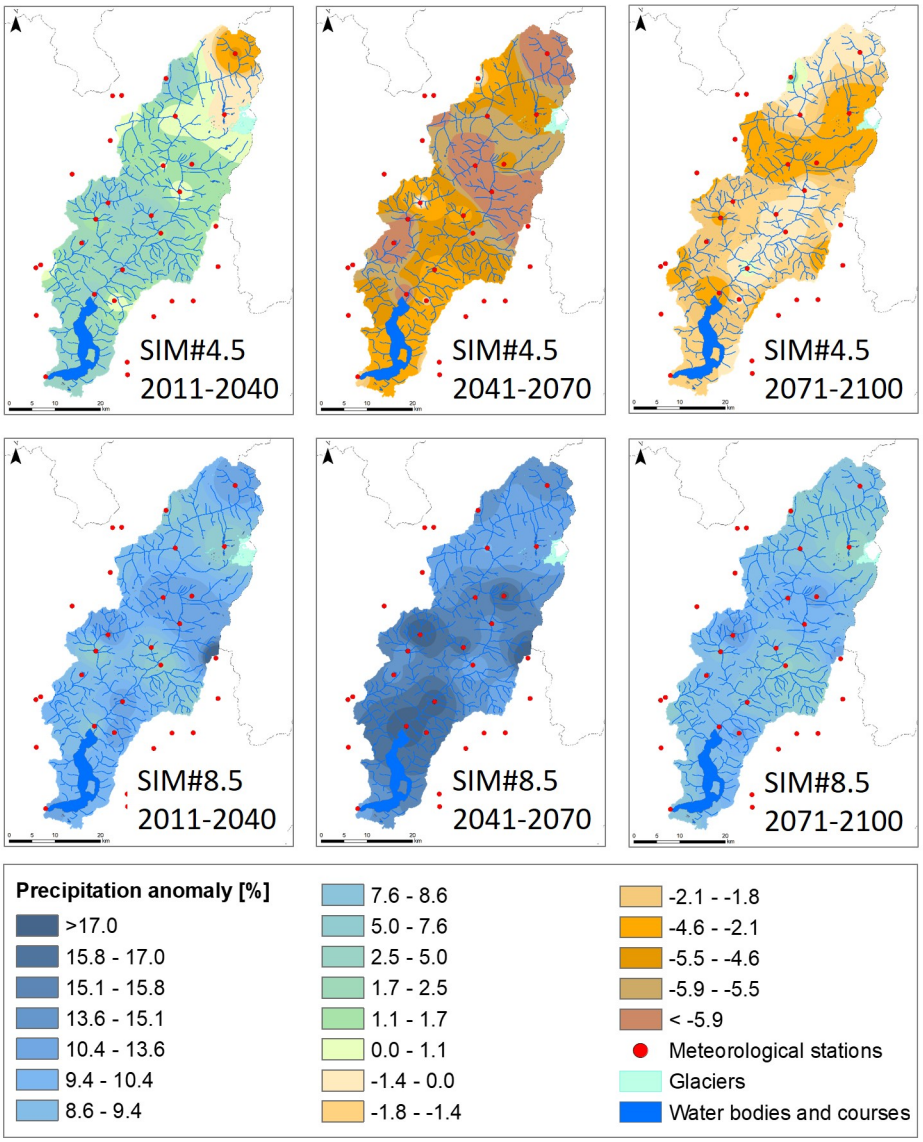

Figure 5.4: Mean precipitation anomalies compared to the reference period (1981–2010): simulated with SIM#4.5 (first row) and SIM#8.5 (second row) at 2011–2040 (first column), 2041–2070 (second column), and 2071–2100 (third column).

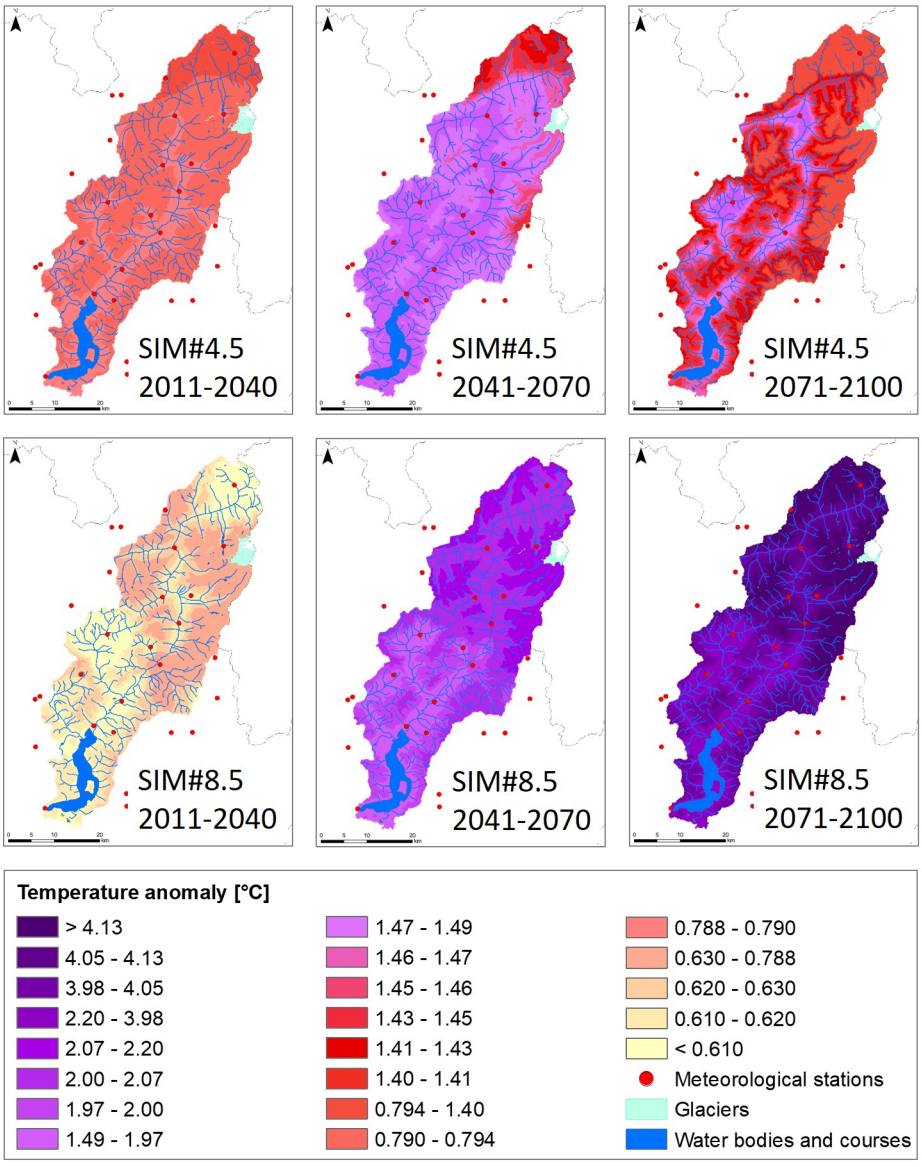

Figure 5.5: Mean temperature anomalies compared with the reference period (1981–2010): simulated with SIM4.5 (first row) and SIM8.5 (second row) at 2011–2040 (first column), 2041–2070 (second column), and 2071–2100 (third column).

Table 5.4: Mean R-factor [$MJ\ mm\ ha^{-1}\ h^{-1}\ yr^{-1}$] based on spatially distributed observations and simulated climate.

	Study Area	North Region	Center Region	South Region
Observed (2003-2017)	436	296	463	581
SIM#4.5 (2003-2017)	231	310	331	447
SIM#8.5 (2003-2017)	325	197	328	482

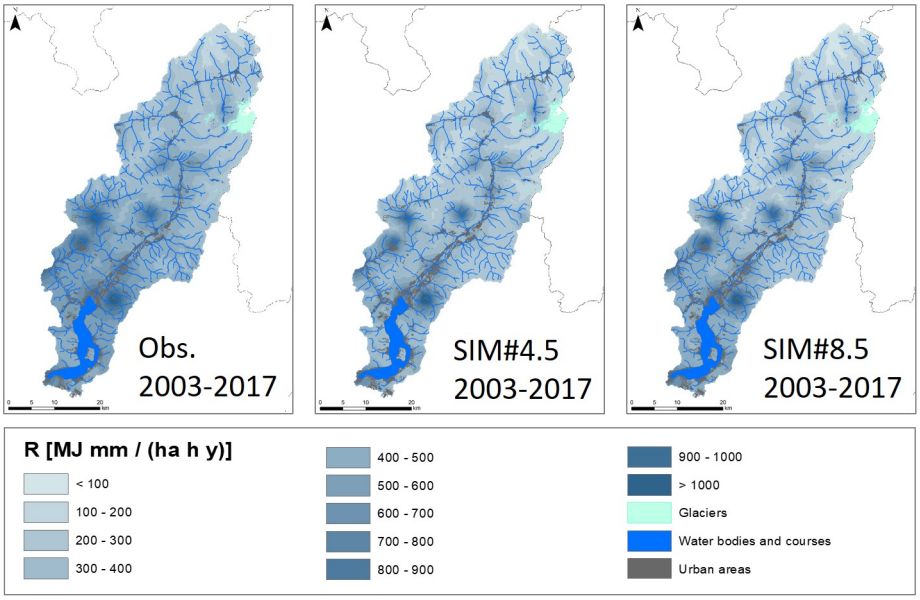

Figure 5.6: Estimates of R-factor based on observations in 2003–2017 (left); statistical downscaling of SIM#4.5 in 2003–2017 (center); statistical downscaling of SIM#8.5 in 2003–2017 (right).

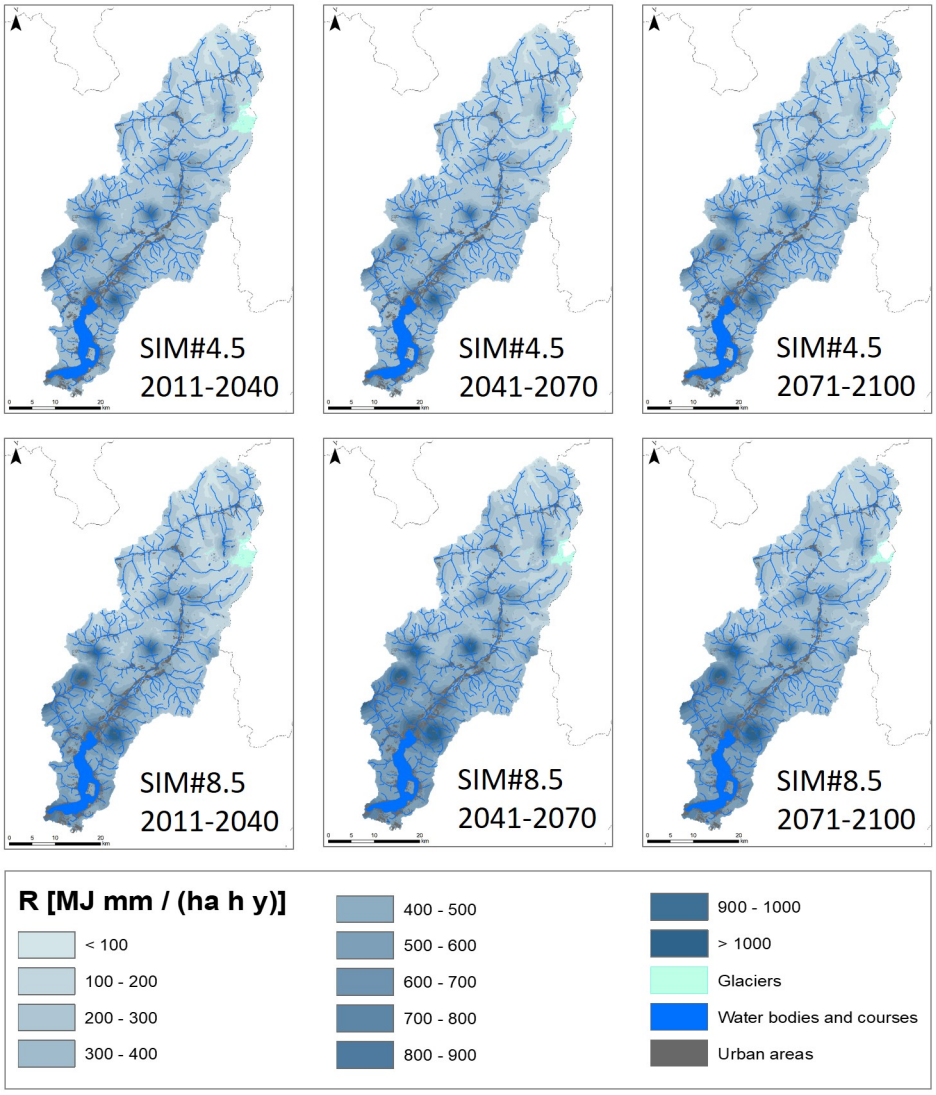

Figure 5.7: R-factor simulated with SIM4.5 (first row) and SIM8.5 (second row) at 2011–2040 (first column), at 2041–2070 (second column), and at 2071–2100 (third column).

5.4 Projections of Future Land Cover and Cover Management Factor

The change detection analysis of past land cover (Figures 5.8 and 5.9) revealed that sparsely vegetated areas and pastures respectively reduced by 14% and 17%. They were almost replaced by natural grasslands, which increased by about 27%, and by moor and heathlands, which increased almost 8%. On the other hand, transitional woodland-shrubs, bare rocks, glacier and perpetual snow areas remained almost stable. With reference to future land cover simulations, results show the following temporal trends (Figures 5.8 and 5.9):

- Sparsely vegetated areas and pastures continue to reduce almost constantly until 2090;
- Natural grasslands continue to increase almost constantly until 2090;
- Moors and heathlands show a rapid increase until 2060 and then a slower increase until 2090;
- Transitional woodland-shrubs and bare rocks show respectively a minimal increase and a minimal decrease in the simulation periods;
- Glacier and perpetual snow considerably reduce (from -37% in the first 30-years period to - 52% in the third 30-years period), in accordance with the expected retreat of the Adamello glacier and the disappearance of the Ortles glacier.

Consequently, Figure 5.10 shows the dynamics of the C-factor computed with the observed land cover maps (DUSAF 2000, DUSAF 2007, DUSAF 2015) and the projected C-factor computed with the future land cover maps (LC 2030, LC 2060, LC 2090). Overall, projections show a gradual decrease of the mean C-factor for the whole study area (from 0.046 in 2000 to 0.033 in 2090), thus a gradual increase in the sheltering effect of vegetation cover toward soil erosion. The same result occurs when analyzing the three regions separately (from 0.052 to 0.035 for the North region, from 0.045 to 0.034 for the Center region, and from 0.040 to 0.030 for the South region).

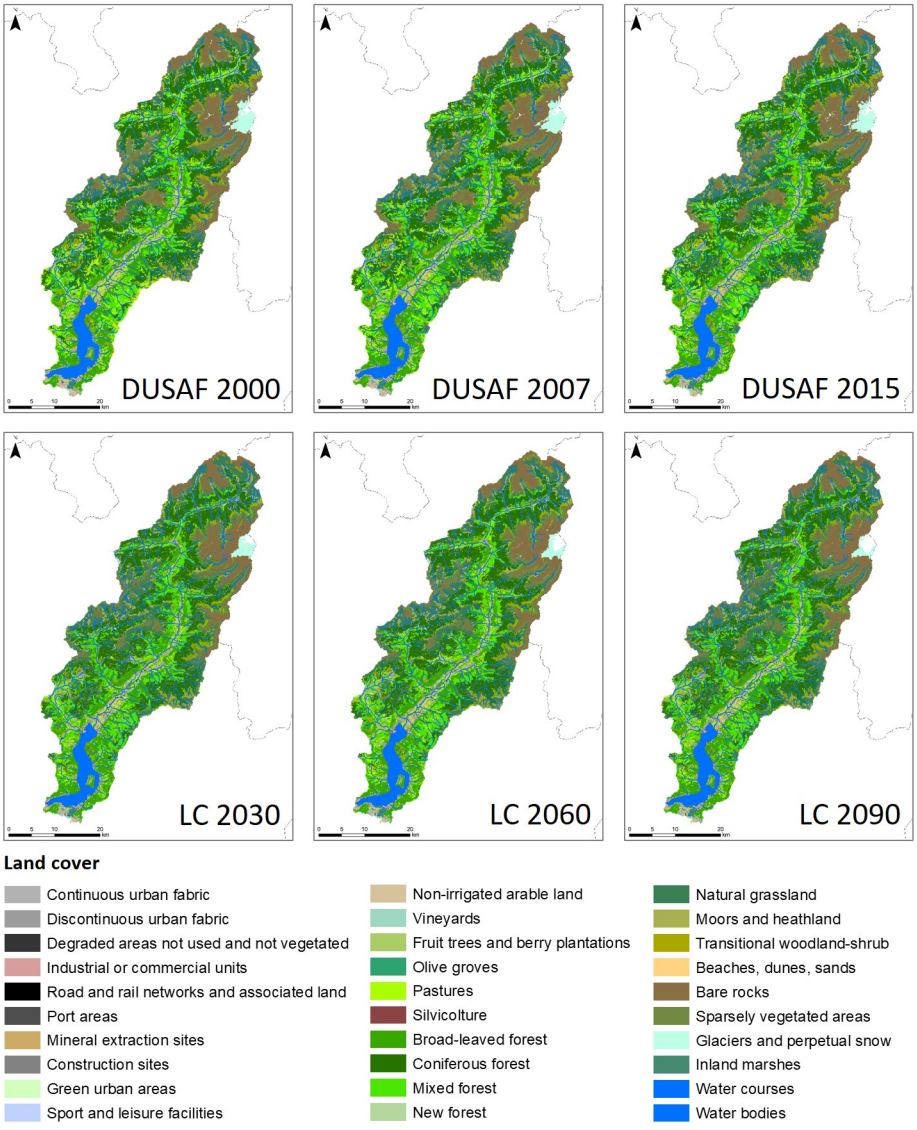

Figure 5.8: Past land cover (DUSAF) observed at 2000, at 2007, and at 2015 (first row); simulated land cover (LC) at 2030, at 2060, and at 2090 (second row).

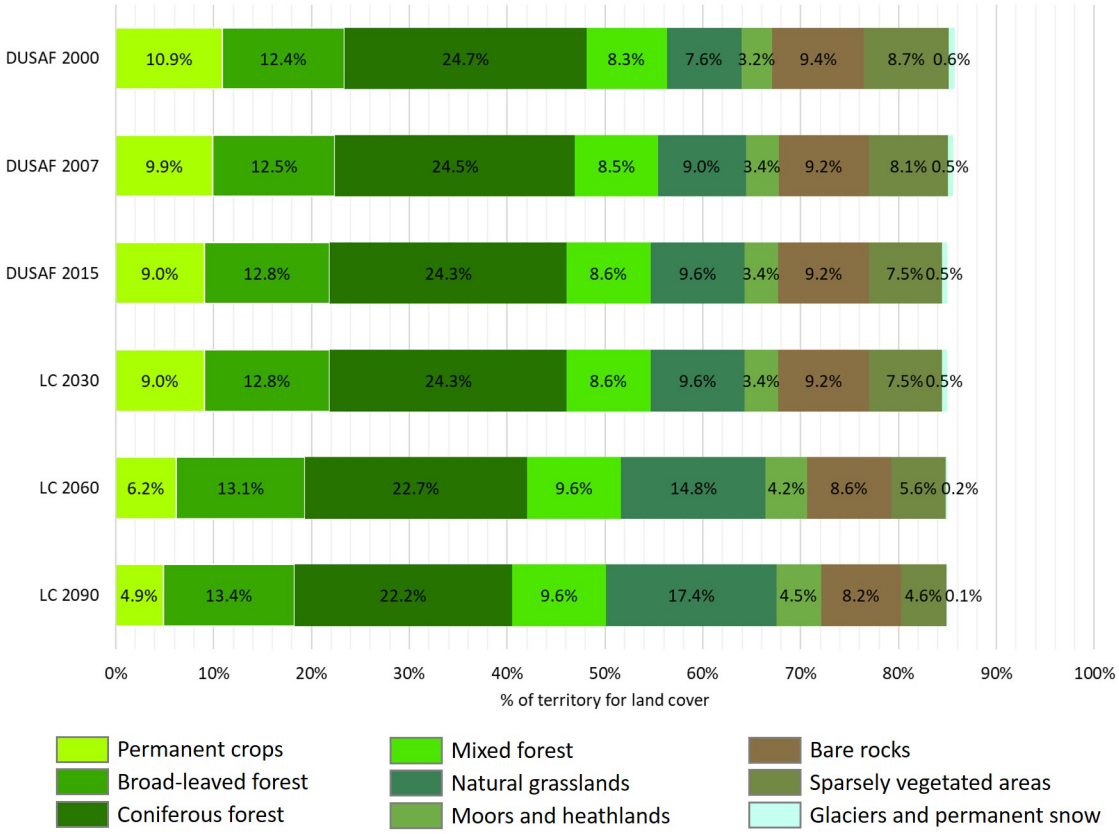

Figure 5.9: Most significant land cover classes at each observed (DUSAF) and simulated (LC) epoch.

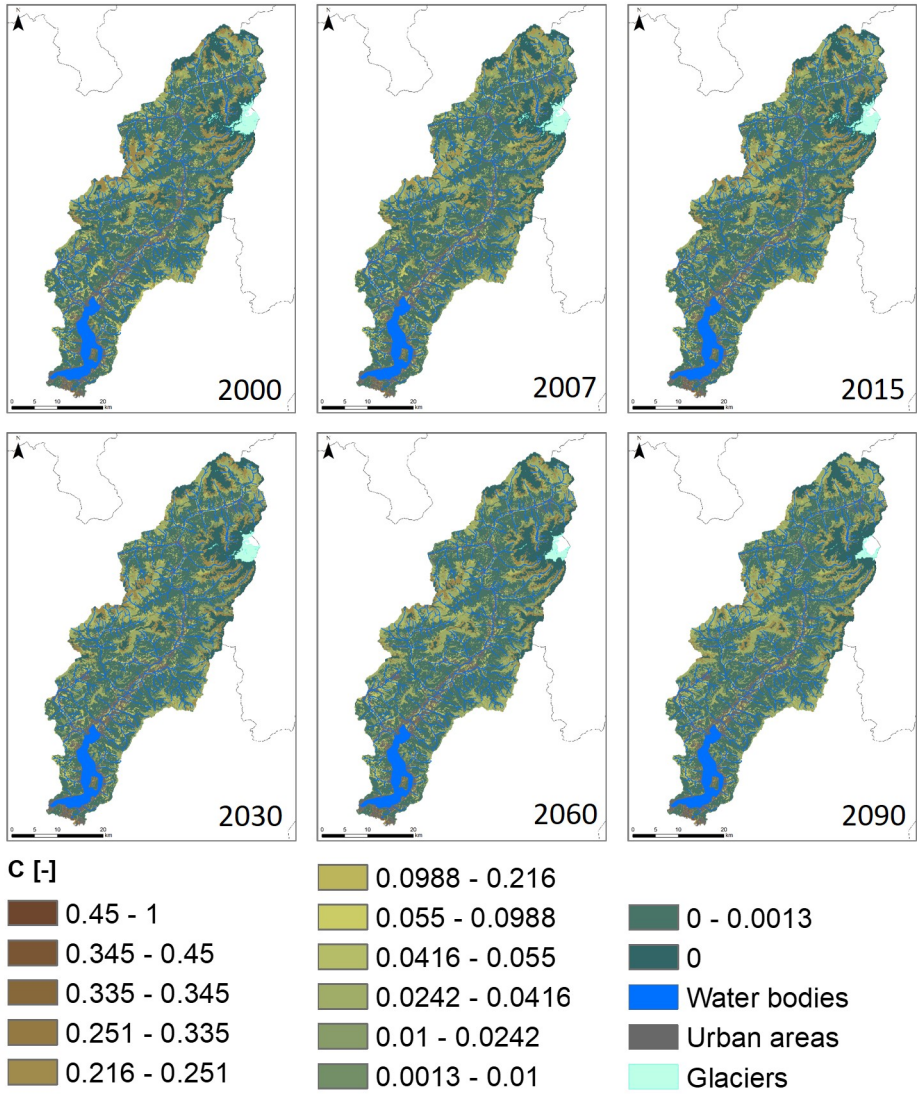

Figure 5.10: DUSAF based C-factor at 2000, at 2007, and at 2015 (first row) and LC based C-factor at 2030, at 2060, and at 2090 (second row).

5.5 Effect of Climate Projections on the Estimates of Soil Erosion

To evaluate the effects of climate change on soil erosion, independently from land cover changes, we run our simulations with a static land cover. In this case, we used the DUSAF 2015 for the whole simulated period (1981–2100). The erosion scenarios obtained with static land cover are hereafter referred to as SIM#4.5_D2015 and SIM#8.5_D2015, depending on the climate scenarios used. Figure 5.11 presents the comparison of observed (74);(75) vs. the simulated mean annual soil erosion rates for the period 2003–2017 and using the two climate scenarios SIM4.5 and SIM8.5. The simulated maps show spatial patterns that are similar to those observed, but the erosion rates are underestimated of about 29% in SIM#4.5_D2015 and 44% in SIM#8.5_D2015

(Table 5.5). As already mentioned, the overall underestimation is strictly related to the underestimation of the R-factor in the same period.

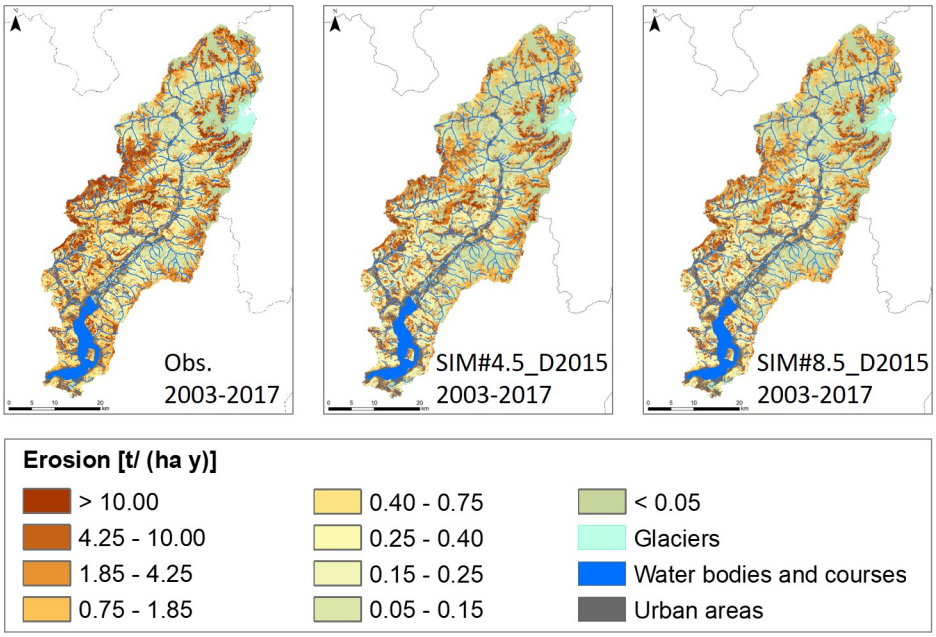

Figure 5.11: Estimates of mean annual soil erosion rates based on observations (left); and using erosion scenarios SIM#4.5_D2015 (center) and SIM#8.5_D2015 (right) with static land cover (DUSAF 2015).

Table 5.5: Mean observed and simulated annual erosion rates [$t\ ha^{-1}\ yr^{-1}$] with two climate scenarios and static land cover (DUSAF 2015).

	Study Area	**North Region**	**Center Region**	**South Region**
Observed (2003-2017)	3.78	3.22	4.64	3.64
SIM#4.5_D2015 (2003-2017)	2.67	2.08	3.08	2.94
SIM#8.5_D2015 (2003-2017)	2.63	1.89	2.94	3.02

More in details, Figure 5.12 reports the projected changes of erosion rates (baseline 1981–2010). Under the hypothesis of a static land cover, changes in erosion rates are only due to rainfall erosivity variability as stated in Equation (1). Expected mean erosion rates for the periods 2011–2040, 2041– 2070, and 2071–2100 are detailed in Table 5.6. According to SIM#4.5_D2015, the mean erosion rate of the study area is expected to remain almost constant. The Center region, on average, has the highest erosion rates, while the North region has the lowest rates. SIM#8.5_D2015 foresees a different scenario: the mean erosion rate of the study area is expected to grow until 2070, and then stabilize. In this case, the territory with the highest erosion rates is the South region, while the North region shows the lowest rates. As expected, the erosion rates predicted by SIM#8.5_D2015 and averaged on the study area exceed those of SIM4.5_2015 by 8% for the simulation period 2011–2040, by 28% for the simulation period 2041–2070 and by 23% for the simulation period 2071–2100. Finally, Figure 5.13 summarizes the percentages of the study area and regions where erosion is predicted to increase, decrease, or remain stable.

Table 5.6: Mean erosion rates [$t\ ha^{-1}\ yr^{-1}$] according to climate projections.

Simulation Periods		Study Area	North Region	Center Region	South Region
SIM#4.5	1981-2010	2.69	2.03	3.20	2.96
	2011-2040	2.63	1.99	3.13	2.87
D2015	2041-2070	2.57	2.06	2.96	2.77
	2071-2100	2.68	2.11	3.19	2.84
SIM#8.5	1981-2010	2.61	1.78	2.96	3.26
	2011-2040	2.84	1.97	2.96	3.26
D2015	2041-2070	3.30	2.31	3.76	4.04
	2071-2100	3.30	2.36	3.76	3.96

5.6 Combined Effects of Climate and Land Cover Projections on the Estimates of Soil Erosion

To evaluate the combined effects of climate and land cover changes, we run our simulations with a time-dependent land cover. In this case, we used LC 2030 as representative for the 30-year period 2011–2040, LC 2060 as representative for the 30-year period 2041–2070 and LC 2090 as representative for the 30-year period 2071–2100. For the control period (1981–2010) we assumed the observed land cover given by DUSAF 2000. The erosion scenarios obtained by combining the two climate scenarios with dynamic land cover are hereafter referred to as SIM#4.5_LC and SIM#8.5_LC. Figure 5.14 shows the comparison of observed (74);(75) vs. simulated mean annual soil erosion rates for the period 2003–2017 and extracted from those generated from the erosion scenarios SIM#4.5_LC and SIM#8.5_LC. The simulated maps show spatial patterns that are similar to those observed, but the erosion rates are still underestimated (Table 5.7). Nevertheless, the better performances of SIM#4.5_LC vs. SIM#4.5_D2015 and of SIM#8.5_LC vs. SIM#8.5_D2015 (cf. Tables 3 and 8) are due to the land cover dynamics (i.e., DUSAF 2000 from 2003 to 2010 and LC 2030 from 2011 to 2017).

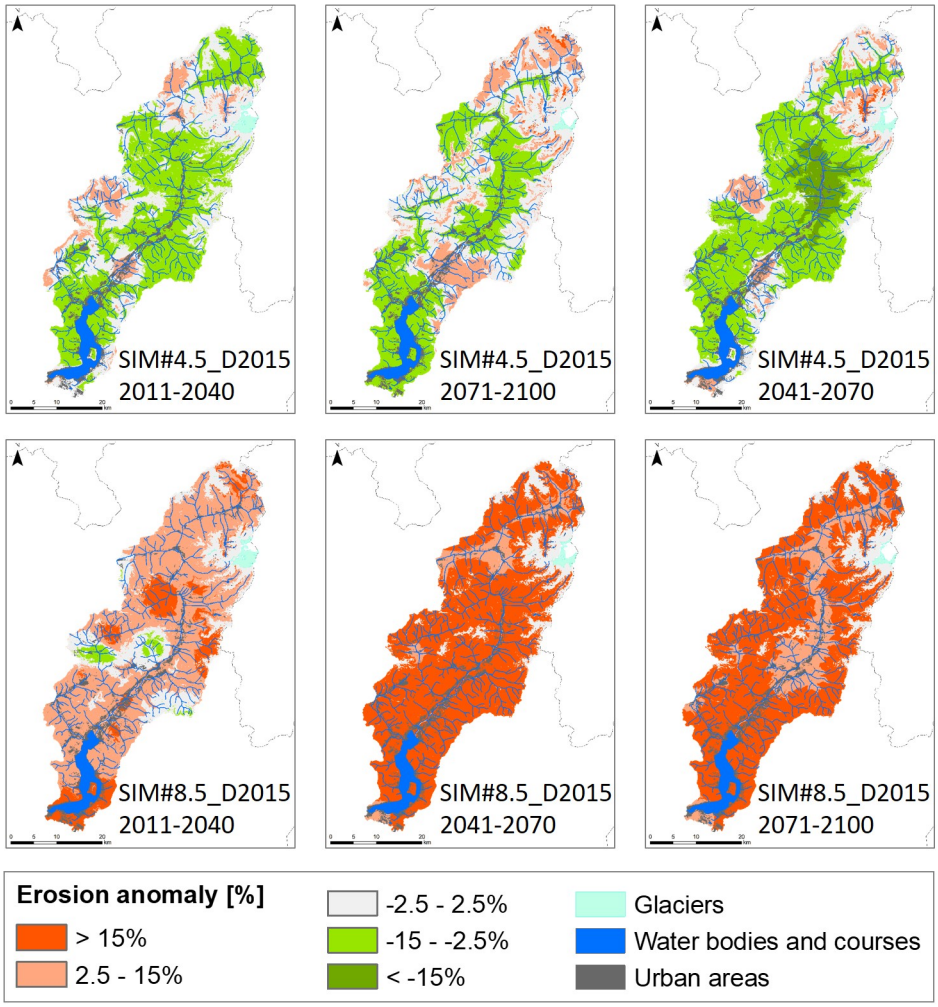

Figure 5.12: Soil erosion rate anomaly with respect to the reference period (1981–2010) for: 2011–2040 (first column), 2041–2070 (second column), and 2071–2100 (third column). SIM#4.5_D2015 (first row) and SIM#8.5_D2015 (second row).

Figure 5.13: Erosion anomaly with respect to the reference period (1981–2010) expressed as percentage of territory for SIM4.5$_D$2015$(onthetop)andSIM$8.5$_D$2015$(onthebottom)$.

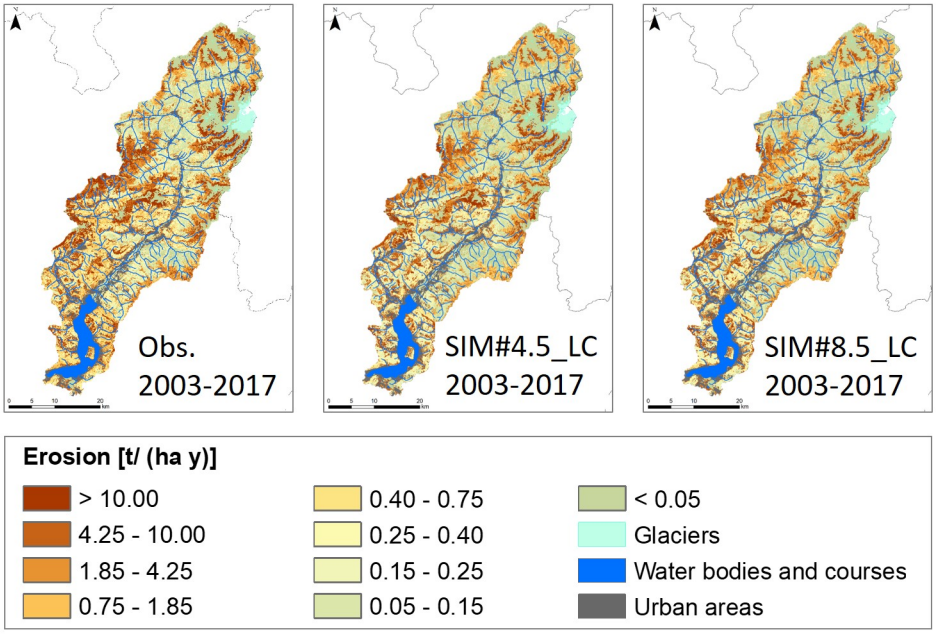

Figure 5.14: Estimates of mean annual soil erosion rates based on observations (left); and using erosion scenarios SIM#4.5_LC (center) and SIM#8.5_LC (right) with time-dependent land cover (DUSAF 2000 from 2003 to 2010 and LC 2030 from 2011 to 2017).

Figure 5.15 shows the maps of soil erosion rate anomaly for the thirty-year periods 2011–2040, 2041–2070, and 2071–2100 under the hypothesis of changes in both climate and land cover. The expected mean erosion rates are summarized in Table 5.8. The spatial patterns of future erosion anomalies (Figure 15) are similar to those presented for SIM#4.5_D2015 and SIM#8.5_D2015 (Figure 5.12), but with local variations because of the land cover changes. Overall, projections with land cover dynamics returned lower erosion rates compared to simulations with static land cover and, as expected, SIM#8.5_LC erosion rates averaged on the whole study area exceeded those of SIM#4.5_LC (by 7% for the thirty-year period 2011–2040, by 28% for the thirty-year period 2041–2070, and by 23% for the thirty-year period 2071–2100). According to SIM#4.5_LC, the mean erosion rate on the study area is expected to slightly decrease. On average, the Center region will have the highest erosion rates, while the North region will have the lowest erosion rates. Conversely, according to SIM#8.5_LC the study area is expected to slightly increase the mean erosion rate from the first (2011–2040) to the second thirty-year period (2041–2070), and then slightly decrease in the last thirty-year period (2071–2100). In this case, the highest erosion rates are in the South region, while the North region shows the lowest rates. Overall, both SIM#4.5_LC and SIM#8.5_LC project a decrease in the mean soil erosion rate and these trends seem contradicting the positive anomalies shown in Figure 5.15. Finally, Figure 5.16 summarizes the percentages of the study area where erosion is predicted to increase, decrease, or remain stable.

Table 5.7: Mean observed and simulated annual erosion rates [$t\ ha^{-1}\ yr^{-1}$] with two climate scenarios and time-dependent land cover (DUSAF 2000 from 2003 to 2010 and LC 2030 from 2011 to 2017)

	Study Area	**North Region**	**Center Region**	**South Region**
Observed (2003-2017)	3.78	3.22	4.64	3.64
SIM#4.5_LC (2003-2017)	2.82	2.15	3.35	3.07
SIM#8.5_LC (2003-2017)	2.80	1.95	3.23	3.39

Table 5.8: Mean erosion rates [t ha^{-1} yr^{-1}] according to climate and land cover projections.

Simulation Periods		**Study Area**	**North Region**	**Center Region**	**South Region**
SIM#4.5	1981-2010	3.12	2.17	3.79	3.57
	2011-2040	2.48	1.96	3.06	2.48
LC	2041-2070	2.19	1.82	2.50	2.32
	2071-2100	2.20	1.68	2.74	2.26
SIM#8.5	1981-2010	3.04	1.90	3.51	3.93
	2011-2040	2.66	1.95	3.08	3.10
LC	2041-2070	2.80	2.02	3.18	3.37
	2071-2100	2.71	1.89	3.22	3.16

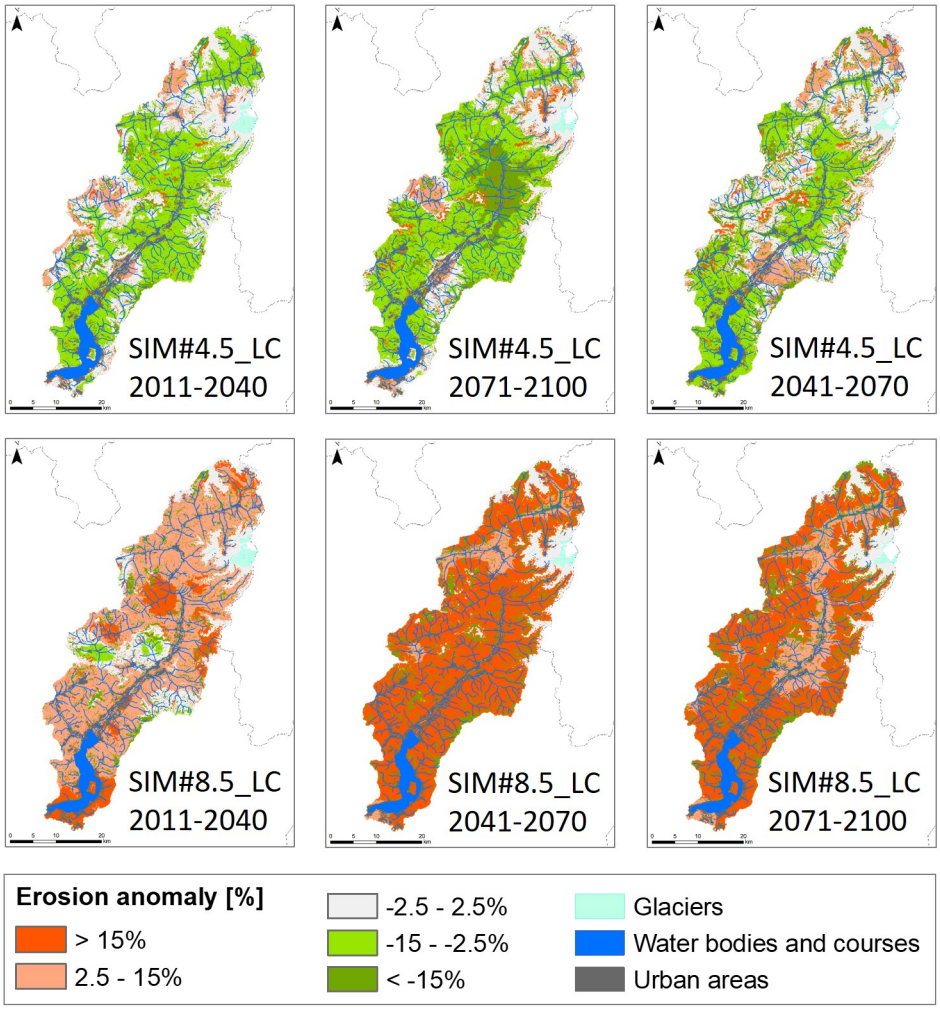

Figure 5.15: Soil erosion rate anomaly with respect to the reference period (1981–2010) for: 2011–2040 (first column), 2041–2070 (second column), and 2071–2100 (third column). SIM#4.5_LC (first row) and SIM#8.5_LC (second row).

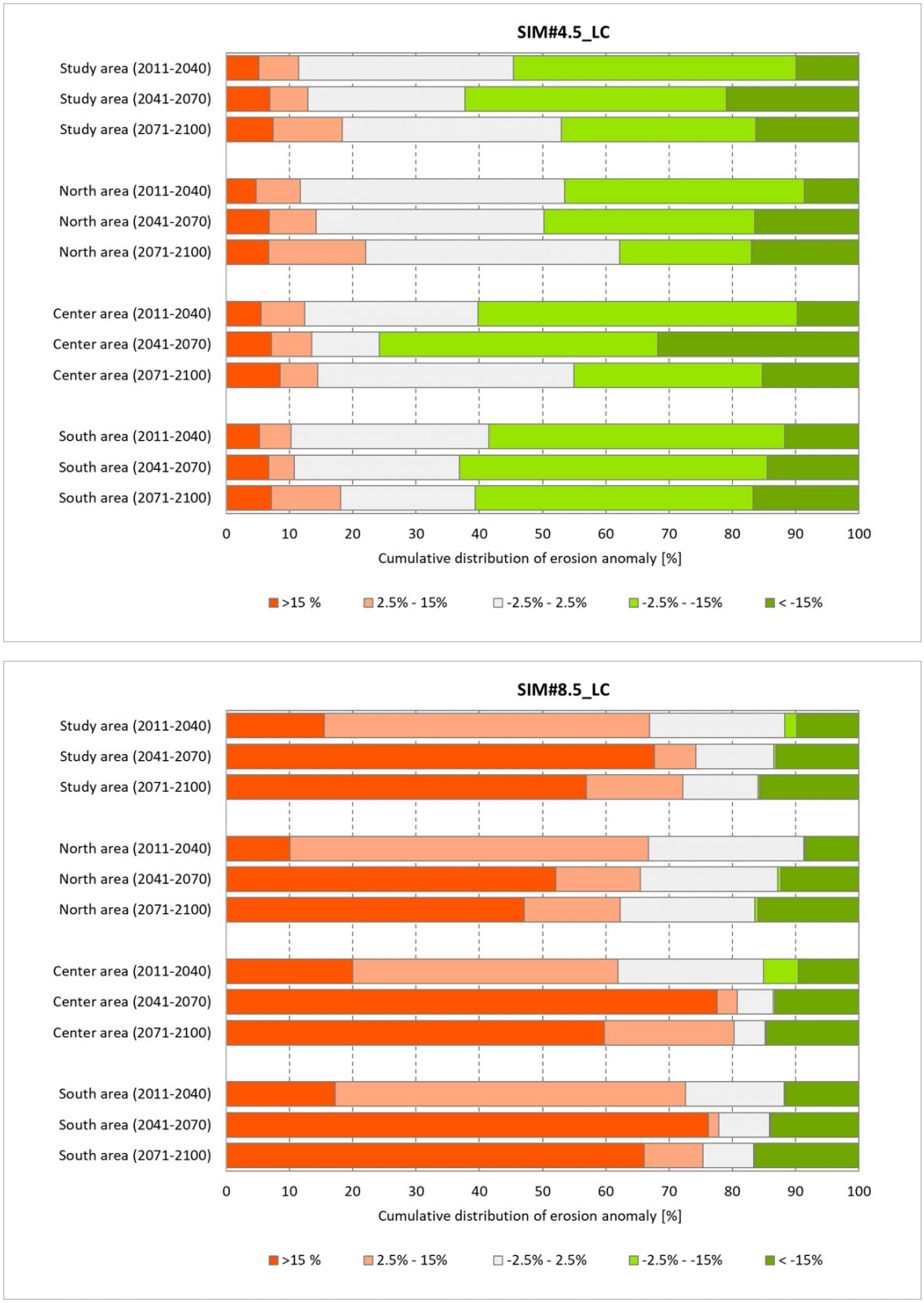

Figure 5.16: Erosion anomaly with respect to the reference period (1981–2010) expressed as percentage of territory for SIM#4.5_LC (on the top) and SIM#8.5_LC (on the bottom).

Chapter 6

Discussion

6.1 Correlation between model's parameters and soil erosion estimates

The sensitivity analysis points out that the parametrization of R-factor has the highest impact on the average potential soil erosion, when not considering the simulation SIM_05 that is biased by the C-factor overestimation. However, the pixel-based Pearson's correlation with the erosion maps shows that the R-factor is always an uncorrelated variable, regardless the parametrization used (Table 6.1). On the other hand, while the C-factor (SIM_06 vs SIM_01) has the lowest impact on soil erosion rates, however this parameter is the most correlated with the erosion maps, regardless the parametrization used (Table 6.1). Even if the different parametrization of K-factor are characterized by comparable statistics, their different spatial variability (K2 is more homogenous than K1) strongly reduces the correlation between K-factor and expected erosion rate, SIM_03 and SIM_07, using K2 formulation, show the lowest correlation coefficient with K-factor. The impact of LS-factor parametrization on the average soil erosion rates is about -56% (SIM_04 vs SIM_01), which is comparable with average reduction of LS-factor retrieved passing from LS1 to LS2, and the correlation coefficient consequently reduces from 0.29 (SIM_01) to 0.19 (SIM_04).

Table 6.1: Pearson's correlation between modelling parameters and erosion maps.

Simulation code	Parameters' code			
	R-factor	C-factor	K-factor	LS-factor
SIM_01	0.03	0.54	0.22	0.29
SIM_02	-0.08	0.53	0.19	0.29
SIM_03	0.04	0.52	0.02	0.29
SIM_04	0.04	0.69	0.27	0.19
SIM_05	0.04	0.54	0.25	0.44
SIM_06	0.02	0.59	0.23	0.29
SIM_07	0.02	0.51	0.08	0.20

6.2 Effect of seasonality on soil erosion estimates

Precipitation regime (i.e. R-factor) and land cover variability (i.e. C-factor) are the parameters that convey seasonality in D-RUSLE. Simulations SIM_02, SIM_05 and SIM_06 show this effect (Table 6.2). SIM_02 retrieves lower soil erosion rates, as a consequence of introducing snow dynamics and the protective effect of snow cover. SIM_05 and SIM_06 introduce a dynamic estimate of C-factor, which translates into a smaller sheltering effect of vegetation during Autumn/Winter. This increases Autumn/Winter erosion estimates, leading to higher erosion rates in Autumn/Winter with respect to Spring/Summer. It is to be noted that traditional RUSLE does not model this dynamic and the modelled Autumn/Winter erosion rates are smaller than Spring/Summer erosion estimates (SIM_01). However, that is not consistent with the phenology of vegetation cover. The out-of-range Autumn/Winter erosion values of SIM_05 are due to the underestimated protective effect of vegetation (C1 parametrization), particularly for forest areas, which leads to a overestimation of soil erosion rates (see Section 4.2).

Simulation code	Val Camonica		High Elevation Areas		Medium Elevation Areas		Iseo Lake Areas	
	S/S	A/W	S/S	A/W	S/S	A/W	S/S	A/W
SIM_01	19.54	12.58	32.19	20.31	18.58	12.53	6.31	3.96
SIM_02	6.91	3.24	9.32	3.89	7.64	3.79	3.47	1.96
SIM_05	17.35	66.95	27.59	91.22	14.20	75.74	8.96	31.04
SIM_06	15.95	20.15	28.53	32.37	13.45	21.25	4.30	5.37

Table 6.2: Average Spring/Summer (S/S) and Autumn/Winter (A/W) erosion estimates [$t\ ha^{-1}\ yr^{-1}$].

Figure 6.1 shows the comparison of the R-factor time series for Spring/Summer and Autumn/Winter. The seasonal effect is much more clearly highlighted by the R2 parametrization, as it splits snowfall and rainfall and considers the soil sheltered by snow cover. Thus, Spring/Summer erosive force exceeds Autumn/Winter erosive force because Spring/Summer rainfall is more abundant and almost no snow cover is present. The effect of seasonality when using the R2 parametrization (SIM_02) is to decrease potential soil erosion rates of almost 3 times during Spring/Summer and 4 times during Autumn/Winter, compared to the classic parametrization (SIM_01) (Table 6.2 and Figure 6.2). This reduction is much more evident in the high altitude areas and decreases moving to the lake area, where lower erosion rates are due effect discussed below. Figure 6.3 shows the comparison of the C-factor time series for Spring/Summer and Autumn/Winter. The reduced vegetation abundance in Autumn/Winter produces higher values for both C1 and C2 parametrizations, while this is not accounted by the "static" C0 parametrization. Slightly higher cover management factor values are retrieved in the high altitude areas, due to the presence of sparsely vegetated areas and moors. On the other hand, the Iseo Lake area has an opposite behaviour because of a larger vegetation cover protecting the soil from erosion. As already mentioned in Section 4.2, C-factor is overestimated when using unbounded relationships with NDVI (C1). Consequently, estimates of potential soil erosion rates reflect the seasonality effect conveyed by land cover. However, in simulation SIM_01 only the effect of precipitation seasonality is present, as the C0 cover management factor parametrization is constant over time. In simulations SIM_05 and SIM_06, the seasonality effect comes from both land cover changes and rainfall/snow seasonality. Spring/Summer erosion estimates with the parametrization of SIM_06 are slightly lower with respect to those simulated with the parametrization of SIM_05, as a consequence of the bounding on C values. In contrast, during Autumn/Winter, erosion rates of SIM_05 are overestimated because of low NDVI values causing overestimates of C-factor, that outreach the SIM_05 estimates of almost four times (Table 6.2). The use of multi-temporal satellite time series for the computation of C-factor (SIM_06 simulation) produces a slight increase in Autumn/Winter erosion estimates and a slight decrease in Spring/Summer erosion estimates (Figure 6.4). Besides, the estimates of soil loss rates decrease from high altitude to the lake area, meaning that during Autumn/Winter land cover types have a higher influence on erosion modelling compared to rainfall. Overall, the computation of

the model's parameters for the Autumn/Winter season seems the most critical for soil erosion in the Italian Alps.

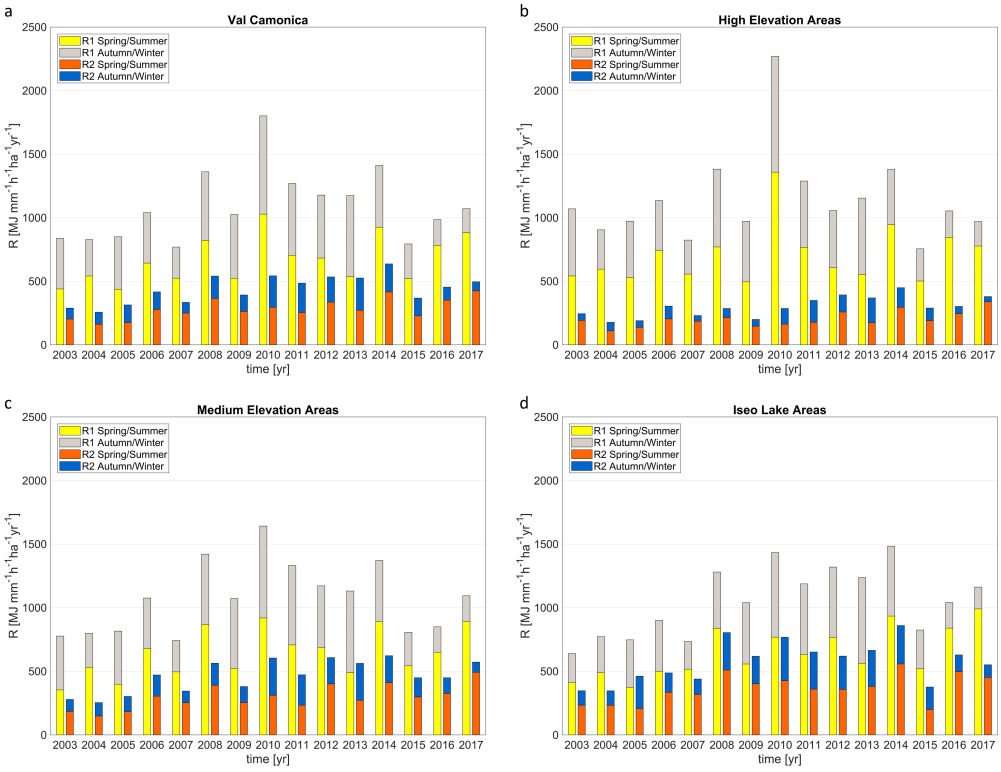

Figure 6.1: Time series of R-factor (2003-2017) computed for Spring/Summer and Autumn/Winter with the R1 (SIM_01) and R2 (SIM_02) parametrizations.

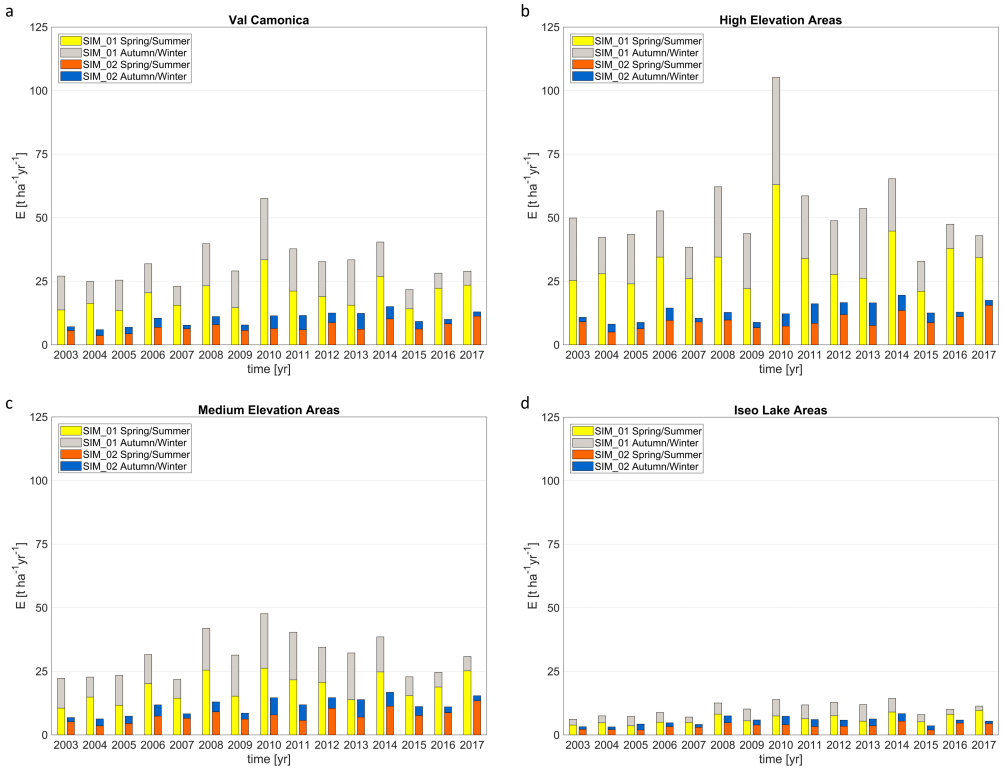

Figure 6.2: Comparison of potential soil erosion rates (2003-2017) computed for Spring/Summer and Autumn/Winter with the R1 (SIM_01) and R2 (SIM_02) parametrizations.

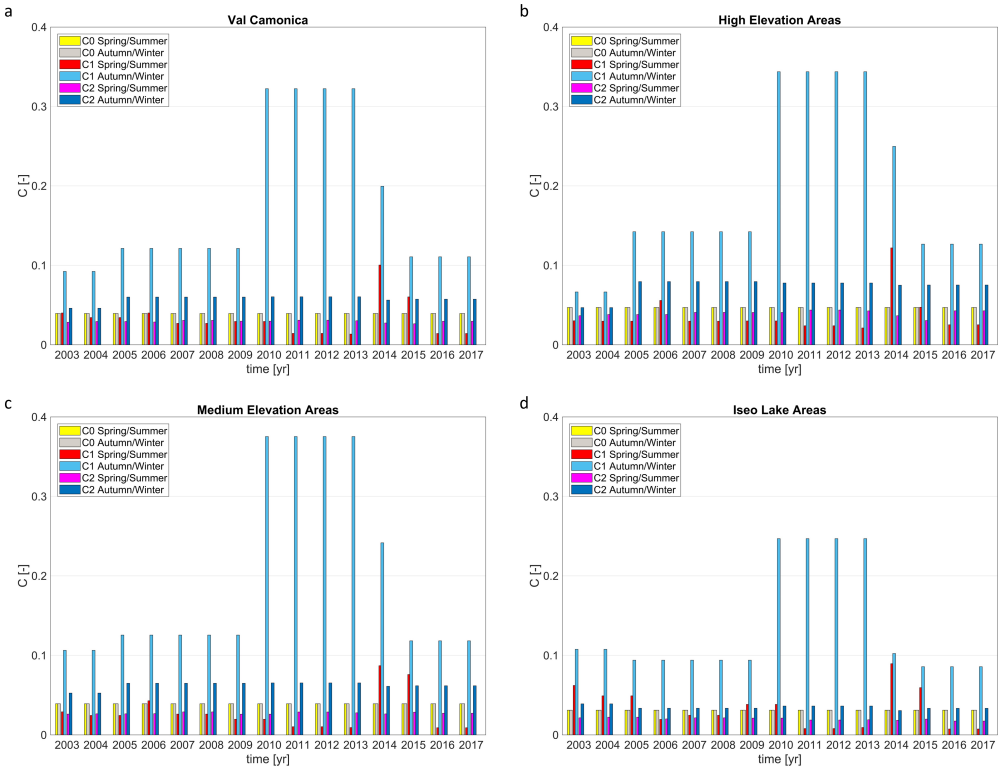

Figure 6.3: Time series of C-factor (2003-2017) computed for Spring/Summer and Autumn/Winter with the C0 (SIM_01), C1 (SIM_05) and C2 (SIM_06) parametrizations.

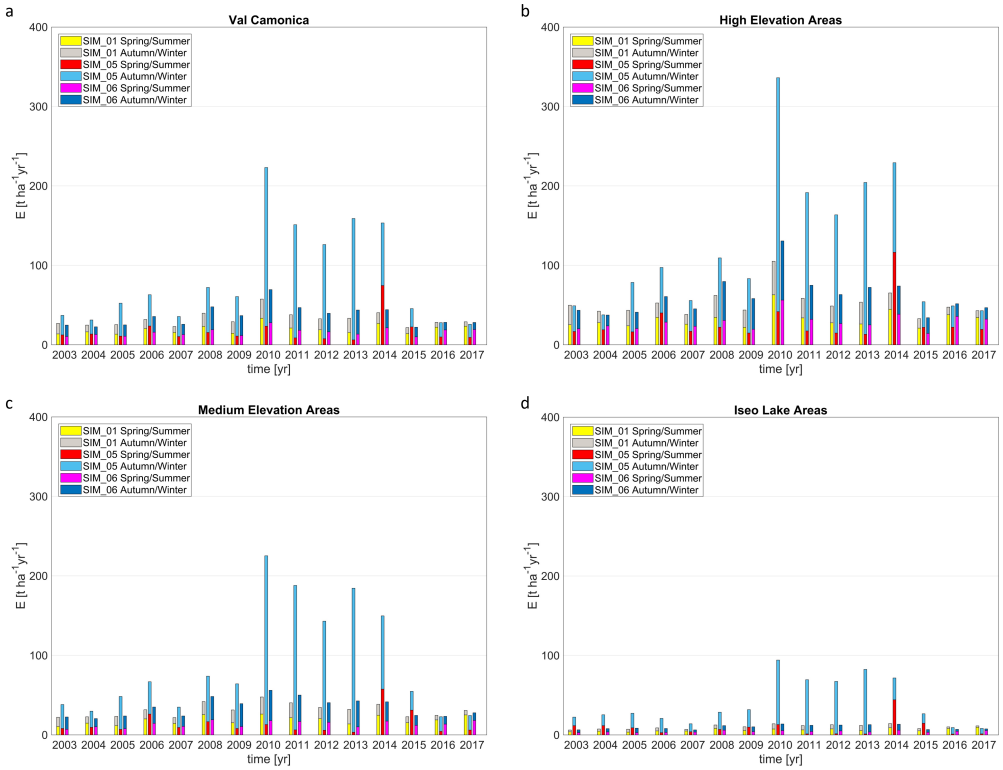

Figure 6.4: Comparison of potential soil erosion rates (2003-2017) computed for Spring/Summer and Autumn/Winter with the C0 (SIM_01), C1 (SIM_05) and C2 (SIM_06) parametrizations.

6.3 Climate scenarios

Taking into account the different spatial domain and the different models used for climate change projections, our simulated mean increase in rainfall erosivity (+24% by 2040) is in line with the overall estimate for Europe (+18% by 2050) made by the European Commission (78). Nevertheless, land cover transformations could modulate (mitigating or enhancing) some erosional trends. Thus, the counterbalancing effects of both precipitation and land cover dynamics will be considered when predicting future trends to avoid inaccurate predictions at local scale. Our results clearly show that both climate and land cover changes contribute to modifying future soil erosion rates. On the one hand, for static land cover, when simulating the climate change with the worst-case SIM#8.5_D2015 scenario we see a growth of the areas with increasing soil erosion and a gradual regress of the areas with decreasing soil erosion. On the other hand, when comparing the same climate scenario with and without the land cover evolution (i.e., SIM#4.5_D2015 vs. SIM#4.5_LC or SIM#8.5_D2015 vs. SIM#8.5_LC), we see a decrease in the mean soil erosion rate over the whole study area because of an enhanced sheltering effect by vegetation and the retreat of glaciers, which compensates for the increase of rainfall erosivity. Nevertheless, the spatial extent with enhanced erosion anomalies with higher (positive and negative) erosion

anomalies expand. Results show that a critical point is the capability of the climate scenarios to correctly simulate the occurrence and the intensity of the precipitation events: biases in the precipitation intensity cause a general underestimation of the R-factor in the reference period, even if the annual mean precipitation is well reproduced. Therefore, the variability of climate projections results in the absence of a clear direction of change of erosion rates that seems more influenced by the temperature increase rather than by precipitation trends. Specifically, the expected temperature increase will cause an increase in rainfall erosivity because snowfall is expected to diminish and rainfall is expected to increase, even if the annual precipitation (i.e., rainfall+snowfall) does not change significantly.

6.4 Projections of Precipitations

Considering the first thirty-year period (2011–2040), the SIM4.5 climate scenario predicts that precipitations will slightly increase (between +2.5% and +15%) in 17% of the study area and will slightly decrease (between -15% and -2.5%) in the 3% of the of the study area. More in detail, this scenario returns that:

- North: 5.5% of this territory will have a slight increase, 9.0% will have a slight decrease and the rest will have almost constant precipitation;
- Center: 19% of this territory will have a slight increase and the rest will have almost constant precipitation;
- South: 25% of this territory will have a slight increase and the rest will have almost constant precipitation.

Over the same period, the SIM8.5 climate scenario predicts a slight increase for 99% of the study area and a moderate increase for the remaining 1%, mostly located in the Center (overall about 2.4% of Center region). Considering the second thirty-year period (2041–2070), SIM4.5 predicts that precipitation is expected to slightly decrease in 97% of the study area, and all the three regions show the same trend. On the other hand, SIM8.5 predicts a different signal over the same period; about half of the study area (48%) will have a slight increase, and about half of the study area (52%) will have a moderate increase. More in details, the slight increase of precipitation is expected in 88% of the North region, 34% of the Center region, and 15% of South region, while the moderate increase will affect 12% of the North region, 66% of the Center region, and 85% of South region. Considering the last thirty-year period (2071–2100), SIM4.5 predicts that the majority of the study area (91%) will have almost constant precipitation and only 9% a slight decrease. In this case, the precipitation reduction is foreseen in 15% of the North region, 8.4% of Center region, and 2.4% of South region. Over the same period, SIM8.5 projects a slight increase in precipitation for the whole study area.

6.5 Projections of Temperatures

According to SIM#4.5 (Figure 5.5), the mean annual temperature is expected to change almost homogenously on the whole study area. The mean projected changes of temperature are +0.79 °C for 2011–2040, +1.48 °C for 2041–2070, and +1.42 °C for 2071–2100. In the period 2071-2100, our simulation shows a temperature anomaly decreasing from the South region (+1.44 °C) to the North region (+1.40 °C), while the valley floor that crosses the study area from North-West to South-East displays a higher temperature anomaly compared to its surroundings. The SIM8.5 climate scenario depicts a different picture: The mean projected changes of temperature are +0.62 °C for 2011–2040, +2.02 °C for 2041–2070, and +4.06 °C for 2071–2100. In the period 2071–2100, our simulations show a temperature anomaly decreasing from the North (+4.13 °C) to the Center (+4.05 °C) to the South (+3.99 °C). In this scenario, the northeastern of the North region, the western part of the Center region and the valley floor have the lowest temperature anomalies.

6.6 Simulation of Rainfall Erosivity

The spatial distribution of the simulated R-factors for 2003–2017 are similar to those estimated from observations in the same period (Figure 5.6). However, as already pointed out, both simulations underestimate the rainfall erosivity by about 26%. A more detailed analysis revealed that the climate scenarios returned different results at local scale (Table 6.2):

- North: the bias is +5% for SIM#4.5 and -33% for SIM#8.5;
- Center: the bias is -29% for both SIM#4.5 and SIM#8.5;
- South: the bias is -23% for SIM#4.5 and -17% for SIM#8.5.

Overall, the underestimation of the rainfall erosivity might be related to differences in the sequence and intensity of the observed and simulated precipitation events, which are further emphasized by the quadratic relationship between hourly rainfall intensity and R-factor (equation (2)). The stochastic generator used to downscale the simulated precipitation, by its nature, reproduces second-order statistics (i.e., mean and variance) of the observed dry/wet spell sequence and of mean daily precipitation. However, it does not replicate path-wise the observed precipitation patterns. This is consistent with the aim of projecting future precipitation patterns by downscaling IPCC projections, which are statistically consistent with the current, yet including modified climate change effects as projected. According to SIM#4.5 the mean R-factor of the study area is expected to be almost constant (Figure 5.6), with simulated values of 312 [MJ mm ha^{-1} h^{-1} yr^{-1}] in 2011–2040, 302 [MJ mm ha^{-1} h^{-1} yr^{-1}] in 2041–2070, and 316 [MJ mm ha^{-1} h^{-1} yr^{-1}] in 2071–2100. SIM#8.5 envisage a different scenario: the mean R-factor is expected to reach its maximum by 2041–2070 (400 [MJ mm ha^{-1} h^{-1} yr^{-1}).

6.7 Projections of Future Land Cover and Cover Management Factor

The apparent disagreement between the trends predicted by SIM#4.5_LC and SIM#8.5_LC (Figure 5.14), which project a decrease of the mean soil erosion rates, and the positive erosion anomalies (Figure 5.16) is due to the small areas with large changes in C-factor estimates. In fact, the land cover evolution from DUSAF 2000 to LC 2090 projects that about 16% of the whole study area will see a reduction of C-factor. More than 55% of the land classified as "sparsely vegetated areas," "pastures," and "non-irrigated arable land" in DUSAF 2000 are modelled to evolve into land cover classes with lower C-factor. Thus, even local changes in land cover might have a big influence on the mean erosion rates of the whole study area. Specifically:

- "Sparsely vegetated areas" cover 8.7% of the study area in 2000 (it is the third more frequent land cover) but are projected to reduce to 4.6% in 2090;
- "Pastures" cover 10.9% of the study area in 2000 (it is the fifth more frequent land cover) but are projected to reduce to 4.9% in 2090;
- "Non-irrigated arable land" covers 1.1% of the study area in 2000 but is projected to reduce to 0.7% in 2090.

Result strongly depends on the reliability of the land cover simulation process but, unfortunately, there are few chances to assess its real accuracy. An exception is the simulated land cover map for the thirty-year period 2011–2040 (LC 2030) because the neural networks was trained using the observed land cover (DUSAF) for both the periods (2000 and 2015). The weighted skill score (Equation 6.1) used to evaluate the projected land cover map is similar to the Cohen's kappa statistic, where the expected accuracy by chance is estimated as the same chance of happening (Equation 6.2):

$$S_i = \sum_{j=1}^{n} p_{ij} \frac{A_{ij} - E(A_{ij})}{1 - E(A_{ij})}, \tag{6.1}$$

$$E(A_{ij}) = \frac{1}{T_i + P_i} \tag{6.2}$$

where:

- S_i is the skill score for the sub-model i;
- A_{ij} is the measured accuracy of the transition/persistence for class j for the sub-model i;
- $E(A_{ij})$ is the expected accuracy of the transition/persistence for class j for the sub-model i;
- p_{ij} is the percentage of land cover class j for the sub-model i;

- T_i is the number of transitions in the sub-model i;
- P_i is the number of persistence classes in the sub-model i.

Overall, the weighted skill score shows a moderate agreement for the sub-models #1 (S=0.43) and #3 (S=0.30), but no agreement for the sub-model #2 (S=0.03). That could be due to the very short span of time considered for training the models (only 15 years), which seems not enough for defining the reliable trends in land cover changes. Nevertheless, that was the best option for our study area.

6.8 Estimates of Future Soil Erosion

With respect to static land cover simulations, SIM#4.5_D2015 foresees an erosion scenario with limited variability on the whole area: about 90% of the study area will have no changes or a slightly decrease in erosion rates. Only a small portion of the study area (7.7% in 2011–2040, 8.0% in 2041– 2070, and 15.5% in 2071–2100) will see a slight increase in the erosion rates, mostly in the South and North regions. On the other hand, SIM#8.5_D2015 foresees a different scenario: most of the study area (72.7% in 2011–2040, 77.1% in 2041–2070, 85.1% in 2071–2100) will increase its erosion rates and the rest is expected to remain stable. This erosion scenario does not predict any decrease of erosion rates. When combining climate with the land cover projections, SIM#4.5_LC foresees a similar scenario to SIM#4.5_D2015. However, in this case a smaller part of the study area is predicted to have no changes or a slight decrease in erosion rate (78.6% in 2011–2040, 66.1% in 2041–2070, and 65.3% in 2071–2100), and a larger part of the study area will see an increase in erosion rates (11.5% in 2011– 2040, 13.0% in 2041–2070, and 18.4% in 2071–2100). In the rest of the study area, the soil erosion is expected to decrease moderately. As for SIM#4.5_DUSAF2015, the regions more exposed to soil erosion increase are the South and North. Alike SIM#8.5_D2015, when considering land cover dynamics SIM#8.5_LC foresees an erosion scenario where most of the territory is supposed to increase its erosion rates. However, contrary to the static land cover simulation, SIM#8.5_LC highlights some local areas where soil erosion moderately decreases due to land cover changes.

6.9 Comparison to Similar Studies

Although a common belief is that increased rainfall amounts and intensities will lead to greater erosion rates, it is rather difficult comparing our findings with existing literature. The reason is that different studies have substantial differences in:

- Working scale. The majority of papers performs global, national, or regional analysis, and not local-scale analysis;
- Topographic and land cover characteristics of the study areas;

- Model used to estimate soil erosion;
- Model used to project climate and land cover changes.

Even with these limitations, our study complements the existing literature on the synergic effects of climate and land cover change on soil erosion. In their review about studies of potential effect of climate change on soil erosion rates at a national scale (USA), Nearing et al. (38) reported that, unless amelioration measures were taken, erosion will increase (with significant geographic heterogeneity) mainly as function of an increase in rainfall amounts and intensities, rather than the number of days of precipitation in a year. In this review, erosion and runoff rates were mainly computed with the Water Erosion Prediction Project (WEPP) model (22) and changes in rainfall erosivity were determined according to estimations of future climate change provided by two GCMs through statistical relationships. Moreover, where rainfall amounts were projected to increase, erosion and runoff were expected to increase at an even greater rate (the ratio of erosion increase to annual rainfall increase is approximately 1.7). Although not predicting land cover changes, the authors declared that even in cases where annual rainfall would decrease, systems feedbacks related to decreased biomass production could lead to greater susceptibility of the soil to erosion. A more detailed study by (41), evaluated the potential impacts of precipitation changes on soil erosion and surface runoff in southeastern Arizona. The authors used seven GCMs models, three emission scenarios for the 2050s and 2090s and the Rangeland Hydrology and Erosion Model (RHEM) described in (39). The seven models used show a similar variability in the annual precipitation for all the three scenarios, ranging from -17.9 to +13.7%. However, a decreased biomass production could lead to long-term increase in soil erosion due to sparser vegetation cover (38). In this case, the authors expected an increment of soil erosion between +44.7 and +210.4%, depending on the models and scenarios considered. The authors also claimed that future increase in runoff and soil erosion could accelerate the transition of grassland to shrubland, or to more eroded states, due to the positive vegetation-erosion feedback. Other authors (42);(43);(79);(44) evaluated the long-term impact of climate change on sediment yield and soil erosion for the Mediterranean region, projecting future climate to 2100. These studies demonstrated that estimated erosion variations can be closely related to changes in precipitation and temperatures, although a biomass growth could be significant in determining the climate change impacts on erosion. However, there is a wide spatial variability in the trends for soil erosion depending on rainfall changes and biomass growth and relevant uncertainty still characterize these types of works. The analysis of the combined effect of both climate and land cover changes is more common at a local scale. Asselman et al. (45) studied the potential effects of changes in both climate and land use on sediment transport from the upstream basin to the lower Rhine delta. In this case, the authors considered three climate change scenarios based on the UK Hadley Centre's high-resolution atmospheric general circulation model [53], corresponding to a temperature rise at 2100 of +1 °C, +2 °C, and +4 °C. Considering the intermediate climate change scenarios, the authors estimated across the entire Rhine basin a temperature rise from +3.2 °C to +3.9 °C in summer and from +4.3 °C to +4.5

°C in winter. While precipitation changes were projected from -9.8% to 10.9% in summer and from +16.6% to +32.7% in winter. In addition, they considered two land use change scenarios that forecast a decrease in crop production because of population growth, and a considerable reduction of the agricultural land because of temperature and CO2 concentration increase. Soil erosion was estimated with the Rhine model for evaluating the effects of Environmental Change On Delivery of Eroded soil to Streams (RECODES) described in (80), which is based on the Universal Soil Loss Equation (USLE) model (14). Their findings showed that, for the projected climate and land use changes, erosion rates were expected to increase in the Alps and to decrease in the German part of the basin, with a mean increase of +12% for the Rhine basin. (40) analyzed the impact of climate and land use changes on streamflow (water quantity) and erosion in humid (Sao Lourenco) and dry (Guadalupe) Mediterranean catchments in Portugal. They used the SWAT hydrological model [56], which computes soil erosion through the Modified Universal Soil Loss Equation (MUSLE) model (81). Climate change scenarios were developed for the period 2071–2100 using the ECHAM5 GCM [57] driven by two emission scenarios (A1B and B1) projecting a decrease in annual rainfall for both catchments (humid: -12%; dry: -8%), but a significant increase of rainfall in winter (+19% for Sao Lourenco and +40% for Guadalupe). Land use scenarios were defined from a linear downscaling of European trends for generic land use types in Portugal, improved by local trends estimated from a comparison with past land cover to identify possible land-cover type replacements. In their study, the authors also analyzed socio-economic trends to gain insight into the driving forces behind land use changes. They defined two scenarios, which both predicted a decrease in agricultural lands for food production. Their results showed that both climate and land cover changes strongly influence soil erosion and sediment transport in both the basins studied. However, they got contrasting results in estimations of sediment transport for the humid (A1B: -29%; B1: -22%) and dry (A1B: +222%; B1: +5%) catchments. (82) published an application of the SWAT model in the Spanish area of the Ompólveda River catchment. They considered eight scenarios obtained by combining climate and land use projections. According to their findings, the increase of scrublands and forests were expected to reduce future soil erosion, while the increase of croplands could make the soil more prone to erosion. Finally, the work by (46) investigated the future changes in erosion rates for three catchments in West, North, and East Saxony/Germany under climate and land use/soil management changes. The climate projection showed a slight increase of precipitation, with a decrease in the number of events with low intensities (0.1 – 0.2 [mm min-1]) and medium intensities (0.2 – 0.5 [mm min-1]). On the other hand, the number of rainstorms with high and very high intensities (> 1 [mm min-1]) was expected to increase. The authors concluded that, without proper soil management and land use policies, climate change will lead to an increase of soil loss by 2050 and a partial decrease from 2050 to 2100. Moreover, the authors also pointed out that changes in soil management such as “no tillage” or land use changes from agriculture to pasture/forest could reduce the soil erosion of more than 90%, thus with a much higher impact than that of climate change alone. This means that, according to (46), land cover and use changes and soil management practices are expected to have higher impacts on soil erosion than

precipitation patterns. The analysis of existing literature has evidence that both climate change and land cover changes will have an impact on future soil erosion. Nevertheless, all past works highlight that projected soil erosion patterns could be very heterogeneous in the areas studied. Our research is substantially in line with these outcomes, confirming an overall increase of soil erosion in the Alps due to climate change, modulated by land cover changes which can generate local patterns of decreasing erosion. That makes very challenging the definition of a general trends.

6.10 Current Limitations

D-RUSLE is an empirical method for modelling potential erosion caused by the impact of raindrops. Thus, from the modelling point of view, erosion is mainly controlled by precipitation, land cover, topography, soil properties, and soil conservation practices. This means that, similar to any other erosion model derived from RUSLE, also D-RUSLE does not consider the melting of permafrost. While the effects of permafrost should be very limited in the study area, in other sites, latitudes or elevations, permafrost could play a very important role in controlling soil erosion. As a matter of principle, D-RUSLE could be modified for including a new parameter related to permafrost (the permafrost factor, PF-factor), but specific experimental activities and maps of the extension and dynamics of permafrost would be needed. That is beyond the scope of our research. We are also aware that snow-induced erosion might be relevant in some mountain areas and RUSLE-like models cannot describe this effect (83). In D-RUSLE, the computation of R-factor includes the snow cover sheltering effect, thus simulating the snow accumulation and melting process, but our model neglects the erosion because of snow melting. Theoretically, snow melting could be included in the computation of the rainfall erosivity factor by considering the snow-water equivalent data (this is a different process from the raindrop action on soil simulated by RUSLE-like models). However, it might be complex to get a satisfactory conversion of snowfall into equivalent liquid precipitation because the snow cover usually has a significant spatial and temporal heterogeneity (84) and the snow melting processes might show oscillations over time. With respect to C-factor, currently unvegetated soils are given a null value, thus a null erosion regardless the rainfall intensity. This is a heritage of RUSLE-like modelling that seems reasonable for compact rocks but could be not true for the moraines exposed to the retreat of glaciers. Consequently, this parametrization is conservative and underestimates the soil erosion at higher elevations. Finally, our study did not include land management policies as constraints for simulating future land cover transformations. Future refinements could might also consider this aspect.

Chapter 7

Conclusions

7.1 D-RUSLE

Recently, many environmental protection agencies have recognized soil degradation due to erosion processes as a serious threat and the European Commission addresses soil degradation as a key priority within its Soil Thematic Strategy. Therefore, soil erosion models are extremely useful for quantifying the impact of soil loss at the basin scale, assessing the potential effects of climate-driven land cover changes on soil erosion rates, defining priorities for effective and sustainable land management actions (i.e. re-vegetation of sparsely vegetated areas with high soil loss rates). In this work, we proposed a RUSLE-like dynamic model (D-RUSLE) to estimate potential soil erosion rates and we tested its performances in the fragile ecosystem of the Italian Alps, where climate change, together with both natural and anthropogenic land transformations, contribute to soil degradation. Our model is able to catch variations in potential soil erosion due to different landscape characteristics: higher rates were found within the land cover classes which are more affected by seasonality (e.g. broad-leaved forests), alike higher altitude areas which were more prone to erosion due to sparse or absent vegetation coverage, while forested areas at lower altitudes were found less exposed to erosion. Moreover, D-RUSLE showed that integrating satellite-derived information in the estimation of C-factor helps in providing a more detailed and reliable estimate of potential soil loss, both including seasonal and long-term land cover changes. In particular, the use of satellite images may increase the spatial resolution of C-factor improving the estimates of soil erosion at regional/local scale, in particular in areas where vegetation is the predominant land cover. Besides, Spring/Summer and Autumn/Winter contribution to soil erosion can be evaluated separately and focused actions towards soil erosion could be programmed.

7.2 Climate Projection

Global warming, and its consequences on glacier retreat and frequency of extreme events, is now undeniable (85). Climate change and land cover transformations have gained increasing

attention because of their impacts on the environment. In particular, they are considered to be the main causes of accelerated land degradation and, specifically, of soil erosion. Therefore, maintaining soil quality for achieving food security, acting to mitigate climate change, and restraining land degradation have been considered among the recently approved United Nations Sustainable Development Goals (86). This is the first study investigating the future scenarios of soil erosion under both climate and land cover changes in Val Camonica and Lake Iseo, one of the largest valleys of the central Alps. Specifically, we investigated nine climate scenarios until 2100 and then analyzed in detail the impacts of soil erosion on two of them: GCM CCSM4 driven by RCP4.5 and the GCM EC-Earth driven by RCP8.5. The first climate scenario forecast a best-case (and optimistic) temperature increase of +1.4 °C and small changes in annual precipitation (-1.8%) by 2100. The latter scenario forecast a worstcase temperature increase of +4.0 °C and also larger changes in annual precipitation (+8.4%). Future land covers were simulated using automatic machine learning based on past observed land changes. Our outcomes confirm past findings: both climate change and land cover changes will have an impact on soil erosion. Nevertheless, it is impossible to describe a trend consistent throughout the study region or for the entirety of Europe's Alps because the projected soil erosion patterns are contextual and heterogenous. Depending on the simulation scenario, if the mean annual precipitation does not change significantly and temperature increases no more than 1.5-2.0 °C, then about half of the study area will experience a decrease in its mean annual erosion rate and less than 20% will see an erosion increase. At the other extreme, if the mean annual precipitation increases more than 8% and the temperature increases more than 4.0 °C, then about three-quarters of the study area will see increase in annual erosion. What clearly emerges from the study is that areas with higher (positive and negative) erosion anomalies are expected to expand, and their patterns will be modulated by future land transformations. With a doubts, land cover prediction could be improved but it is important to consider this parameter in future scenarios. When working with future climate scenarios, we have no real way to validate such models because they provide precipitation projections that are consistent with observed precipitation amounts, but do not truly replicate climate. Thus, we cannot determine whether most of the uncertainties stem from land cover projections or from the climate scenarios used.

7.3 Parameter computation with lower data availability

It is possible to affirm that the model is scalable on a different study area, with different data availability. The integration of machine learning algorithms and statistical data proved to be a useful tool to optimize the model parameters in such situations. The future development of this work is to conclude the processing of the D-RUSLE parameters, in order to evaluate the future evolution of soil erosion, under the influence of climate changes.

References

[1] Aiello M. Vezzoli R. Rota Nodari F. Polinelli F. Frassy F. Rulli M.C. Ravazzani G. Bocchiola D. Soncini A. Chiarelli D.D. Passera C. Corbari C. (2018 September). Satellite-based cover management factor assessment for soil water erosion in the Alps. Proceedings of the Remote Sensing for Agriculture Ecosystems Gianinetto, M., p. 107830T). International Society for Optics Hydrology XX (Vol. 10783, and Photonics.

[2] Borrelli P. Poesen J. Ballabio C. Lugato E. Meusburger K. Montanarella L. Alewell C. (2015). The new assessment of soil loss by water erosion in Europe. Environmental science policy 54 438-447. Panagos, P.

[3] Borrelli P. Meusburger K. Alewell C. Lugato E. Montanarella L. (2015). Estimating the soil erosion cover-management factor at the European scale. Land use policy 48 38-50. Panagos, P.

[4] E.; Montanarella L.; Panagos P. Soil erosion in the Alpine area: Risk assessment Bosco, C.; Rusco and 117–123. climate change. Studi Trentini di Scienze Naturali 2009, 85.

[5] Priori S. Costantini E. A. C. (2015). Soil erosion risk Sicilian Region (1: 250 000 scale). Journal of Maps 11(2) 323-341. Fantappiè, M.

[6] THE EUROPEAN ECONOMIC COM(2006)231 final COMMUNICATION FROM THE COMMISSION TO THE COUNCIL, THE EUROPEAN PARLIAMENT, SOCIAL COMMITTEE, and THE COMMITTEE OF THE REGIONS Thematic Strategy for Soil Protection (2006).

[7] Jones R. J. Rickson R. J. Smith C. J. (2009). Tolerable versus actual soil erosion rates in Europe. Earth-Science Reviews 94(1-4) 23-38. Verheijen, F. G.

[8] Letcher R. A. Jakeman A. J. (2003). A review of erosion Merritt, W. S. and 761-799. sediment transport models. Environmental Modelling Software, 18(8-9).

[9] J. Soil Erosion in Europe; John Wiley Boardman, J.; Poesen and 2007 Sons: Chichester, UK.

[10] Sediments Chapman, D.V. Water Quality Assessments: A Guide to the Use of Biota and Abingdon-on-Thames Oxfordshire UK 2006. Water in Environmental Monitoring, 2nd ed.; Taylor Francis: Milton Park.

[11] E.Y.; Lorenson T.D.; Tran K.; Alexander C. Temporal Bay, S.M.; Zeng and 56 255–276 spatial distributions of contaminants in sediments of Santa Monica Bay, California. Mar. Environ. Res. 2003.

[12] J. Does control of soil erosion inhibit aquatic eutrophication? J. Environ. Manag. 2012 93 140–146. Ekholm, P.; Lehtoranta.

[13] M.A.; Schoellhamer D.H.; Shellenbarger G.G.; Weidich K.W. Continuous Water-Quality Buchanan, P.A.; Downing-Kunz and pp. 2014–3090 Suspended-Sediment Transport Monitoring in the San Francisco Bay; U.S. Geological Survey Fact Sheet: Reston VA USA, 2014; Volume 4.

[14] Smith D. D. (1978). Predicting rainfall erosion losses-a guide to conservation planning. Predicting rainfall erosion losses-a guide to conservation planning. USDA Agricultural Handbook No. 537 58 pp. Wischmeier, W. H.

[15] J. R. (1975). Sediment yield prediction with Universal Equation Using Runoff Energy Factor. Present Williams, Prospective Technology for predicting sediment yields, and pp.244-252. sources. ARS-S-40, US Department of Agriculture Agricultural Research Service.

[16] Foster G. R. Weesies G. A. McCool D. K.- Yoder D. C. (1997). Predicting soil erosion by water: a guide to conservation planning with the Revised Universal Soil Loss Equation (RUSLE) (Vol. 703). Washington DC: United States Department of Agriculture. Renard, K. G.

[17] Onstad C. A. Bosch D. D. Anderson W. P. (1989). AGNPS: A nonpoint-source pollution model for evaluating agricultural watersheds. Journal of soil Young, R. A. and 168-173. water conservation, 44(2).

[18] Porto-P. (2000). Sediment delivery distributed (SEDD) model. Journal of hydrologic engineering 5(4) 411-422. Ferro, V.

[19] Runoff Knisel, W. G. (1980). CREAMS: a field scale model for Chemicals and Erosion from Agricultural Management Systems [USA]. United States. Dept. of Agriculture. Conservation research report (USA).

[20] Sivapalan M. (1999). A conceptual model of sediment transport: application to the Avon River Basin in Western Australia. Hydrological Processes 13(5) 727-743. Viney, N. R.

[21] Quinton J. N. Smith R. E. Govers G. Poesen J. W. A. Auerswald K. Chisci G. Torri D. Styczen M. E. (1998). The European Soil Erosion Model (EUROSEM): a dynamic approach

for predicting sediment transport from fields Morgan, R. P. C., small catchments. Earth Surface Processes, and 527-544. Landforms: The Journal of the British Geomorphological Group, 23(6).

[22] Lane L. J. Foster G. R. (1991). WEPP: A new generation of erosion prediction technology. Journal of Soil Laflen, J. M. and 34-38. Water Conservation, 46(1).

[23] Huggins-L. F. Monke A. Beasley, D. B. Answers: A model for watershed planning. transactions of the asae. 23(4):938–0944, 1980.

[24] Onuigbo-A. A. Chinedu O. C. Ezeaku I. I. Muoneke M. M. (2017). Soil Erosion: A Review of Models Igwe, P. U., Applications. International Journal of Advanced Engineering Research, and 4(12). Science.

[25] Adamo M. Canora F. Aiello, A. *Remote Sensing and GIS to assess soil erosion with RUSLE3D and USPED at river basin scale in southern Italy*, volume 131. Catena, 2015.

[26] 65(1) 2-18. Vrieling, A. (2006). Satellite Remote Sensing for water erosion assessment: A review. Catena.

[27] Vuerich L. G. Zerihun W. (2002). Evaluation of environmental degradation in northern Ethiopia using GIS to integrate vegetation geomorphological erosion Feoli, E. and 91(1-3) 313-325. socio-economic factors. Agriculture, Ecosystems Environment.

[28] Jones R. J. A.- Montanarella L. (1999). Soil erosion risk assessment in Italy. European Soil Bureau European Commission. Van der Knijff, J. M. F.

[29] Märker M. Moretti S. Rodolfi G. Sidrochuk A. (2003). Integrating geographical information systems Remote Sensing ground truthing Flügel, W. A. and 929-942. modelling approaches for regional erosion classification of semi-arid catchments in South Africa. Hydrological Processes, 17(5).

[30] Wu J. Q. McCool D. K. Stöckle C. O. (2003). Estimating water erosion Fernandez, C., RUSLE sediment yield with GIS, SEDD. Journal of Soil, and 128-136. Water Conservation, 58(3).

[31] Mello C. R. Norton L. D. Curi N. Viola M. R. Avanzi J. C. Beskow, S. Soil erosion prediction in the grande river basin, brazil using distributed modeling. 79(1):49–59, 2009.

[32] J. The consequences of land-cover changes on soil erosion distribution in Slovakia Cebecaur, T.; Hofierka.

[33] K. N.; Bhadoria P. B. S. Effect of land use land cover change on soil erosion potential in an agricultural watershed Sharma, A.; Tiwari.

[34] E. Effect of land use land cover changes on the rate of soil erosion in the Upper Eyiohia river catchment of Afikpo North Area Nigeria. Environmental Challenges volume 1 1000002 2020 Obiahu, O. H.; Elias.

[35] Meusburger K. Ballabio C. Borrelli P. Alewell C. (2014). Soil erodibility in Europe: a high-resolution dataset based on LUCAS. Science of the total environment 479 189-200. Panagos, P.

[36] D.B. (Eds.) Slope instability: Wiley Singapore 1984. In Pradhan B.; Chaudhari A.; Adinarayana J.; Buchroithner-M.F. Soil erosion assessment Brunsden, D.; Prior, its correlation with landslide events using remote sensing data, and 184 715–727 GIS: A case study at Penang Island, Malaysia. Environ. Monit. Assess. 2012.

[37] D.J.; Szabolcs I. The global extent of soil degradation. In Soil Resilience Oldeman, L.R.; Greenland and 1992; pp. 99–118. Sustainble Land Use; CAB international: Wallingford, UK.

[38] H.; Stone J.J.; Pierson F.B.; Spaeth K.E.; Weltz M.A.; Flanagan D.C.; Hernandez M. A rangeland hydrology Nearing, M.A.; Wei and 901–908. erosion model. Trans. Am. Soc. Agric. Biol. Eng. 2011, 54.

[39] V.; Baffaut C.; Cerdan O.; Couturier A.; Hernandez M.; Le Bissonnais Y.; Nichols M.H.; Nunes J.P.; Renscheler C.S.; et al. Modeling response of soil erosion Nearing, M.A.; Jetten, runoff to changes in precipitation, and 131–154. cover. Catena 2005, 61.

[40] J.P.; Santos J.; Sampaio E.; Jacinto R.; Veiga S.; Lima J.C.; Moreira M.; Corte-Real J.; Keizer J.J.; et al. Impacts of climate Serpa, D.; Nunes, land use changes on the hydrological, and 64–77. erosion processes of two contrasting Mediterranean catchments. Sci. Total Environ. 2015, 538.

[41] M.; Anson E.; Nearing M.A.; Wei H.; Stone J.J.; Heilman P. Modeling climate change effects on runoff Zhang, Y.; Hernandez, soil erosion in southeastern Arizona rangelands, and 390–405. implications for mitigation with conservation practices. J. Soil Water Conserv. 2012, 67.

[42] M.; Ruiz E.; Antigüedad I. Simulation climate change impact on runoff Zabaleta, A.; Meaurio and 43 235– 245 sediment yield in a small watershed in the Basque Country, Northern Spain. J. Environ. Qual. 2014.

[43] J.; Pacheco N.R. Vulnerability of water resources vegetation productivi Nunes, J.P.; Seixas.

[44] A.; Sanchez-Canales M.; Terrado M.; López A.; Elorza F.J.; Ziv G.; Acuña V.; Schuhmacher M. Ecosystem services in Mediterranean river basin: Climate change impact on water provisioning Bangash, R.F.; Passuello and 246–255. erosion control. Sci. Total Environ. 2013, 458–460.

[45] H.; Van Dijk P.M. The impact of changes in climate Asselman, N.E.; Middelkoop, transport land use on soil erosion, and 3225– 3244. deposition of suspended sediment in the River Rhine. Hydrol. Process. 2003, 17.

[46] J.; Kreienkamp F.; Impact of climate change on soil erosion—A high-resolution projection on catchment scale until 2100 in Saxony/Germany. Catena 2014 121 99–109. Routschek, A.; Schmidt.

[47] A.M.; Fröb F.; Liniger M.A. Climate change signals of CMIP5 general circulation models over the Alps—Impact of model selection. Int. J. Climatol. 2016 36 3088–3104. Zubler, E.M.; Fischer.

[48] S.; Beniston M.; Heinrich G.; Rajczak J.; Stoffel M. 21st century climate change in the European Alps—A review. Sci. Total Environ. 2014 493 1138–1151. Gobiet, A.; Kotlarski.

[49] H.; Senatore A. EURO-CORDEX regional climate model analysis for the Greater Alpine Region: Performance Smiatek, G.; Kunstmann and 7710–7728. expected future change. J. Geophys. Res. Atmos. 2016, 121.

[50] Qin D. Plattner G.K. Tignor M. Allen S.K. Boschung J. Nauels A. Xia Y. Bex V. Midgley P.M. Eds.; Cambridge University Press: Cambridge UK; New York NY USA 2013. IPCC. Summary for Policymakers. In Climate Change 2013: The Physical Science Basis. Contribution of Working Group I to the Fifth Assessment Report of the Intergovernmental Panel on Climate Change; Stocker, T.F.

[51] J.A.; Hibbard K.A.; Manning M.R.; Rose S.K.; van Vuuren D.P.; Carter T.R.; Emori S.; Kainuma M.; Kram T.; et al. The next generation of scenarios for climate change research Moss, R.H.; Edmonds and 747–756. assessment. Nature 2010, 463.

[52] B. Influence of rapid glacial retreat on the rate of erosion by tidewater glaciers. Geology 2002 30 47–50. Koppes, M.; Hallet.

[53] 171 247–259. Vezzoli, G. Erosion in the Western Alps (Dora Baltea Basin): 2. Quantifying sediment yield. Sediment. Geol. 2004.

[54] F.; Spreafico M.; Schadler B. Ripercussions of a CO2 doubling on the water balance: A case study in Switzerland J. Hydrol. 1992 137 199–208. Bultot, F.; Gellens.

[55] M. Climatic Change Beniston and 2004. its Impacts: An Overview Focusing on Switzerland; Kuwler Academic Publishers: Dordrecht, The Netherlands.

[56] L.; De Jong C. Collins D. Ranzi R. Eds. The influence of glacier retreat on water yield from high mountain areas: Comparison of Alps Hagg, W.; Braun, central Asia. In Climate, Hydrology of Mountain Areas; Wiley, and USA 2005; Volume 18 pp. 263–275. Sons: Hoboken, New Jersey.

[57] L.N.; Kuhn M.; Nesgaard T.I. Modelling of hydrological response to climate change in glacierized Central Asian catchments J. Hydrol. 2007 332 40–53. Hagg, W.; Braun.

[58] R. Effects of transient climate change on basin hydrology 2. Impacts on runoff variability of the Arno River Basin central Italy Hydrol. Process. 2002 16 1177–1199. Burlando, P.; Rosso.

[59] G.; Giorgi F.; Bi X. Extreme precipitation over the Maritime Alps Boroneant, C.; Plaut, associated weather regimes simulated by a regional climate model: Present-day, and 81–99. future climate scenarios. Theor. Appl. Climatol. 2006, 86.

[60] https://www.icimod.org/ International Centre for Integrated Mountain Development.

[61] upper Ganges High resolution 5 km daily reference climate dataset of upper Indus and upper Bramhmaputra river basins from 1981 to 2010. http://rds.icimod.org/Home/DataDetail?metadataId=29332searchlist=True.

[62] Shuttle Radar Topography Mission. https://www2.jpl.nasa.gov/srtm/.

[63] Hofierka J. Zlocha M Iverson L. R. (1996). Modelling topographic potential for erosion Mitasova, H. and 629-641. deposition using GIS. International Journal of Geographical Information Systems, 10(5).

[64] S. I. Estimation of Slope Length factor (L) Rammahi, A. A.; Khassaf and 2018 Slope Steepness Factor (S) of RUSLE equation in Euphrates River Watershed by GIS. Kufa Journal of Engineering, 9(3).

[65] Rusco E. Montanarella L. Panagos P. Bosco, C. Soil erosion in the alpine area: risk assessment and climate change. 85:117–123, 2009.

[66] Gianinetto M. Vezzoli R. Rota Nodari F. Polinelli F. Frassy F. Rulli M.C. Ravazzani G. Aiello, M. and Chiarelli D.D. Passera C. Bocchiola D. Corbari C., Soncini A. *Modelling soil erosion in the Alps with dynamic RUSLE-like model and satellite observations. Proceedings of the Italian Society of Remote Sensing conference 2018.* 2018.

[67] D.; Rosso R. Spatial downscaling of precipitation from GCMs for climate change projections using random cascades: A case study in Italy. Water Resour. Res. 2011 47 W03519. Groppelli, B.; Bocchiola.

[68] A.; Bocchiola D.; Rosso R. Evaluation of future hydrological cycle under climate change scenarios in a mesoscale Alpine watershed of Italy. Nat. Hazard. Earth Sys. 2011 11 1769–1785. Groppelli, B.; Soncini.

[69] P.S.; Daniell T.M. Contour-based digital elevation modeling of watershed erosion Sun, H.; Cornish, sedimentation: Erosion, and 38. doi:10.1029/2001WR000960. sedimentation estimation tool (EROSET). Water Resour. Res. 2002.

[70] L.A.; Van Fossen M.; Maguire D.J. Batty M. Goodchild M.F. Eds. Transition potential modeling for land-cover change. In GIS Spatial Analysis Eastman, J.R.; Solorzano and USA 2005 pp 357–385. Modelling; ESRI Press: Redlands, CA.

[71] D.G.; Shellito B.A.; Manik G.A. Using neural networks Pijanowski, B.C.; Brown and 553–575. GIS to forecast land use changes: A land transformation model. Comput. Environ. Urban Syst. 2002, 26.

[72] M: Clark University. http://www.clarklabs.org/applications/uplaad/Land-Change-Modeler-IDRISI-Focus-Paper-pdf Clark Labs (2009) The land-change modeler for ecological sustainability. IDRISI Focus Paper, Worcester.

[73] M. Meijaard-E. Deforestation projections for carbon-rich peat swamp forests of Central Kalimantan Indonesia. Environ. Manag. 2011-48-436-447 Fuller, D.O.; Hardiono.

[74] Vezzoli R. Polinelli F. Frassy F. Rota Nodari-F. Rulli M.C. Ravazzani G. Corbari C. Soncini A. Chiarelli D.D.-Passera-C.-Bocchiola D. Gianinetto M. Aiello, M. *Analisi di sensitività nella stima dell'erosione di suolo nelle Alpi con misure in situ e serie temporali Landsat. Acts of the XXII Conferenza Nazionale ASITA 2018.* 2018.

[75] M.; Vezzoli R.; Rota Nodari F.; Polinelli-F.; Frassy F.; Rulli M.C.; Ravazzani G.; Bocchiola D.; Soncini A.; et al. Satellite-based cover management factor assessment for soil water erosion in the Alps. In Proceedings of the Remote Sensing for Agriculture Ecosystems Gianinetto, M.; Aiello, Germany 10–13 September 2018; International Society for Optics Hydrology, Berlin, and USA 2018; Volume 10783 p. 107830T. doi:10.1117/12.2325536. Photonics: Bellingham, WA.

[76] G. A.; Salomonson V. V. Development of methods for mapping global snow cover using moderate resolution imaging spectroradiometer data. Remote Sensing of Environment Volume 54 Issue 2 1995 Pages 127-140 Hall, D. K.; Riggs.

[77] Borrelli P. Meusburger K. (2015). A new European slope length Panagos, P. and 117-126. steepness factor (LS-Factor) for modeling soil erosion by water. Geosciences, 5(2).

[78] C.; Meusburger K.; Spinoni J.; Alewell C.; Borrelli P. Towards estimates of future rainfall erosivity in Europe based on REDES Panagos, P.; Ballabio and 251–262. WorldClim datasets. J. Hydrol. 2017, 548.

[79] J.; Keizer J.J. Modeling the response of within-storm runoff Nunes, J.P.; Seixas, multi-scale approach to scenario design erosion dynamics to climate change in two Mediterranean watersheds: A multi model, and 27–39 analysis. Catena 2013, 102.

[80] F.J.P.M. The Supply of Sediment to the River Rhine Drainage Network. The Impact of Climate Change Van Dijk, P.M.; Kwaad, Land Use Change on Soil Erosion, and 1999.

Sediment Transport to Stream Channels; Report of the NRP project 952210; University of Amsterdam: Amsterdam, The Netherlands.

[81] J.G.; Kiniry J.R.; Williams J.R. Soil Neitsch, S.L.; Arnold and TX USA; Texas AM University System: College Station TX USA 2011. Water Assessment Tool Theoretical Documentation Version 2009; Report No. 406; Texas Water Resources Institute Technical: College Station, TX.

[82] D.; Martínez-Pérez S.; Sastre-Merlín A.; Jeppesen E. Hydrological Molina-Navarro, E.; Trolle, water quality impact assessment of a Mediterranean limno-reservoir under climate change, and 354–366. land use management scenarios. J. Hydrol. 2014, 509.

[83] M.; Ceaglio E.; Maggioni M.; Meusburger K.; Alewell C.; Zanini E. Soil erosion in an avalanche release site (Valle d'Aosta: Italy): Towards a winter factor for RUSLE in the Alps. Nat. Hazards Earth Syst. Sci. 2014 14 1761–1771. Stanchi, S.; Freppaz.

[84] S.R.; Heath J.T.; Musselman K.N.; Revuelto J.; Latron J.; Morán-Tejeda E.; Jonas T. Small scale spatial variability of snow density Lopez Moreno, J.L.; Fassnacht and 55 40–52. depth over complex alpine terrain: Implications for estimating snow water equivalent, Adv. Water Resour. 2013.

[85] IPCC. Summary for Policymakers. In Global Warming of 1.5°C. An IPCC Special Report on the Impacts of Global Warming of 1.5°C above Pre-Industrial Levels, Sustainable Development Related Global Greenhouse Gas Emission Pathways, in the Context of Strengthening the Global Response to the Threat of Climate Change, and Zhai H.-O. Pörtner D. Roberts J. Skea P.R. Shukla A. Pirani W. Moufouma-Okia C.-Péan R. Pidcock S. et al. Eds.; World Meteorological Organization: Geneva Switzerland 2018; p. 32 Efforts to Eradicate Poverty; Masson-Delmotte, V.P.

[86] D.A.; Fleischer-L.R.; Lugato E.; Ballabio-C.; Alewell C.; Meusburger K.; Modugno S.; Schütt B.; Ferro V.; et al. An assessment of the global impact of 21st century land use change on soil erosion. Nat. Commun. 2017 8 2013. Borrelli, P.; Robinson.